Development and Characterization of a Laser-Induced Desorption Source for FEL Experiments

Dissertation

zur Erlangung des Doktorgrades
an der Fakultät für Mathematik, Informatik und Naturwissenschaften,
Fachbereich Physik
der Universität Hamburg

vorgelegt von

Zhipeng Huang

Hamburg

2019

1. Gutachter: Prof. Dr. Jochen Küpper
2. Gutachter: Prof. Dr. Henry N. Chapman

Gutachter der Dissertation:	Prof. Dr. Jochen Küpper Prof. Dr. Henry Chapman
Zusammensetzung der Prüfungskommission:	Prof. Dr. Jochen Küpper Prof. Dr. Henry N. Chapman Prof. Dr. Daniel A. Horke Dr. Sadia Bari Prof. Dr. Daniela Pfannkuche
Vorsitzender des Prüfungsausschusses:	Prof. Dr. Daniela Pfannkuche
Datum der Disputation:	16. May 2019
Vorsitzender Fach-Promotionsausschusses PHYSIK:	Prof. Dr. Michael Potthoff
Leiter des Fachbereichs PHYSIK:	Prof. Dr. Wolfgang Hansen
Dekan der Fakultät MIN:	Prof. Dr. Heinrich Graener

Eidesstattliche Versicherung / Declaration on oath

Hiermit versichere ich an Eides statt, die vorliegende Dissertationsschrift selbst verfasst und keine anderen als die angegebenen Hilfsmittel und Quellen benutzt zu haben.

Die eingereichte schriftliche Fassung entspricht der auf dem elektronischen Speichermedium.

Die Dissertation wurde in der vorgelegten oder einer ähnlichen Form nicht schon einmal in einem früheren Promotionsverfahren angenommen oder als ungenügend beurteilt.

Ort, Datum	Zhipeng Huang

Abstract

The recording of structural dynamics of individual large biomolecules requires efficient delivery of these biomolecules, which are usually thermally labile or non-volatile, to the X-ray or electron beam interaction point. Laser-induced acoustic desorption (LIAD) is a promising technique for gentle and efficient preparation of large intact neutral molecules into the gas-phase.

In this thesis a newly set-up LIAD source was designed for prolonged measurement times and fixed interaction point, as required by free-electron laser (FEL) experiments, through a tape-drive automatic sample replenishment method. A novel sample preparation method utilized gas dynamic virtual nozzle to aerosolize sample was implemented to deposit uniform layers on the long 10 µm thick tantalum foil band, which was irradiated by the third harmonic of a nanosecond Nd:YAG laser on the back surface. The induced photoacoustic stress and thermal stress waves travel through the foil and desorb deposited samples into the gas-phase. Stable dense phenylalanine, adenine and glycine plumes with density higher than 10^9 cm^{-3} were created and characterized using strong-field ionization (SFI) by an intense femtosecond laser field. The produced ions induced by SFI were detected by a linear time-of-flight mass spectrometer (TOF-MS).

Number density, spatial extend, temporal distribution, translational velocity, and translational temperature of created plumes were fully characterized. Effects of desorption laser intensity, sample layer thickness on LIAD prepared thermally labile and thermally stable molecules were evaluated. These results show a thorough picture of the desorption process and molecule plume characteristics. While translational velocity is invariant for different desorption laser intensities, pointing to a non-thermal desorption mechanism, the translational temperature increases significantly and higher fragmentation is observed with increased desorption laser fluence for thermally labile molecules, which shows that more thermal energy was transferred to sample at higher desorption laser intensity. The broad temporal distribution, long delay (∼8 µs) between desorption molecule signals and desorption laser pulse rules out the shake-off model and point to a indirect coupled desorption mechanism. The kinetic energy of prepared plume is in the range of the surface stress energy between foil substrate and sample layer, which supports the previous proposed stress-induced desorption mechanism.

Zusammenfassung

Die Messung struktureller Veränderungen von großen Biomolekülen, welche oft thermisch labile oder nichtflüchtig sind, erfordert einen effizienten Transport der Biomoleküle von der Quelle hin zum Wechselwirkungspunkt zwischen der Probe und dem, zum Beispiel, Röntgen-, oder Elektronenstrahl. Laser-induzierte akustische Desorption (Laser-induced acoustic desorption, LIAD) ist ein vielversprechender experimenteller Ansatz um große Moleküle sanft und elektrisch neutral in die Gasphase zu bekommen.

In dieser Dissertation wird die Entwicklung einer neuartigen LIAD-Quelle gezeigt bei welcher die LIAD-Quelle mit einem sogenanntem Tape-Drive (Laufband) kombiniert wird um Moleküle über einen längeren Zeitraum kontinuierlich in die Gasphase zu bringen. Das Tape-Drive wird für den automatischen Probennachschub genutzt und erlaub somit lange, kontinuierliche Messzeiten welche sehr wichtig sind für, zum Beispiel, Messungen an freien Elektronen Lasern (FELs). Das Laufband besteht aus einer 10 µm dünnen Tantal-Folie und dient gleichzeitig als Probenträger. Die zu messenden Moleküle werden mit einer sogenannten gas dynamic virtual nozzle (GDVN) auf die Vorderseite der Folie deponiert um eine dünne, einheitliche Schicht zu garantieren. Die Desorption von der Folie erfolgte durch einen frequenzverdreifachten Nd:YAG Lasers (Desorptionslaser) welcher auf die Rückseite der Folie fokussiert wird. Der in der Folge entstehende photoakustische Stress sowie die thermische Schockwelle in der Folie führen zur Desorption der Moleküle an der Vorderseite. Die entstandene Gas-, oder Molekülwolke wurden anschließend mittels eines fs-Laser ionisiert (Multiphoton-, und Tunnelionisation) und in einem Ionen-Flugzeitmassenspektrometer analysiert. Innerhalb der Dissertation wurden so verschiedene stabile und intakte Moleküle von Phenylalanin, Adenin und Glycin mit einer Dichte von 10^9 cm^{-3} nachgewiesen.

Ein großes Augenmerk wurde auf die Charakterisierung der erzeugten Molekülwolke gelegt. Hierbei wurden die Dichte, die räumliche und zeitliche Verteilung, Translationsgeschwindigkeit und Temperature der Molekülwolke in Abhängigkeit gesetzt zur Energie des Desorptionslasers und der Dicke der aufgetragenen Molekülschicht. Die Ergebnisse zeigen, dass die Translationsgeschwindigkeit der Molekülwolken nahezu unabhängig von der Energie des Desorptionslasers ist was auf einen nicht-thermischen Desorptionsmechanismus hindeutet. Im Gegensatz dazu wurde eine höhere Fragmentation der Moleküle beobachtet was, bei den verwendeten thermisch-labilen Molekülen, auf eine höhere interne Temperature und somit auf einen höheren thermischen Energietransfer deutet. Die zeitliche Dauer des Molekülwolke und die lange zeitliche Verzögerung (∼8 µs) zwischen

der Desorption der Moleküle und dem Desorptionslaser deuten auf einen indirekt gekoppelten Desorptionsmechansismus hin und schließen somit das sogenannte shake-off model aus. Die kinetische Energie von den Molekülen ist in der Größenordnung der Oberflächenspannungsenergie zwischen den Molekülen und der Folie was auf einen zuvor schon vorgeschlagenen stressinduzierten Desorptionsmechanismus hindeutet.

Contents

1 Introduction

Atoms and molecules are building blocks of nature. Investigating the structural dynamics of these molecules is crucial to understand how nature works [1]. There are different dynamics happening in molecules on different time scales, such that electron dynamics of molecules occuring on the attosecond (10^{-18} s) timescale, with the classical period of the electron in a Bohr hydrogen atom being 150 attoseconds [1]. The fastest molecular vibrations occur in the molecular hydrogen are on the order of 20 femtoseconds (10^{-12} s), while molecular rotations occur on a picosecond timescale [1]. With the known structure of molecules, their functions can be determined, which enables the structure-based drug design and development. From the known structural dynamics of molecules, one can know how they function in real time. We are interested in imaging structural dynamics of molecules in the gas-phase, as gas-phase molecules get rid of the undesired influences from the surroundings, which enable us to investigate their intrinsic properties.

X-ray Free-Electron Lasers (XFEL) hold the promise to image isolated biomolecules and particles with femtosecond temporal and picometer spatial resolution [3, 5–7]. The main challenges in these experiments are the extremely low signal-to-noise ratio due to the very low number density of samples in gas-phase, as well as the random orientation of molecules in each shot. In order to enhance the signal-to-noise ratio, the recording of structural dynamics of individual molecules requires the efficient delivery of controlled, identical molecules to the interaction point. By dispersing molecular beams with strong electric fields, pure samples of individual conformers or clusters according to their quantum state can be routinely separated [8–12]. State-selected molecules can be further controlled as alignment and orientation by laser and static electric fields [8, 13–15], as shown in Figure 1.1. We are currently working towards extending these techniques to much large molecules and systems, ranging from amino acids, peptides, DNA strands to proteins or even viruses. Most of these large biomolecules are thermally labile and some of them are light sensitive or non-volatile. Traditional vaporization method (i.e. simply heating) can not be applied to bring these biomolecules into gas-phase, as they will be destroyed during heating or not vaporized. Laser-induced acoustic desorption (LIAD) is

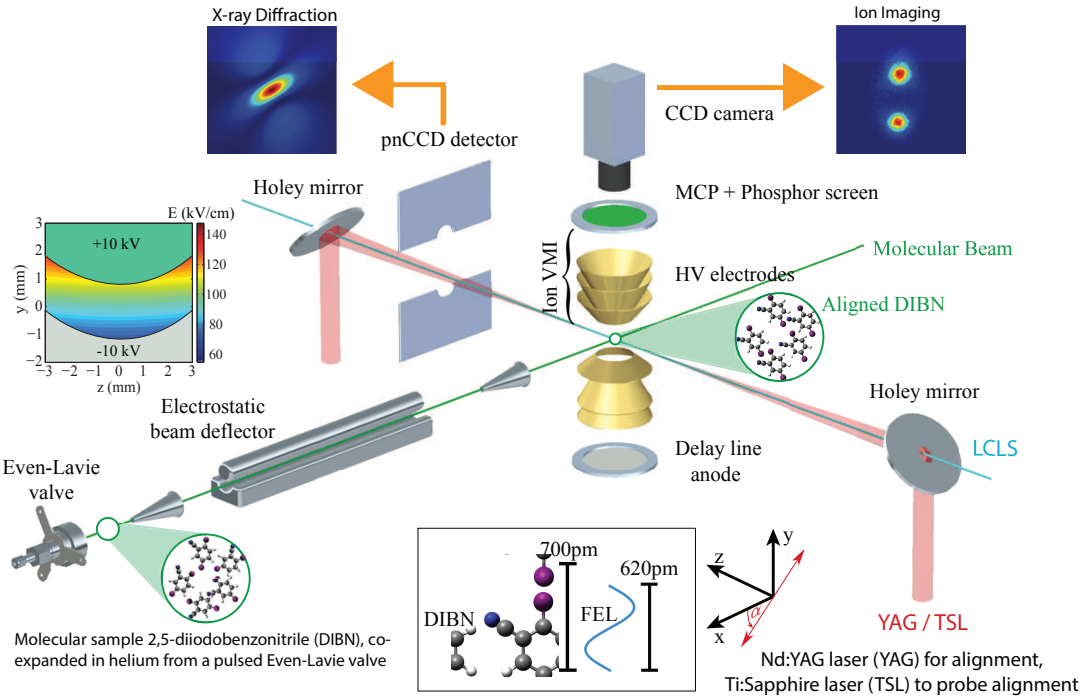

Figure 1.1: Schematic drawing of the experimental setup used in our group for gas-phase molecule structure dynamic studies [2–4]. See texts for details.

a promising technique to solve these problems for gentle and efficient preparation of these large intact neutral molecules into the gas-phase [16–19].

The scheme of laser-induced acoustic desorption was first proposed by B. Lindner and U. Seydel at 1985 [16]. They shined a pulsed nanosecond laser on a transparent substrate and the generated photoacoustic waves traveled through the substrate and desorbed molecules on other side out of the surface. Afterwards several groups were involved in this research field and applied this technique to mass spectrometry research areas [19–21]. Group of H. I. Kenttämaa coupled it with a Fourier Transform Ion Cyclotron Resonance Mass Spectrometer [22–24] and a quadrupole linear time-of-flight mass spectrometer [25, 26] to analyze chemical properties of large molecules. Group of Zhang extended this technique to bring single cells into the gas-phase [20, 27] for precise mass measurements. Greenwood's group utilized this source to study the ultrafast dynamic of biomolecules [28, 29]. Furthermore group of Francesca combined it with attosecond techniques and observed the ultrafast electron dynamics in phenylalanine [30]. What sets LIAD apart from other laser-based vaporization techniques such as laser desorption [31–34], is that it avoids any direct interaction between the desorption laser and the molecular sample, making this technique applicable to light-sensitive and labile compounds.

Although LIAD has been applied to variety research areas and shows great potential, reproducibility of the source, unclear desorption mechanism and little knowledge of desorbed plume properties are limiting its potential application [35].

Here in this thesis a newly LIAD setup for prolonged measurement times through tape-drive automatic sample replenishment method was designed. In order to create a stable coverage of sample on the foil, sample was aerosolized using a gas-dynamic virtual nozzle (GDVN) [36,37] and deposited on the foil, where it sticks and rapidly dries out. The novel sample deposition method provides a uniform sample coverage on the LIAD substrate and hence stable signal intensity for experiments. With shining the back surface of the foil band by third harmonic Nd:YAG laser pulses, the induced photoacoustic and thermal waves traveled through the foil and desorbed the uniform deposited sample into the gas phase. A stable, dense, neutral molecular plume was created in the vacuum, with which we studied the plume properties thoroughly. Here we employed strong-field ionization (SFI) to characterize the desorbed molecules. In SFI molecules are ionized using a strong non-resonant femtosecond laser pulse with typical field-strengths on the order of $>10^{13}$ W/cm^2. This leads to the ejection of electrons through tunnel or multi-photon ionization (see section 2.2), and hence the production of cations. The produced cations were detected by a time-of-flight mass spectrometer. The stable plume density enabled us measure the spatial-temporal profile of the plume at different interaction points, plume number density at different desorption laser intensities precisely. As a result the plume translational velocity, translational temperature and desorption mechanism were derived and discussed thoroughly in this thesis. The fragmentation processes during desorption and ionization were investigated for thermally stable and thermally labile molecules respectively. Effects of deposited sample layer thickness on the desorption process, plume properties were studied. Based on these experimental results, the desorption mechanism was carefully discussed.

This thesis consists of four parts. The first part is on conceptional background, which is presented in chapter 2. Vaporization techniques for large molecules, laser-matter interaction, X-ray/electron imaging for gas-phase molecules are explained in this part. The second part contains experimental apprautus, which are developed for gas-phase large molecule preparation, and sample preparation techniques to deposit uniform sample layers on metal foil (LIAD substrate). The experimental setup and sample preparation methods are presented in chapter 3 in detail. The third part is mainly on experiments that were conducted by the newly designed setup. It includes preparation of phenylalanine, adenine, glycine samples into gas-phase, strong-field characterization of these prepared plume by intense femtosecond laser fields and detection by time-of-flight mass spectrometer (TOF-

MS) [38]. These experiments were presented in chapter 4, chapter 5, and chapter 6, respectively. Chapter 4 mainly focuses on the characterization of phenylalanine plume for its number density, spatial extend, temporal distribution, fragmentation, forward velocity and translational temperature etc. Chapter 5 compares the plume properties for thermally stable adenine and thermally labile glycine molecules in order to better understand the desorption mechanism and source properties. Chapter 6 evaluates the effects of sample layer thickness on the prepared plume properties. The last part is on conclusion and outlook. We summarized the results we got and what we have learned. Potential applications of the developed setup for free-electron laser experiments and other experiments were discussed in this part.

2 Conceptional Background

Image ultrafast structural dynamics of isolated molecules is a dedicated goal for physicist, chemist, and biologist. With the development of fourth-generation X-ray free-electron laser sources (XFEL) and ultrafast electron sources, these facilities enable us to image isolated molecules in picometer spatial resolution and femotosecond temporal resolution [39–42]. The recording of "molecular movies" of individual molecules requires the efficient delivery of controlled, identical molecules to the interaction point [3]. Different gas-phase sample preparation methods, which were developed for these experiments, are briefly presented in this chapter. Femtosecond laser-molecule interaction and X-ray or electron diffractive imaging are briefly explained.

2.1 Gas-phase Molecule Preparation

Preparing intact molecules into gas phase is the first step for gas-phase X-ray or electron imaging experiments. There are different ways to bring molecules into the gas phase [43–47]. Some of the methods which bring isolated neutral molecules into gas phase are described below.

2.1.1 Thermal Vaporization

The conventional way to prepare molecules into gas phase is thermal vaporization [48, 49]. Usually the sample is directly deposited as powders in a temperature controlled oven or valve. Then the sample got heated to a sufficient temperature to vaporize.

Molecules produced by thermal vaporization can be cooled down with supersonic expansion cooling [48, 50]. The generated vapor from the oven can be mixed with seeding gases (i.e. helium in 1∼10 bar) and then expanded through a nozzle into vacuum. For example an Even-Lavie valve can be used to produce pulsed cold molecular beams (∼ 20 µs) [51] as shown in Figure 1.1. The initial volatilization of the molecules is prepared by thermal vaporization. Then the adiabatic jet expansion out of the valve creates collisions

between the sample molecules and carrier gas atoms, which cool the molecule rotational and vibrational temperatures down to a few K [52, 53]. Even though this volatilization method creates cold samples, which are required for gas phase experiments such as conformer separation and laser alignment [54–56], it can only be applied for molecules that are thermally relatively stable as shown in Figure 1.1. It is not applicable to thermally labile sample, such as most of biomolecules, which would get destroyed at high temperatures, or non-volatile molecules which do not vaporize by heating.

2.1.2 Laser Desorption

Laser desorption (LD) overcomes the problem of samples with low vapor pressures and can vaporize thermally labile samples. The sample molecules are mixed with the matrix molecules i.e. graphite, 2,5-Dihydroxybenzoic acid, etc. and get deposited on a sample bar. The mixtures then get irradiated by a laser, resulting in the desorption of matrix and sample molecules [57–60]. LD prevents damaging sample molecules by depositing most of the energy into the matrix molecules and fast desorption time reduces thermal transport to sample molecules. It was already used to transfer biomolecules with masses ranging in the 10 000 dalton region in the gas phase [61] and coupled with supersonic expansion for the preparation of cold large molecules [31, 62–68]. But it is not applicable to light sensitive molecules, as the laser shines on the samples directly.

2.1.3 Laser-Induced Acoustic Desorption

The volatilization method used in this thesis tries to transfer large, thermally labile, non-volatile, light sensitive neutral molecules into the gas-phase by adapting the laser-induced acoustic desorption method, which was proposed by Lindner nearly thirty years ago [16].

As illustrated in Figure 2.1, a UV laser beam shines the back of a metal foil with sample deposited on the front. Thermal and acoustic waves are produced due to the interaction of laser with the metal foil. When the thermal and acoustic waves propagate to the other side of the metal foil, they will induce stress on sample molecules, which are desorbed following. This method avoids the direct shining of laser light on sample directly, so it can be applied to light-sensitive molecules. The desorption is caused by acoustic and thermal induced stress, so it can be used to transfer thermally labile or non-volatile sample into gas-phase.

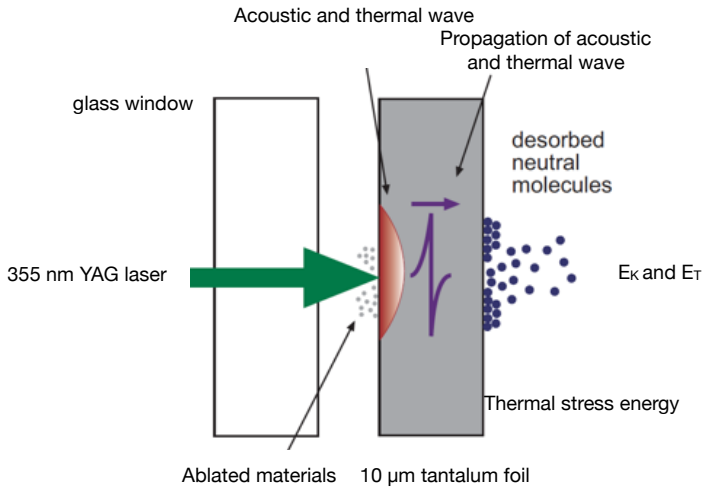

Figure 2.1: Schematic of working principle of LIAD [69]. See main texts for further details.

2.2 Photoionization Mechanism

With the development of ultrafast laser systems, it opens new dimensions of light matter interaction. The radiation intensity $I = W/(A \cdot \tau_{\text{Laser}})$ in a focused laser pulse scales with the pulse energy W, focal area A, and pulse duration τ_{Laser}. Thus, the ultrashort laser pulse i.e. femtosecond pulse can generate gigantic electric field strengths, which can be comparable with the potential valence electron experienced on the molecular orbit. [70]

Atoms and molecules exposed to such extreme conditions, they would be electronically excited and ionized. There are different ionization regimes defined by the atom or molecule ionization potential, laser wavelength, laser field strength, etc. Theory to describe the different ionization process on atoms under laser fields is briefly presented below, and it can be extended to molecules. That is the case for the experimental parts of this thesis, we adapted photoionization method to characterize the prepared molecular sources.

2.2.1 Single-Photon Ionization

Single-photon ionization occurs when the energy of a photon is higher than the atom ionization potential V_p. Electrons (usually valence electrons) get exited from the atom/molecule by a single photon as shown in Figure 2.2(a). Kinetic energy of exited electron is given by $E_{kin} = h\nu - V_p$ where h is the Planck constant.

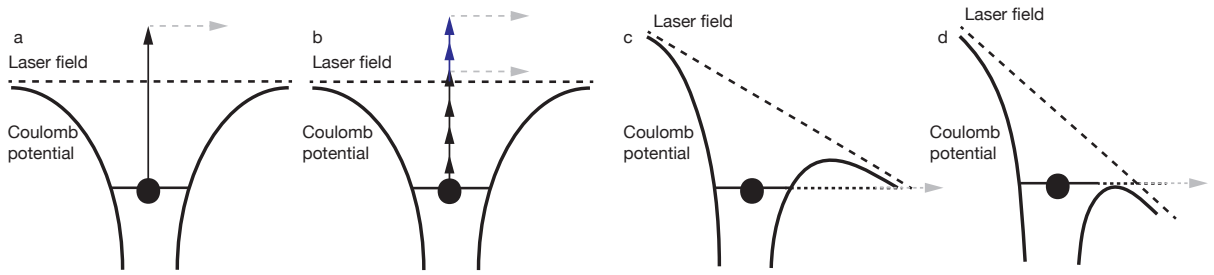

Figure 2.2: Different ionization mechanisms for atoms or molecules under laser field [71]. a)Single-photon ionization. b)Multi-photon ionization. c)Tunneling ionization. d)Over the barrier ionization.

2.2.2 Multi-Photon Ionization

When the energy of a photon is lower than the ionization potential V_p, a single photon is not enough to ionize the atom or molecule, but multi-photon ionization (MPI) could occur for this case. Electrons get exited from the atom or molecule excited by multiple photons within the lifetime of the excited state. This can either be achieved over real energy levels with tunable lasers i.e. dye laser or over imaginary energy levels with relatively high intensity lasers. For the former case, the ionization can be enhanced due to the resonant states, so it is also called resonant enhanced multi-photon ionization (REMPI). In the latter case, the life time of the energy level is determined by the Heisenberg uncertainty relation $\Delta E \cdot \Delta t \geq \hbar/2$. It usually needs a high photon flux to ionize the atom or molecule due to the very short life time of the imaginary state. At MPI regime the laser field strength is much less than the electric field for binding the electron in atom or molecule. Perturbation theory can be applied to explain the MPI process [72]. The rate Γ_n for an n-photon process is given by:

$$\Gamma_n = \sigma_n I^n \tag{2.1}$$

where σ_n is the cross section for the event and I is the intensity of the laser. Kinetic energy of the exited electron that absorbed n photons of frequency ν is given by $E_{kin} = nh\nu - V_p$. For a Ti:Sapphire laser used in this thesis, it has a central wavelength $\lambda = 800$ nm. The energy of one photon is calculated as $hc_0/\lambda \approx 1.55$ eV where c_0 is the speed of light in vacuum. To multi-photon ionize phenylalanine with a vertical ionization potential of $V_p = 8.63$ eV [73, 74], a total of 8.63 eV/1.55 eV $\approx 5.57 < 6$ photons are needed.

If more photons are absorbed than necessary for ionization, atoms or molecules can be above-threshold ionized. It still belongs to multi-photon ionization regime and its photoelectron emission spectra will show peaks clearly separated in photon energy step.

2.2.3 Tunneling Ionization

At very high laser field strength, the internal atomic field will be modified substantially by the external oscillating electric field. In this case, the laser field can't be treated as a perturbation any more. It causes the bending of the atomic potential and the creation of a coulomb wall with a finite tunnel probability of electrons. The resulting potential $V(r,t)$ is determined by the atomic potential and the electric field of the laser.

$$V(r,t) = -\frac{Ze^2}{4\pi\epsilon_0 r} + eE(t)r \tag{2.2}$$

where Z is the atomic number of the ionized atom, e is the charge of an electron and ϵ_0 is the electric field constant. The first term in equation 2.2 is the undisturbed coulomb potential, while the second term represents the potential generated by the laser.

Since the laser field oscillates, the electrons need to escape from the atom fast enough before the field reverses. When the tunneling time of the electron is much faster than the oscillation of the laser field, the laser electric field can be treated as static when tunneling. Equation 2.2 can be written as below:

$$V(r) = -\frac{Ze^2}{4\pi\epsilon_0 r} + eEr \tag{2.3}$$

2.2.4 Over the Barrier Ionization

When the laser field is so high that it is even higher than the atomic potential, the bound electron can thus leave the atom "above-barrier", so it is termed over-the-barrier (OTB) ionization. The ionization probability under this regime tends to one. The intensity of a laser and its electric field are correlated as bellow [75, 76]

$$I = \frac{1}{2} c_0 \epsilon_0 E^2 \tag{2.4}$$

where c_0 is the speed of light in vacuum. The minimum laser intensity I_{cr} for this happens can be calculated by identifying the maximum of the coulomb wall in equation 2.3 when $\frac{\partial V(r)}{\partial r} = 0$ and equating it with the potential $V(r) = -V_p$. Hence the minimum intensity needed for over the barrier ionization occurring can be calculated with equation 2.3 and 2.4 to:

$$I_{cr} = \frac{\pi^2}{2} \frac{c_0 \epsilon_0^3}{e^6} \frac{V_p^4}{Z^2} \tag{2.5}$$

This intensity is also know as the saturation intensity, where all atoms experiencing an intensity higher than this will be ionized. Spectrum of photoelectrons emitted from tunneling ionization or over-the-barrier ionization have a continuous distribution.

2.2.5 Keldysh Parameter

The Keldysh parameter γ was introduced to determine the dominating ionization mechanism by Keldysh in 1965 [77]. It is described as below

$$\gamma = \sqrt{\frac{V_p}{2U_p}} \tag{2.6}$$

where U_p is the ponderomotive potential. The ponderomotive potential is the "quiver" energy of a free electron in an AC electric field due to its oscillation. When $\gamma \ll 1$, tunneling is dominant. When $\gamma \gg 1$, MPI is the dominating ionization mechanism. The ponderomotive potential is given by

$$U_p = \frac{e^2 E^2}{4 m_e \omega^2} \tag{2.7}$$

where ω is the angular frequency of the electric field, m_e is the mass of electron. Substitute Equation 2.7 and Equation 2.4 into Equation 2.6, the Keldysh parameter can be described as following:

$$\gamma = \sqrt{\frac{\epsilon_0 c_0 m_e \omega^2 V_p}{e^2 I}} = 2.31 \times 10^3 \sqrt{\frac{V_p/eV}{I/10^{12} W cm^{-2} \lambda^2/nm^2}} \tag{2.8}$$

where λ is the wavelength of laser. It is obvious that with the same laser intensity I for higher angular frequency ω or shorter wavelength λ, the Keldysh parameter will become larger, which means tunneling ionization is less dominant. In order to allow the electrons to leave the atom, the tunneling time needs to be smaller than one half of the oscillation period, say $\tau < 1/(2\ \omega)$. [75] While the angular frequency ω rises, the tunneling time τ of an electron (determined by the coulomb wall) stays the same, making it less possible for the electron to tunnel out of the potential due to the fast oscillation of the laser field.

For experiments conducted in this dissertation, we utilize strong-field ionization (SFI) to post ionize desorbed neutral plume. The ionization regime ranges between multi-photon and tunnel ionization regime. SFI is a universal ionization technique since it does not rely on molecular resonances. But the SFI process can furthermore lead to fragmentation. Thus, while the use of SFI leads to denser mass spectra due to SFI-

induced fragmentation, it also carries more information as all fragments produced by the source can be observed. The use of the "fragment-to-parent ratio" allows us to quantify this fragmentation occurring during the desorption process itself.

2.3 X-ray or Electron Diffractive Imaging

In order to derive the structural dynamics of gas-phase molecules (i.e. nuclear positions and electronic densities as a function of time in femtosecond resolution), ultrafast X-ray or electron diffractive imaging were commonly used [3, 5, 78–87]. For X-ray, it interacts with electrons in the molecules and induces quiver motions for the electrons, which emit photons of the same wavelength due to dipole radiation. For coherent scattering the photon energy is conserved and the radiation from all electrons corresponding to their density is superposed coherently. The coherent sum contains structural information of the molecules [88]. For electron diffraction, incoming electrons are sensitive to both the nuclei and electrons within the molecules, as they interact with the coulomb potentials [89, 90]. Cross sections for electrons are significantly larger than X-ray photons [91, 92]. But the number density and pulse duration for electrons are not comparable with fourth generation X-ray source due to coulomb repulsion of electrons.

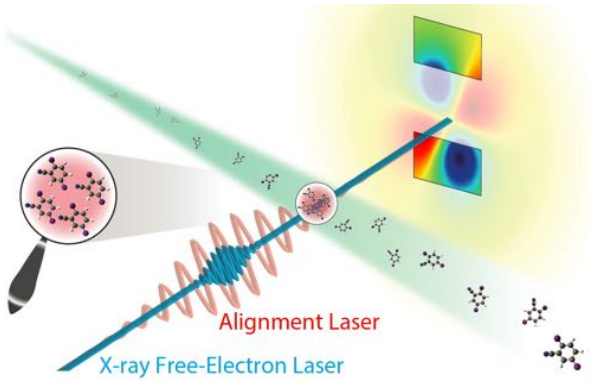

Figure 2.3: Sketch of the X-ray or electron coherent diffraction of controlled molecules [3, 5, 7]

Figure 2.3 shows the sketch of X-ray or electron diffraction of controlled molecules. The green beam shows the prepared cold molecular beam. The molecules are aligned and oriented under the alignment laser and external DC fields. And then aligned and oriented molecules are diffracted by X-ray or electron pulses [86, 93, 94]. The diffracted patterns are recorded by the detector. Each X-ray or electron pulse will shot fresh samples, so the diffraction before destruction concepts can be applied and it can be also applied for non-reversible process investigation, as fresh samples are delivered to each X-ray or electron

pulse. Because molecules are aligned and oriented, the diffraction signals can be added up to improve the signal to noise ratio.

3 Experimental Methods [1]

3.1 Introduction

A laser-induced acoustic desorption setup, developed for use at central facilities, such as free-electron lasers, is presented in this chapter. The setup was developed to prepare large biomolecules, ranging from amino acids, nucleotides, to peptides, DNA strands, which are usually thermally labile or light sensitive, into gas phase. The apparatus contains vacuum system, LIAD source, time-of-flight mass spectrometer (TOF-MS), data acquisition (DAQ) system and optical laser setup, which are presented in following sections, respectively. Details on the experimental apparatus can be found in section 3.2. In order to create a stable coverage of sample on the foil, sample was aerosolized using a gas-dynamic virtual nozzle (GDVN) [36, 37] and deposited on the foil, where it sticks and rapidly dries out. The novel sample deposition method provides a uniform sample coverage on the LIAD substrate and hence stable signal intensity for experiments. The sample preparation method is presented in section 3.3.

3.2 Experimental Setup

3.2.1 Vacuum System

Figure 3.1 shows the schematic overview of the whole setup. The LIAD source and TOF-MS are housed inside a vacuum chamber, which is evacuated with a turbomolecular pump (Pfeiffer Vacuum HiPace 700) to typical operating pressures of 10^{-8} mbar. The TOF-

[1] This chapter is partly based on the supplementary information of the paper *Development and Characterization of a Laser-Induced Acoustic Desorption Source*, Zhipeng Huang, Tim Ossenbrüggen, Igor Rubinsky, Matthias Schust, Daniel A Horke, and Jochen Küpper, *Analytical Chemistry* **90**, 3920–3927 (2018).
I designed the setup together with D. Horke, T. Ossenbrüggen, M. Schust, and J. Küpper. I developed the sample preparation method and conducted the experiments and data analysis. Together with the other authors, I discussed the results and wrote the article.

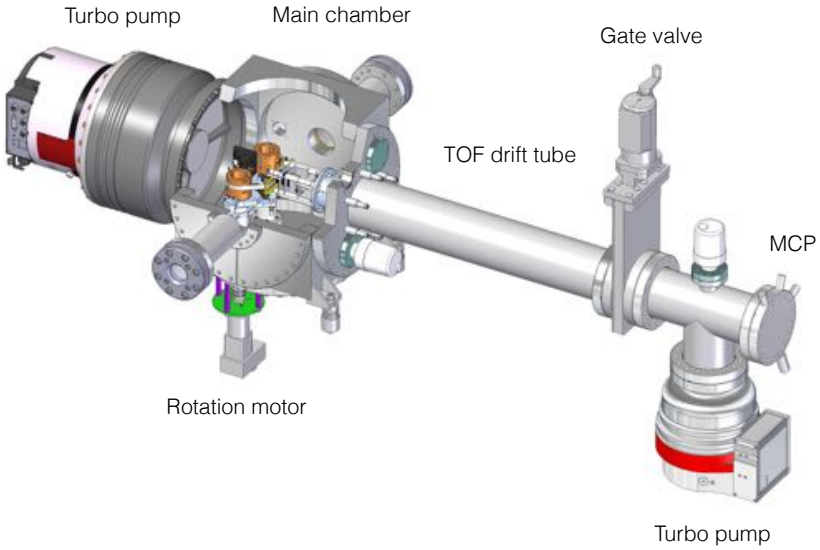

Figure 3.1: Overview of the LIAD setup, consisting of vacuum system, tape-drive source, time-of-flight mass spectrometer.

MS microchannel plate (MCP) detector is isolated from the main vacuum chamber by a gate valve to allow sample exchange without venting the detector. The detector chamber is pumped by a turbomolecular pump (Pfeiffer Vacuum TMU 261) and a pressure of 10^{-9} mbar is typically maintained. For the two turbomolecular pumps, they are both connected to a forevacuum line, which is pumped by a scroll pump (Edwards XDS35i) to maintain a pressure of 10^{-2} mbar. The main vacuum chamber allows optical access for the desorption and ionization lasers through anti-reflection coated windows.

3.2.2 LIAD Source

The LIAD source utilized a tape-drive method to replenish the sample, which ensured the interaction point was fixed and undisturbed for prolonged measurement times. A schematic of the tape-drive LIAD source setup developed in this dissertation is shown in Figure 3.2. It consists of a sample cartridge "taper platform" containing the sample of interest deposited on a long foil band. The taper platform, shown in detail in Figure 3.2, consists of a solid aluminum baseplate, onto which two brass rollers (outer diameter 50 mm) are mounted with grease-free vacuum compatible roller bearings (HWG Horst Weidner GmbH). Between the two rollers the tantalum foil band containing the molecular sample is held under tension. One of the rollers is connected via an axle and rotation feedthrough to a stepper motor (Schneider LMDCE421-G1A9) housed outside the vacuum

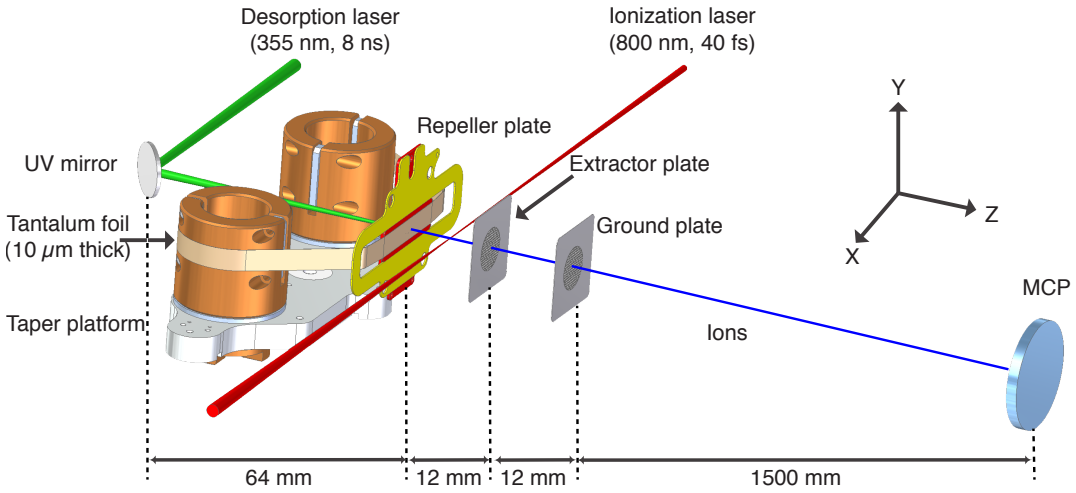

Figure 3.2: LIAD taper platform with sample delivery based on a rotating tape drive. See text for further details.

to allow motorized rotation at variable speeds. The other roller is freely rotating with an adjustable resistance. At the front of the platform the foil band is fed over a stainless steel plate with rounded edges (shown in red in Figure 3.2) to avoid damaging the foil band and a central hole of 4 mm diameter to allow the desorption laser to reach the backside of the foil. This stainless steel plate can interlock with a corresponding part (shown in yellow in Figure 3.2) on the TOF electrode setup to ensure repeatable and correct alignment of the molecule source to the TOF electrodes. The entire taper platform is mounted on a quick release platform inside the vacuum chamber and can be quickly exchanged; two stainless steel dowels ensure repeatable alignment inside the vacuum chamber.

Figure 3.3(a) shows the computer-aided design (CAD) drawing of the rotating tape-drive LIAD source. It shows how the taper platform is coupled with the time-of-flight mass spectrometer, and how it connects to the supported posts on the bottom flange.

Figure 3.3(b) shows the dimension and size of the tape drive platform from a top view. Both rollers have a diameter of around 50 mm and a distance of 110 mm far away. During data collection the foil band is moved across the desorption laser spot by rotating the brass rollers, thereby constantly providing fresh sample. The typical speed of the foil band was on the order of 50 µm/s. The reason for this speed is discussed later in subsection 4.3.1.

3.2.3 Laser System

The desorption laser, third harmonic of an Innolas Spitlight 600-20 YAG operated at 355 nm (central wavelength) with a repetition rate of 20 Hz and pulse durations of 8 ns

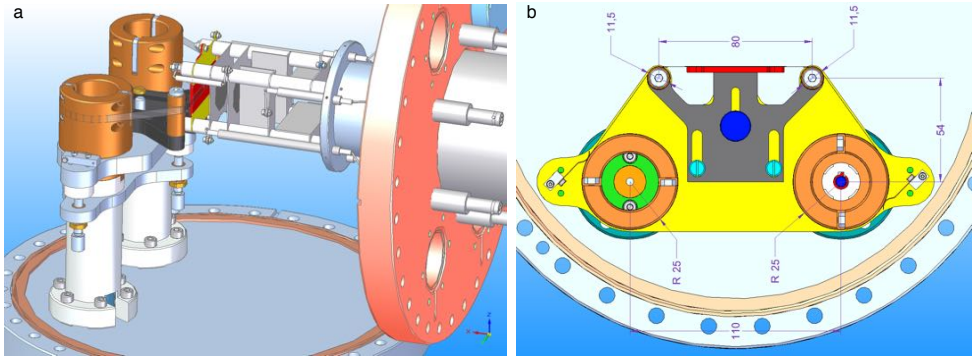

Figure 3.3: CAD drawing of the LIAD setup with sample delivery based on a rotating tape drive and coupled with a three-electrode Wiley-McLaren TOF spectrometer. (a)Side view of the setup; (b)Top view of the tape-drive platform (unit in mm).

(FWHM), focused with a $f = 400$ mm lens to a spot size of 300 µm (FWHM), gets coupled in over a mirror inside the vacuum chamber and irradiates the foil on the back side. The pulse energies could be adjusted with a $\lambda/2$ wave plate and a polariser or with the delay between flash lamp and Q-switch of the laser. The spot size, as well as the spot position on the foil, could be adjusted using translation mounts, onto which the focusing lens was placed. Typical pulse energy utilized in this thesis is usually at 0.6 mJ.

Molecules are deposited on a 10 µm tantalum foil and desorbed out of the foil by the desorption laser. Once desorbed, molecules get ionized between the repeller and extractor plates of the TOF-MS through strong-field ionization, induced by 40 fs (FWHM) pulses from an chirped pulse amplified Ti:Sapphire laser (Spectra Physics Spitfire ACE). The ionization laser was focused with a $f = 750$ mm lens to a spot size of 100 µm (FWHM) in the interaction region, with typical field strengths on the order of 4×10^{13} W/cm^2.

3.2.4 Mass Spectrometer

The LIAD source is coupled with a Wiley-McLaren Jordan linear time-of-flight mass spectrometer [38], which determines ions mass-to-charge ratio from their flight time. Figure 3.4 shows the CAD drawing of the mass spectrometer electrodes. The Wiley-McLaren design TOF has three electrodes (repeller, extractor, ground) with a distance of 12.8 mm between each other, with a typical mass resolution $m/\Delta m > 1000$. When running experiments, electric potential of 4.2 kV and 3.5 kV are usually set for the repeller and extractor electrodes, respectively. Once molecules getting ionized between the repeller and extractor plates, they are accelerated to the drift tube and then detected by the multi-channel plate (MCP) detector. The flying time of the created ions are recored by a digitizer, which is described in subsection 3.2.5. The ion mass-to-charge ratio is proportional to the square

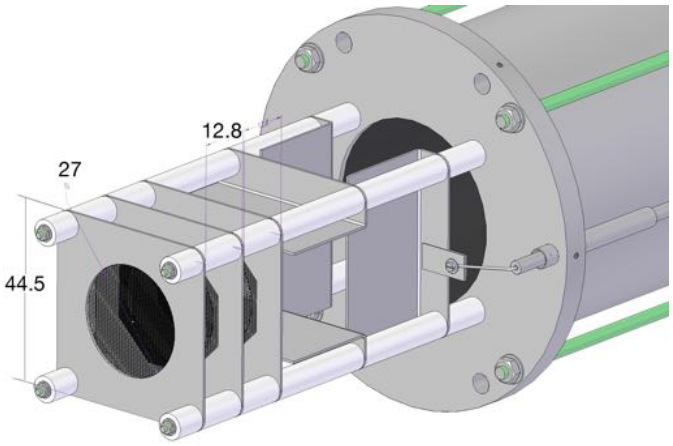

Figure 3.4: Dimensions of the Wiley-McLaren linear time-of-flight spectrometer [38] (unit in mm), which is coupled to the LIAD source.

of the time-of-flight, therefore the experimentally measured time-of-flight t of ions can be converted to their mass-to-charge ratio m/q when the mass of one time-of-flight peak is known. For the mass spectra recorded in this thesis, the known peaks were either water ion peak at 18 u or the dominant ion peak, i.e. 74 u fragment ion of phenylalanine, 135 u molecule ion of adenine and 30 u fragment ion of glycine. These peaks were primarily used for the mass calibration. The relationship between time-of-flight and mass-to-charge ratio is shown below. Detailed derivation can be found in appendix section A.2.

$$\frac{m}{q} = \frac{m_1}{q_1}\left(\frac{t - t_0}{t_1 - t_0}\right)^2 \tag{3.1}$$

where t_0 is the delay between digitizer electronic trigger and ionization laser photons, m_1/q_1 and t_1 is the known TOF-MS peak.

For the offset t_0, either it can be experimentally determined with a photo diode for recording the delay between the electronic trigger and photon arriving time to the interaction point or it can be derived if two peaks in the TOF spectrum are know. For the latter case, t_0 can be derived from below,

$$t_0 = \frac{t_1 - t_2\sqrt{\frac{\left(\frac{m_1}{q_1}\right)}{\left(\frac{m_2}{q_2}\right)}}}{1 - \sqrt{\frac{\left(\frac{m_1}{q_1}\right)}{\left(\frac{m_2}{q_2}\right)}}} \tag{3.2}$$

where m_2/q_2 and t_2 is the second known TOF-MS peak.

With the known t_0, experimentally measured time-of-flight can be converted to mass-to-charge ratio using Equation 3.1. Detailed derivation of calibration equation for ion time-of-flight to ion mass-to-charge ratio can be found in appendix section A.2.

3.2.5 Data Acquisition

The ion current produced on the MCP detector is read out with a 12 bit digitizer (SP Devices ADQ412). The bandwidth of the digitizer is 1 GHz corresponding to a time resolution of 1 ns. Our home developed CMIDAQ software was used to control the digital delay generator, rotation motor, lens stage motor and acquire data from the digitizer.

The number of ions impacting on the MCP is proportional to the output voltage. Knowing the output voltage of a single ion impacting on the MCP, we can evaluate the number of ions detected on the MCP. The ionization laser intensity was reduced so that only one molecule or less per laser shot was ionized. By plotting histogram of the integration of parent ion peak, we can distinguish the single ion amplitude on the MCP. Figure 3.5 shows histogram of the integration of phenylalanine parent ion peak intensity. A clear two distributions were shown in the figure. The first distribution is coming from the single ion impacting on the detector and a second distribution is due to two ions impacting signal. The focus spot size of ionization laser is around 100 µm. The FWHM of plume transverse spatial profile at 2 mm is around 2 mm. As a result the interaction volume is around 1.0×10^{-5} cm^3. If assuming the strong-field ionization efficiency equals one, number density of the plume can be calculated by dividing the number of parent ions per laser shot with ionization laser interaction volume. But this value should be considered the lower limit as it does not account for the contribution from the fragment ions.

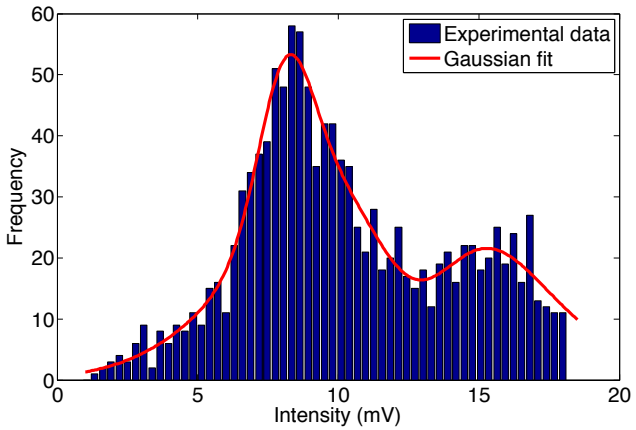

Figure 3.5: Histogram of the integration of phenylalanine molecule ion peak .

3.3 Sample Preparation

Preparing a uniform sample layer on the metal foil substrate is crucial for achieving a stable LIAD source. In order to control the sample preparation process rigidly and get a uniform layer prepared on the foil, we aerosolized sample molecules using a gas-dynamic virtual nozzle (GDVN) [36, 37] and deposited this aerosol onto the foil, where it rapidly dries out and sticks. The sample thickness can be controlled by adjusting the flow rate of sample through the GDVN, and thereby the aerosol production rate, or by adjusting the speed of the foil band as it moves through the aerosol beam.

Figure 3.6 shows the schematic of sample preparation setup. The gas dynamic virtual nozzle was used to create aerosol droplets. The foil band was replenished by a tape-drive platform. A optical microscope was mounted to monitor the sample deposition on the foil band in real-time.

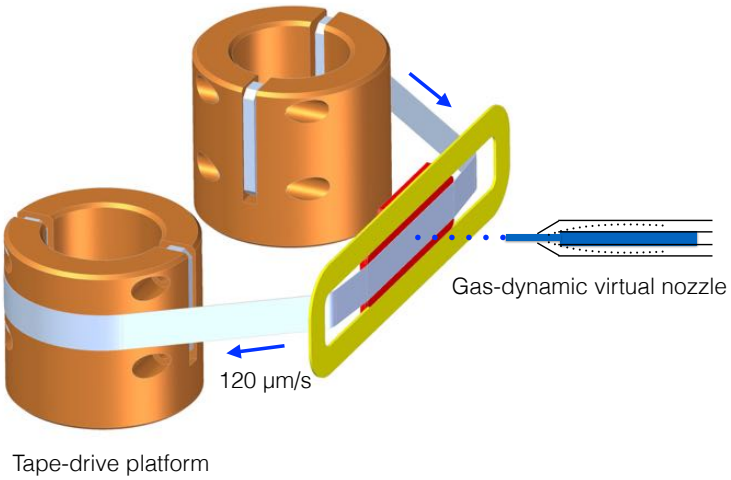

Figure 3.6: A diagram of the sample preparation setup (see main text for details). The tape-drive system drives the foil band across an aerosol beam produced by a gas-dynamic virtual nozzle to get samples deposited uniformly on the foil band.

In particular for the experiments presented in chapter 4 and chapter 5, we aerosolized a 0.1 M aqueous solution of sample inside a ceramic injection-molded GDVN with a liquid inner capillary of 75 µm diameter [36, 37]. A liquid flow rate of 20 min was maintained and focused at the tip of the nozzle into a thin (several micrometer) liquid jet by helium focusing gas at 30 bar pressure. After ∼1 mm propagation the liquid jet becomes unstable and breaks up into small droplets, producing a fine mist of aerosolized particles, which was deposited onto the foil band placed 40 mm away. The aerosolization and deposition

process was constantly monitored through a long working distance microscope. The foil band was advanced at 120 µm/s; thus, it took approximately 140 min to cover the entire 1 m long foil band with sample. By weighing foil bands before and after application of sample, we can determine an approximate surface coverage of the sample. This should be considered an upper limit since this estimation is based purely on the weight of applied material and it is unclear to what extend water remains bound to samples and hence gets deposited on the foil band, adding to the recorded weight. By varying the foil band moving speed, we could control the deposited sample layer thickness systematically, as presented in chapter 6.

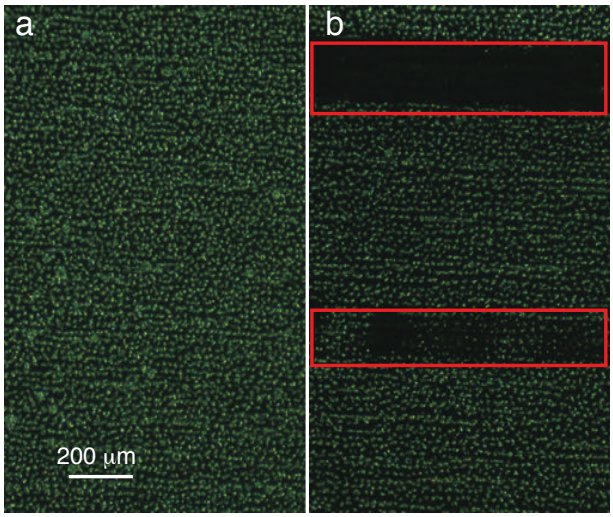

Figure 3.7: Optical microscope image of phenylalanine deposited on a 10 µm Ta foil using aersolization spraying. Images were taken before (a) and after (b) desorption in the LIAD setup. The latter clearly shows two regions where the desorption laser has depleted the deposited sample, as indicated by the red framed regions.

A microscope image of a foil band after sample deposition is shown in Figure 3.7 a. This clearly shows a uniform distribution (If summing up the image intensity horizontally or vertically, the standard deviation of the summed image intensity is ∼2.4 %) of deposited small islands of sample across the entire surface. For comparison, we also show an image of a foil band following desorption of sample in our LIAD setup in Figure 3.7 b. In these images the sample was moved horizontally with a speed of 50 µm/s while the desorption laser was on, leading to a dark stripe across the image where the foil is void of sample. The upper (and darker) gap corresponds to desorption of sample with 2 J/cm^2 laser intensity, which removed nearly all sample from the foil. The lower one was taken with 0.7 J/cm^2, and some sample molecules are observed to remain on the foil band.

Figure 3.8 a shows a microscope image of sample deposited on the foil band after

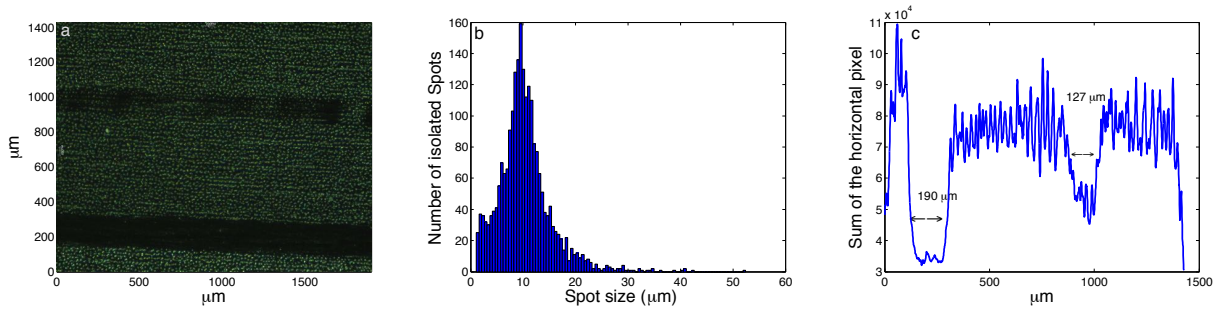

Figure 3.8: Optical microscope image of phenylalanine sample spreads on Ta foil band after desorption in the LIAD setup (a); Sample island size distribution of the area without desorption (b); Integration of the horizontal pixel intensity of the microscope image along the vertical axis (c).

desorption. From the area without laser scanning we can see that a uniform layer was prepared. Figure 3.8 b shows the histogram of sample island spot size distribution from the area without desorption. The island sizes were determined by circle finding algorithm of the bright isolated spots. The algorithm finds edges of the bright spots and fits them with round circles. The circle diameter gives an estimate the sample island size. The most probable island size is around 9 µm, which is around 1/33 of the desorption laser focus spot size. In an area of desorption laser spot, there are around 500 sample islands uniformly distributed. This insures that the signal is stable during sample replenishment. Figure 3.8 c shows integration of the horizontal pixel intensity of Figure 3.8 a along the vertical axis. It gives information of the desorption area width at two different desorption laser intensities. The vertical width of desorption lines is approximately 200 µm, which is a bit smaller than the FWHM of desorption laser focus spot size (300 µm). The width of desorbed area also contains information of desorbed plume initial spatial distribution, which will be discussed in chapter 4.

3.4 Summary

A laser-induced acoustic desorption setup for preparing large biomolecules into gas-phase, coupled with a time-of-flight mass spectrometer, was presented in this chapter. Different parts of the apparatus were described throughly. In summary, the vacuum system maintains a 10^{-8} mbar and 10^{-9} mbar pressure for the source chamber and detector chamber, respectively. The laser system contains a third harmonic Nd:YAG nanosecond laser and a Ti:sapphire femtosecond laser for sample desorption and strong-field characterization respectively. These two lasers are synchronized with a digital delay generator. The DAQ system ensures fast data read out from the MCP detector and parameter scanning.

A novel sample preparation method with depositing aerosols onto the foil substrate to produces uniform sample layers was introduced. The uniform distributed sample layer ensured the LIAD source was stable. The sample preparation was usually conducted in a conventional fume hood. And then the prepared sample was installed into the vacuum chamber for experiments. A detailed characterization of the LIAD source will be discussed in chapter 4.

4 Characterize the Laser-Induced Acoustic Desorption Source [1]

A laser-induced acoustic desorption source, developed for use at central facilities, such as free-electron lasers, is presented in chapter 3. It features prolonged measurement times and a fixed interaction point. A novel sample deposition method using aerosol spraying provides a uniform sample coverage and hence stable signal intensity. Utilizing strong-field ionization as a universal detection scheme, the produced molecular plume is characterized in terms of number density, spatial extend, fragmentation, temporal distribution, translational velocity, and translational temperature. The effect of desorption laser intensity on these plume properties is evaluated. While translational velocity is invariant for different desorption laser intensities, pointing to a non-thermal desorption mechanism, the translational temperature increases significantly and higher fragmentation is observed with increased desorption laser fluence.

4.1 Introduction

Recent years have seen the development of several techniques to control isolated neutral molecules in the gas-phase. Molecular beams of polar molecules can be dispersed with strong inhomogeneous electric fields, producing pure samples of individual conformers, cluster stoichiometries or even single quantum-states [8,9,11,95–98]. We can, furthermore, control the alignment and orientation of complex gas-phase molecules in space [13–15,54], allowing one to extract molecular-frame information, such as nuclear or electronic struc-

[1] This chapter is based on the paper *Development and Characterization of a Laser-Induced Acoustic Desorption Source*, Zhipeng Huang, Tim Ossenbrüggen, Igor Rubinsky, Matthias Schust, Daniel A Horke, and Jochen Küpper, *Analytical Chemistry* **90**, 3920–3927 (2018), DOI: 10.1021/acs.analchem.7b04797, arXiv: 1710.06684 [physics].
I designed the setup together with D. Horke, T. Ossenbrüggen, M. Schust, and J. Küpper. I developed the sample preparation method and conducted the experiments and data analysis. Together with the other authors, I discussed the results and wrote the article.

tures, from these samples [99, 100]. In combination with the technological developments in free-electron laser (FEL) ultrafast x-ray sources, now providing millijoule-level pulses of hard x-rays with sub-100 fs pulse durations, these control techniques open up the potential to image isolated biomolecules and particles with femtosecond temporal and picometer spatial resolution [3, 5, 7, 101].

The realization of these experiments crucially depends on a high-density source of intact molecules in the gas-phase, ready for further manipulation and experiments. While for many small stable compounds this is easily achieved using thermal vaporization and seeding into a molecular beam, this approach is not feasible for thermally labile or non-volatile species – such as most larger biochemically relevant molecules, and biological species in general. Therefore, these samples, which are one of the primary driving forces behind FEL facilities, require the development of gentle vaporization techniques, that still produce a pure and high-density sample of molecules in the gas-phase. Furthermore, technical requirements for central-facility experiments, such as a well-defined and fixed interaction point and capabilities for long uninterrupted measurements times, need to be fulfilled.

One approach to achieve relatively dense ensembles of labile neutral molecules is laser-induced acoustic desorption (LIAD), which has been introduced over 30 years ago [16], but received relatively little attention since. What sets LIAD apart from other laser-based vaporization techniques, such as laser desorption [102], is that it avoids any direct interaction between the desorption laser and the molecular sample, making this technique applicable to light-sensitive and labile compounds. The basic principle of LIAD is that samples get deposited on one side of an opaque substrate – often a thin metal foil – while the other side of this substrate gets irradiated with a laser pulse. This laser pulse induces an acoustic or thermal wave in the substrate, which travels through the material and leads to desorption of molecules on the front side. The physical mechanism behind this desorption process is currently very poorly understood, i. e., even the nature of the desoprtion process (thermal, acoustic, stress-induced) is not clearly established and, furthermore, it is highly dependent on the employed substrate and sample preparation method [35].

Nonetheless, the LIAD technique has been used in a number of mass spectrometry studies [19–21]. Notably, the Kenttämaa group coupled LIAD to a Fourier transform ion cyclotron mass spectrometer [22–24] and a quadrupole linear time-of-flight mass spectrometer [25, 26]. They used this source to study peptides and large organic compounds up to ∼500 u mass. Recently, the LIAD methodology has also been applied to study the dynamics of intact aminoacids on the femtosecond and attosecond timescale using ion-yield and photoelectron spectroscopy [28–30]. In a seminal paper in 2006, Peng et al.

showed the applicability of LIAD to significantly larger systems and particles, successfully desorbing viruses, bacteria and cells and storing them in a quadrupole ion trap for precise mass measurements [20, 27]. The Campbell group furthermore established a closely related technique, termed "laser-induced forward transfer" for the gentle vaporisation of large nanoparticles [103, 104].

Here, we present our new LIAD-source setup, designed for use in central facilities such as free-electron lasers or advanced-table-top-laser user facilities. It allows for prolonged measurement times through automatic sample replenishment, whilst keeping the interaction point fixed. This is realized through the use of a long metal tape as the LIAD substrate, which is constantly forwarded – akin to an old-fashioned cassette tape – to provide fresh sample. A reproducible layer of molecules is prepared on this foil by spraying aerosolized samples onto the band. This technique yields a stable and reproducible signal for many hours of measurement time. As a test system we use the amino acid phenylalanine and characterize the produced molecular plume using strong-field ionization, evaluating the number density, spatial extend and temporal distribution. By convoluting the initial plume temporal distribution with a Maxwell-Boltzmann velocity distribution, the forward velocity and the translational temperature in the moving frame were derived. While the velocity does not increase with desorption laser intensity, the translational temperature does increase and, furthermore, we observe enhanced fragmentation. These observations are consistent with a desorption model based on surface stress between the foil band and islands of deposited molecules, which was previously proposed [35].

4.2 Experimental Method

A schematic of our new LIAD setup is shown in Figure 3.2; further details regarding the setup and sample preparation are given in the chapter 3. Briefly, sample is deposited on the front side of a tantalum foil band of 10 µm thickness and 10 mm width, while the backside gets irradiated with a pulsed desorption laser. We use tantalum as a substrate due to its very high melting point of 3290 K and hence its ability to withstand higher desorption laser intensities. During data collection the foil band is constantly moved across the desorption laser spot to provide fresh sample, as further discussed below. In order to create a stable coverage of sample on the foil, we aerosolized samples using a gas-dynamic virtual nozzle (GDVN) [36, 37] to create and deposit an aerosol on the foil, where it sticks and rapidly dries out. Full details of the sample preparation and deposition process, including details regarding sample concentration, spray rate, speed of

the foil band, and an estimate of total deposited material are given in the section 3.3.

Molecules are desorbed using ∼8 ns duration laser pulses at 355 nm, focused to a 300 µm (FWHM) spot on the foil. Desorbed molecules are strong-field ionized by 40 fs pulses from a Ti:Sapphire laser, with typical field strengths of 4×10^{13} W/cm^2. Produced cations are detected by a conventional linear time-of-flight mass spectrometer (TOF-MS), with a typical mass resolution $m/\Delta m > 1000$.

4.3 Results and Discussion

4.3.1 Characterizing LIAD by strong-field ionization

In order to characterize the molecular plume desorbed from the metal foil band we utilize strong-field ionization from a focused femtosecond Ti:Sapphire laser as an universal probing scheme [28,67]. The observed time-of-flight mass spectrum of phenylalanine (PA)

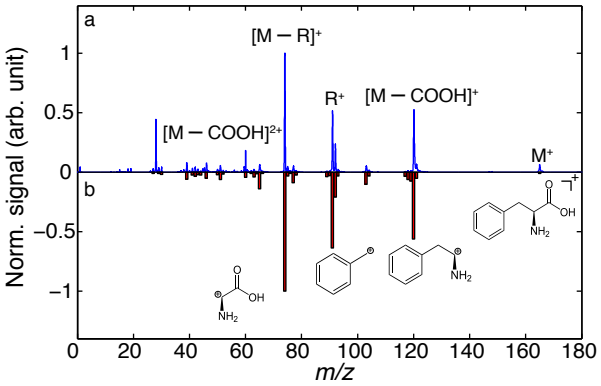

Figure 4.1: Mass spectrum of phenylalanine; (a) recorded using LIAD and strong-field ionization from a femtosecond laser beam and (b) reference spectrum for electron impact ionization [105]. The intensity in both spectra is normalized to the dominant mass peak at 74 u.

is shown in Figure 5.1 and compared to a literature spectrum obtained using electron-impact ionization (EI) [105]. Both spectra are normalized to the intensity of the most abundant fragment at mass 74 u, corresponding to loss of a benzyl-radical fragment from PA. It is evident that both ionization schemes strongly induce fragmentation, however we do note that using SFI a significant contribution from intact PA is observed at 165 u; this could even be enhanced using improved laser pulses [28]. We observe no evidence in the mass spectrum for the production of larger clusters of PA, and hence attribute this channel to intact PA monomers desorbed from the foil. Furthermore, we observe an

additional fragmentation channel in the SFI data, loss of a C-NH_2 group (28 u), which is absent in the EI mass spectrum. These spectra clearly demonstrate the production of intact PA following desorption from the foil band. We do not observe the emission of any tantalum atoms or clusters from the foil band, which would easily be ionized by the SFI probe, since the ionization potential of tantalum is lower than of PA. This indicates that the desorption laser does not penetrate through the foil band nor ablate metal from the foil by other means. We further discuss the observed fragmentation in subsection 4.3.3 below.

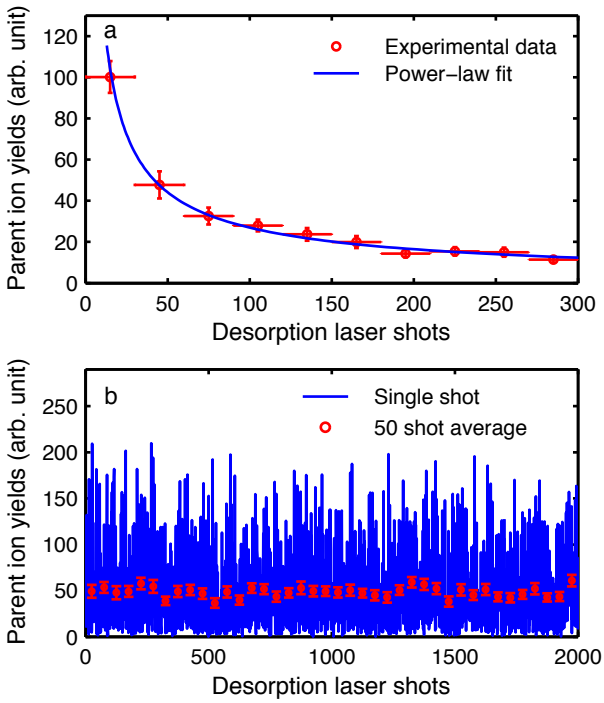

Figure 4.2: (a) Parent ion yield as a function of desorption laser shot without sample replenishment. Data have been averaged over 30 shot-wide intervals, represented by the horizontal bars; the solid line corresponds to a power-law fit. (b) Parent ion signal as a function of desorption laser shot while moving the foil band at 50 µm/s. The blue line corresponds to single-shot measurements, red markers correspond to averaged data for 50 shots, showing a standard deviation below 10%.

To assess the depletion of deposited sample from the foil and to determine the required moving speed of the foil band for sample replenishment, we measured the parent ion yield as a function of the number of desorption laser shots onto the same spot. The resulting intensities are shown in Figure 4.2 a, where the solid line represent a power-law fit of the form $y = A \times x^n$, with a fitted exponent of n $= -0.68 \pm 0.03$. We observe a rapid decay of signal, with signal levels falling to around 10% after 330 desorption laser shots. Similar power-law behavior has previously been observed and rationalized with the existence of

several isolated desorption centers on the foil surface [35]. This is consistent with our observation of many large crystalline islands on the foil surface, see Figure 3.7, many of which fall within the desorption laser spot size.

During further data collection the foil band is continuously moved at 50 µm/s, corresponding to a movement to a new sample spot every ∼120 desorption laser shots. The corresponding shot-to-shot signal stability for the moving foil band is shown in Figure 4.2 b. The signal exhibits large fluctuations with a single shot standard deviation of 70% of the mean value. No long-term drift of the overall signal levels is observed. Averaging over 50 desorption laser shots reduces the standard deviation to below 10%, as indicated by the red markers and error bars in Figure 4.2. Further data points in this manuscript are typically averaged over 1200 desorption laser shots, resulting in a standard deviation of ∼2.5%.

4.3.2 Molecular Plume Properties

In the following we investigate the spatial extent, density, velocity, and translational temperature of the "plume" of molecules desorbed from the foil band. We estimate absolute number densities from ion counting measurements and the known interaction volume as defined by our ionization laser, as described in section 3.2. In Figure 4.3 a we show the measured number density of parent ions in the center of the desorbed plume as a function of distance from the foil band. We note that the shown densities are lower limits, since their calculation assumes an ionization efficiency of 1 for SFI and considers the measured intact parent ions only, such that any fragmentation induced by the SFI probe will reduce the derived density. The obtained densities exhibit approximately an inverse-square-law behavior with distance from the desorption spot on the foil, since the expansion along the laser propagation direction is not reflected in the measurements due to the large Rayleigh length of the ionization laser ($z_R \approx 38$ mm). We note that the data point closest to the foil band for the measurement at 0.64 J/cm^2 shows a significantly lower than expect density, which we can only explain with a lower density of molecules attached on the desorption foil band for this measurement, due to some instability during the aerosolization process.

We assess the spatial extent of the plume, i. e., the transverse profile, by translating the ionization laser in height along the y-axis as defined in Figure 3.2, across the plume of molecules. This is shown in Figure 4.3 b for three distances between the foil band surface and the interaction point. The initial profile close to the foil band is very narrow, with a FWHM of ∼0.6 mm after 0.5 mm of free flight. The plume of desorbed molecules

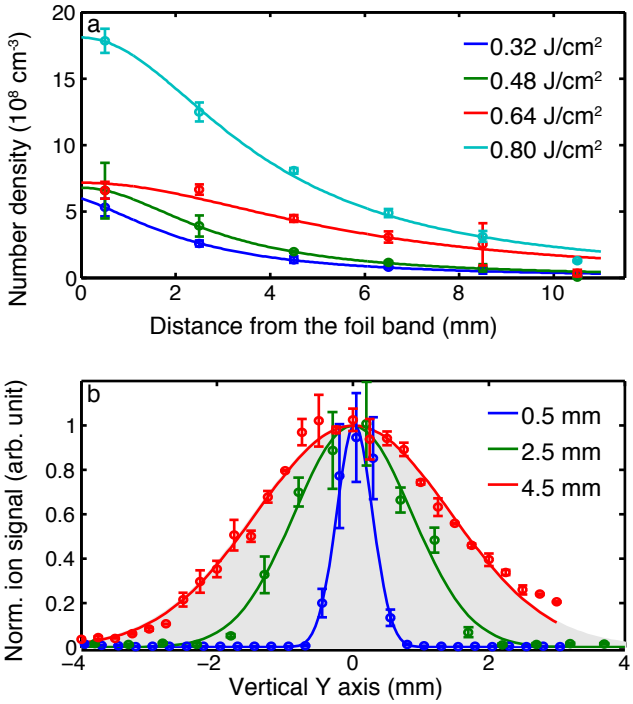

Figure 4.3: (a) Parent ion number density as a function of distance from the foil band, showing inverse-square law behavior. (b) Transverse profile of the molecular plume at three distances from the foil band. Gray shading corresponds to the measured acceptance of the TOF spectrometer, such that the measurement at 4.5 mm does not represent the actual spatial extend of the plume, but the limits of the experimental acceptance. Solid lines correspond to Gaussian fits to the data.

then rapidly spreads out, reaching a FWHM of around 2 mm after 2.5 mm propagation and within 4.5 mm of free flight the extent of the plume exceeds the spatial acceptance of the TOF ion optics (indicated by the gray shading in Figure 4.3 b), such that no accurate data can be measured at larger separations. This rapid diffusion of the plume in space is consistent with the fast drop in density observed as the distance between the foil band and the interaction point is increased, Figure 4.3 a, and indicates rapid diffusion of the molecular plume in space following desorption from a well-defined spot defined by the desorption laser profile. To investigate the longitudinal extend and velocity of the plume of

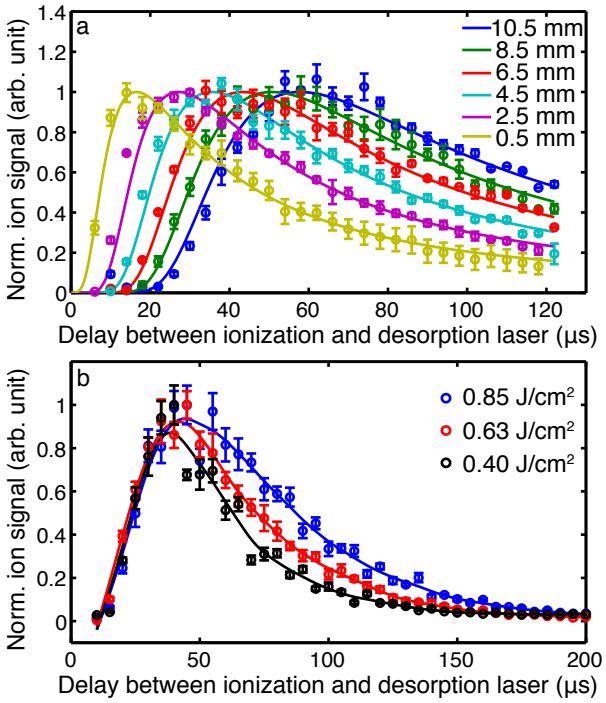

Figure 4.4: (a) Normalized temporal profiles of intact parent ions following desorption with 0.8 J/cm^2, recorded for different distances from the foil band. Solid lines correspond to a fit with a Maxwell-Boltzmann distribution convoluted with the desorption time distribution. (b) Normalized temporal profiles of intact parent ions for different desorption laser intensities and otherwise identical settings, obtained at $z = 6.5$ mm. While the most probable velocity is approximately constant, the larger desorption laser fluence clearly leads to a much broader velocity distribution.

desorbed molecules we measure mass spectra as a function of delay between the desorption and ionization lasers, and at different distances from the foil band. Results for the intact-parent-ion yield following desorption with a fluence of 0.8 J/cm^2 are shown in Figure 5.4 a. Similar data for other desorption fluences are shown in the supplementary data. It is very clear that even when the interaction point is very close to the foil band a broad temporal profile is observed, lasting several tens of µs, much broader than the 8 ns duration of the

desorption-laser pulse. At larger distances from the foil band these distributions widen considerable more, demonstrating that during free flight through the vacuum chamber the plume spreads out also in the longitudinal direction. We identify two physical origins for the observed profiles and their temporal evolution; (i) the desorption process itself that does not release molecules at one instant in time, but with a certain temporal and kinetic energy distribution and (ii) the propagation of molecules in free flight with a certain finite translational velocity distribution. Whereas (i) contains information about the physical desorption mechanism from the foil, the translational velocity spread from (ii) corresponds to the translational temperature in the moving frame of the molecules.
Assuming an equilibrated thermal distribution of molecules in the moving frame, we can model the velocity distributions with a modified Maxwell-Boltzmann distribution, where we have introduced the parameter $v_{0,z}$ as a velocity offset (or stream velocity) in the z-direction. This accounts for the forward momentum by the desorption process [106, 107],

$$f(\vec{v}) = \left(\frac{m}{2\pi k_\mathrm{B} T}\right)^{3/2} e^{\frac{-m\left(v_x^2+v_y^2+(v_z-v_{0,z})^2\right)}{2k_\mathrm{B}T}} \,\mathrm{d}v_x\,\mathrm{d}v_y\,\mathrm{d}v_z. \tag{4.1}$$

Here, m denotes the molecular mass, v_x, v_y, and v_z the velocity components along the axes as defined in Figure 3.2, k_B the Boltzmann constant and T the equilibrium translational temperature of the plume in the moving frame of reference. We can simplify this expression further by considering the actual volume of the plume probed in the experiment. For these measurements the ionization laser was placed vertically in the transverse center of the plume, $y = 0$. Due to the small spot size of the laser (100 µm), $v_y = 0$ can be assumed for the probed molecules. Similar arguments hold for the other transverse direction, x. While the Rayleigh range of the ionization laser ($z_R \approx 38$ mm) is non-negligible compared to the plume dimensions, the focal point was located in the center of the plume and hence the *average* velocity in the x direction is also zero. Taking these simplifications into account and re-normalizing the distribution we obtain

$$f(v) = f(v_z) = \sqrt{\frac{m}{2\pi k_\mathrm{B} T}}\, e^{\frac{-m(v_z-v_{0,z})^2}{2k_\mathrm{B}T}} \,\mathrm{d}v_z. \tag{4.2}$$

Since the experiment does not measure velocities directly, but rather the time t it takes molecules to travel a certain distance l, we can substitute for $v_z = \frac{l}{t-t_0}$, where t_0 accounts

for any temporal offset from the desorption process.

$$f(t) = \begin{cases} 0 & \text{if } t \leq t_0 \\ \frac{l}{(t-t_0)^2}\sqrt{\frac{m}{2\pi k_\mathrm{B} T}}\, e^{\frac{-m\left(\frac{l}{t-t_0}-v_{0,z}\right)^2}{2k_\mathrm{B}T}}\,\mathrm{d}t & \text{if } t > t_0 \end{cases} \tag{4.3}$$

While this simplified Maxwell-Boltzmann picture describes the velocity distribution resulting from the finite translational temperature of the molecular plume, it does not take into account the broad distribution of desorption times from the foil band. Since so far no quantitative model is available to describe this desorption process accurately, we take the experimental data measured closest to the foil band, here 0.5 mm, as a measure of the desorption time distribution. While this distribution has already been influenced by a short free-flight propagation, it is nonetheless the one that most closely resembles the *actual* time-dependence of the desorption process. Given the measured plume velocities, it takes around 2 µs for the propagation of 0.5 mm, whereas the observed temporal distributions are significantly wider, justifying this assumption.

To fit the measured data from Figure 5.4 a, we numerically convolute this experimental temporal desorption distribution with the Maxwell-Boltzmann model of the free-flight propagation. We then perform a global fit of the data for all propagation distances l simultaneously using a common temperature T and offset velocity $v_{0,z}$, while we introduce only a single linear scaling parameter for the different data sets. The latter essentially accounts for the drop in intensity along the probed center-line of the plume. The results of this fit for a desorption laser fluence of 0.8 J/cm^2 are shown as solid lines in Figure 5.4 a, with data for other laser fluences provided in the appendix. The obtained translational temperatures and forward velocities are summarized in Table 4.1.

Table 4.1: Measured translational velocities and temperatures in the moving frame for different desorption laser intensities.

Desorp. Fluence (J/cm^2)	T (K)	$v_{0,z}$ (m/s)
0.32	594	233
0.48	679	234
0.64	715	265
0.80	758	224

We observe a strong, nearly linear, dependence of the translational temperature of the molecular plume on the fluence of the desorption laser. Even at the lowest fluence used a translational temperature of nearly 600 K is obtained. In the current experimental setup using strong-field ionization we cannot measure the internal (vibrational or rota-

tional) temperature directly. However, given the large density of states in systems such as phenylalanine, and the microsecond timescales of the desorption process, we can assume a large degree of thermalization between the different degrees of freedom. Thus the measured translational temperatures can be considered as a good indicator of the internal temperature of desorbed molecules.

Unlike the temperature, the observed forward velocity appears to be approximately constant for the different desorption laser fluences. The slightly elevated velocity for the measurement at 0.64 J/cm^2 could be due to instabilities in the sample preparation for this measurement, as mentioned above. Similar observations of identical forward velocity have been previously reported [24, 35]. This invariability of the velocity with desorption laser fluence suggests that this might be determined by material properties of the substrate and the molecular sample.

Figure 5.4 b shows the yield of intact parent ions as a function of desorption laser-ionization laser delay for different desorption fluences. While the peaks of the distribution overlap in time the distribution is significantly broader for higher fluences. These observations fully support our finding of a constant translational velocity, but increasing translational temperature as the desorption laser fluence is increased (*vide supra*).

4.3.3 Molecular Fragmentation

In how far the observed fragmentation is due to the desorption or the strong-field ionization process is hard to assess from the mass spectra in Figure 5.1 alone. In order to disentangle these contributions, we collect mass spectra for different ionization and desorption laser intensities.

Figure 4.5 a shows the ion yield for the PA parent and the three dominant fragments as a function of ionization laser intensity, with all ion channels showing a steep increase with increasing laser intensity. These data were fit with a power-law dependence of the form $A \times x^n$. Figure 4.5 b further shows the ratio of fragment-to-parent ion intensities for the three dominant fragments, i. e., comparing the relative intensities of the two respective channels. We observe only a very slight increase in fragmentation as the laser intensity increases, in good agreement with previous studies suggesting that strong-field ionization induced fragmentation is very sensitive to the employed pulse duration, but not the intensity [28].

Figure 4.5 c shows the dependence of ion yields on the intensity of the desorption laser and Figure 4.5 d the corresponding fragment-to-parent ratios. The overall measured ion intensities are again well described by a power-law fit and show a steep increase for higher intensities, especially noticeable for fragment ions. This is confirmed by the fragment-to-

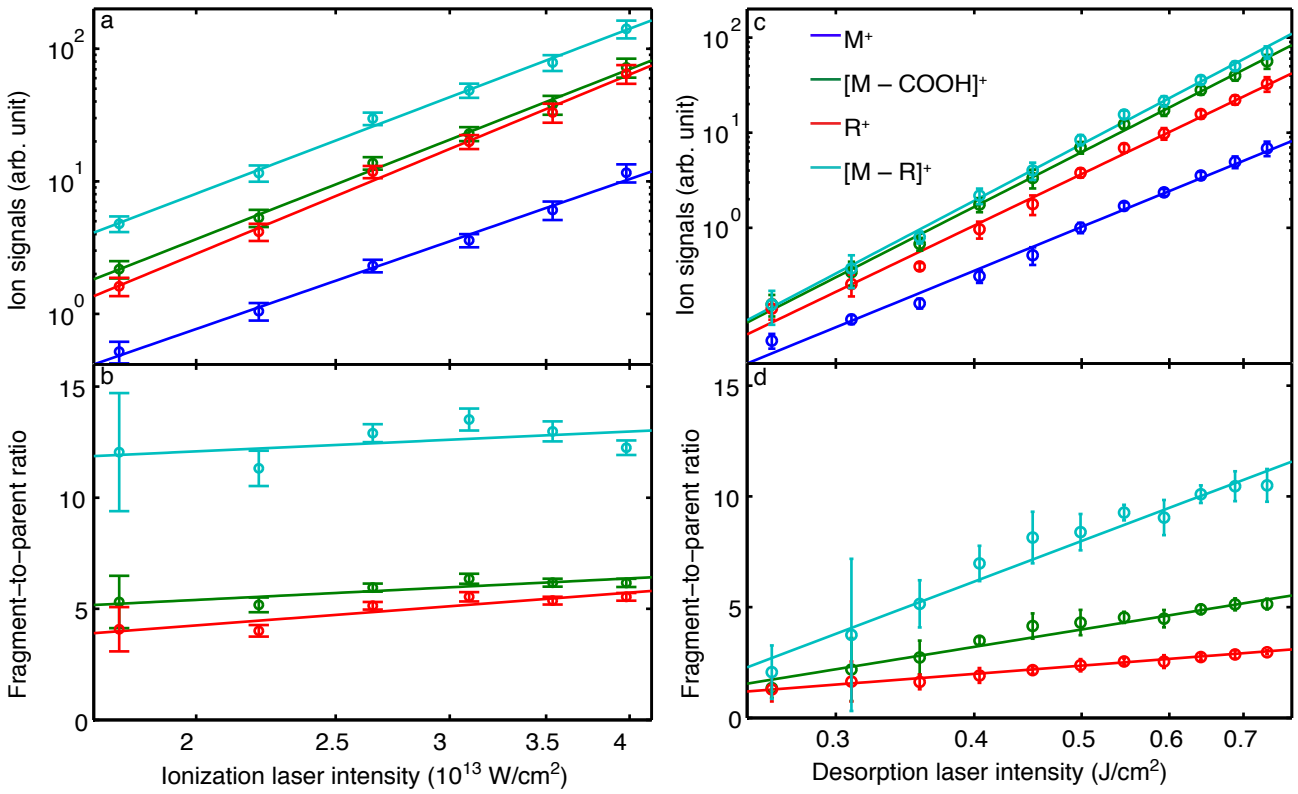

Figure 4.5: Ion-yield signals (a, c) and fragment-to-parent ratios (b, d) as a function of ionization laser intensity (a, b) and desorption laser intensity (c, d). Color coding for all graphs is given in panel c; see Figure 5.1 for assignment of the mass peaks. Solid lines correspond to power-law fits.

parent ratios, which also significantly increase with laser intensity, indicating enhanced fragmentation. Thus, the desorption-laser interaction clearly induces fragmentation, either directly during the desorption process or thereafter, but prior to ionization, i. e., as molecules travel through the vacuum chamber toward the interaction point. To test the latter, we recorded mass spectra at different distances behind the foil band, changing the laser-laser delay such that we always probe the highest density part of the molecular plume, i. e., we follow the center of the plume as it travels through the vacuum chamber.

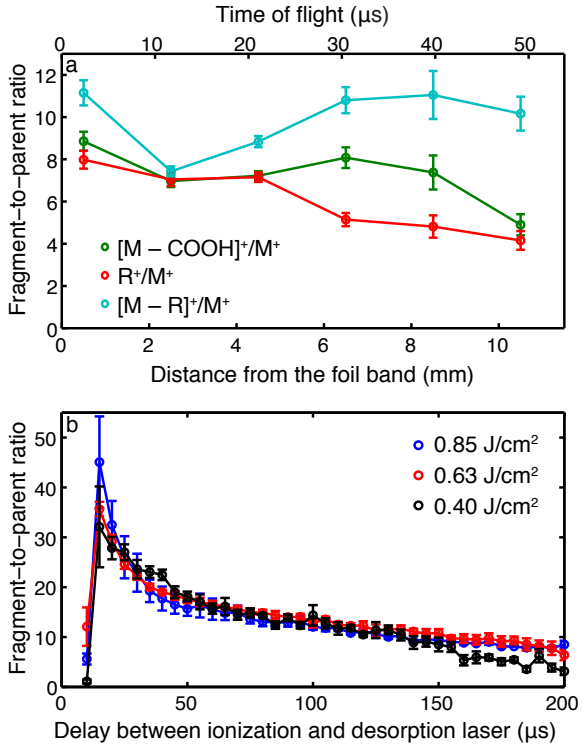

Figure 4.6: (a) Fragment-to-parent ratio recorded at the peak of the molecular plume density for different distances behind the foil band. No significant increase in fragmentation is observed as the plume travels through the vacuum chamber. (b) Fragment-to-parent ratio throughout the molecular plume recorded 6.5 mm behind the foil for different desorption laser intensities. Molecules desorbed shortly after the arrival of the desorption laser show significantly higher fragmentation than molecules desorbed later.

This data is shown in Figure 4.6 a, collected for distances of 0.5–10.5 mm between the foil band and the interaction point, which corresponds to flight times of around 0–50 µs. Over this distance we observe no significant increase in fragmentation. This indicates that the observed fragmentation occurs on much faster timescales, i. e., most likely during the desorption process itself, either while molecules are still attached to the metal substrate or very shortly after desorption into the gas-phase.

We now consider the distribution of fragments within a single plume coming from the foil band, i. e., if the fragmentation changes depending on which part of the plume is observed. This is shown in Figure 4.6 b, where we plot the fragment-to-parent ratio for the most abundant molecular fragment as a function of desorption-laser-to-ionization-laser delay for a fixed distance from the foil band, i. e., 6.5 mm. We observe an initial peak in the fragment-to-parent ratio at the onset of desorption, i. e., the "front" part of the molecular plume, which then decreases on a timescale of tens of microseconds. These timescales are consistent with thermal processes, in particular we associate the observed distribution with the rapid heating of the foil band by the nanosecond laser pulse, causing increased fragmentation, followed by slow dissipation of the thermal energy, i. e., cooling down of the front surface and, hence, reduced fragmentation.

Further evidence that the fragmentation occurs during the desorption process and that it is of a thermal nature comes from the comparison of the fragment-to-parent ratios throughout the plume for different desorption laser fluences, also shown in Figure 4.6 b. These clearly show that the highest degree of fragmentation occurs for the most intense desorption laser pulse. This is also consistent with the higher translational temperatures derived for these conditions. Once the foil band cools down, i. e., at longer desorption-laser-to-ionization-laser delays, the fragment-to-parent ratio approaches an asymptotic value independent of initial desorption conditions.

4.3.4 Nature of the Desorption Process

Several possible mechanisms have been suggested in the literature for the underlying physical processes occurring in the LIAD process [17, 18, 35, 104]. It is important to note that the experimental conditions for the different published LIAD-based molecule sources in the literature are very different; pulsed [28,35] and continuous [30,108] desorption lasers are used and sample preparation methods vary greatly, from the thick sample layer used here of ∼500 nmol/cm^2 [108,109], to intermediate thicknesses of tens of nmol/cm^2 [23,24], to near-monolayer coverage in other studies [35]. As such, we do not aim to provide a general model for the LIAD mechanisms, but seek to explain our observations and compare these with previous studies where applicable.

One of the suggested desorption mechanisms, and indeed the origin of the term "acoustic desorption" [17,18], is the direct momentum transfer from a shock wave induced by the desorption laser in the foil band to the sample molecules. The data presented here firmly rules out this mechanism for our molecule source. We observe a slow rise in molecular signal on the order of ∼10 µs, see Figure 5.4, which is not compatible with molecules

being “shaken off” by an impulse traveling through the foil, as this should lead to a sharp sudden onset of signal as the impulse reaches the front surface, followed by an immediate drop as the impulse is reflected on the surface. Additionally one might expect to observe a periodic revival of signal as the impulses bounces back and forth within the metal foil. We observe no evidence for this behavior in our data. Furthermore, the travel time for a mechanical wave through a 10 µm tantalum foil is approximately 2 ns [110], significantly shorter than the delay we observe between the desorption laser impacting on the foil and molecules being desorbed. A purely acoustic desorption mechanism would, furthermore, not explain the observed increase in fragmentation for increased desorption laser fluences. Similar observations have been made previously for a pulsed LIAD setup, and the “shake off” mechanism similarly discredited [35].

The other conceptually simple mechanism behind the observed desorption of molecules is a simple thermal one; the incident laser pulse heats up the material from the backside and this thermal energy then diffuses to the front of the foil where it heats up molecules and they eventually desorb. However, the observation that the velocity and, therefore, the kinetic energy of desorbed molecules is independent of the incident desorption laser power and thus surface temperature is not compatible with a purely-thermal desorption model.

The observation that the kinetic energy of desorbed molecules is independent of desorption laser fluence indicates that this is determined by material properties of the foil substrate and/or the molecular sample. This observation, along with the increase in translational temperature in the moving frame, is consistent with a desorption model proposed by Zinovev et al. [35]. They explain the LIAD process by an introduction of surface stress between the substrate and the molecular sample – located in isolated islands on the substrate – due to the acoustic and/or thermal wave created by the desorption laser. This surface stress can lead to elastic deformation, decomposition, and cracking of sample islands on the foil band and, eventually, to desorption of molecules. In this conceptual model the kinetic energy transferred to a desorbing molecule is independent of the total incident laser power, and rather depends on the intrinsic characteristics of a given sample island and substrate. A higher laser fluence leads to the introduction of more surface stress and the formation of more cracks and deformation sites, leading to an increase in molecular signal, but does not influence the amount of kinetic energy per molecule. At the same time we note that due to thermal conductivity the higher temperature of the substrate reached for higher desorption laser fluences will also heat up deposited sample molecules due to thermal conduction, leading to internally hotter molecules, increased fragmentation as well as higher translational temperatures.

While it is difficult to theoretically model the amount of energy transferred to each desorbed molecule, Zinovev et al. provide a simple formula to estimate the energy per analyte molecule based on material properties and thermal stress theory [35]. Based on this we estimate 25 – 100 meV of energy per molecule for temperature differences of $\Delta T = 100$ – 200 K. [2] This is well within the range of the measured kinetic energy per molecule which is, based on the average velocity observed, around 50 meV. Thus, our data is fully supportive of the proposed surface stress model.

4.4 Conclusion

We presented an advanced LIAD source for the preparation of gas-phase samples of labile molecules, designed for the use at central-facility light sources such as free-electron lasers. It features a prolonged continuous measurement time through automatic sample replenishment using a long foil band, as well as a fixed interaction point. Uniform sample preparation on the long substrate was achieved using an aerosol spraying method based on thin liquid jets. We have characterized the new source using phenylalanine as a sample molecule and strong-field ionization as a universal probe method. We observe a significant fraction of intact molecules being desorbed from the foil, with number densities around 2×10^8 cm^{-3} close to the foil band. Due to fragmentation processes induced by the femtosecond laser probe, this should be treated as a lower limit. The spatial extend of the molecular plume rapidly spreads out from the point of desorption, leading to a corresponding drop in density with increasing distance from the foil band. The plume forward translational velocity and temperature in the moving frame are derived by convoluting a Maxwell-Boltzmann velocity distribution with the initial temporal profile near the foil band. The forward velocity, and hence kinetic energy, of molecules desorbed from the foil does not depend on the desorption laser intensity. In contrast to this, the translational temperature clearly increases with increasing desorption intensity. We investigated the fragmentation processes and observe increased fragmentation at higher desorption laser intensity, consistent with the translational temperature behavior. Furthermore, we show that the amount of fragmentation depends on the time of desorption from the foil: shortly after the laser pulse molecules are observed to be hottest, and subsequently they cool down on thermal timescales (10s of µs) as the substrate itself cools down. These observations are fully supported by the previously proposed surface-stress model of the LIAD process.

[2] We evaluated the energy release per molecule based on the known physical constants for anthracene [111], since data for PA was not available. The thermal expansion coefficient of the film is assumed to be 2.8×10^{-4} K^{-1}.

Our characterization measurements show that our new source produces a stable high-density signal of intact molecules in the gas-phase. With automatic sample replenishment it provides very long continuous measurement times. The produced molecular plume is well suited for further gas-phase experiments and manipulation, and work is currently underway towards integrating this source into a buffer-gas-cooling setup for the production of cold molecules [112], which can then be further manipulated using electric fields [8]. One could also envision to make use of this desorption technique for the entrainment of molecules into supersonic beams, similar to matrix-assisted laser desorption approaches [67]. Furthermore, we are working towards a better understanding of the desorption mechanism and its dependence on the sample layer thickness and sample itself in order to successfully apply our new source to the gentle vaporization of more labile biological samples.

5 Laser-Induced Acoustic Desorption of Thermally Stable and Unstable Molecules [1]

We evaluated the effect of the laser-induced acoustic desorption (LIAD) process on thermally stable and unstable biomolecules. The thermally stable adenine molecules were prepared fully intact in the gas-phase, while thermally labile glycine molecules exhibited some fragmentation. We observed a rise in translational temperature of the produced molecules plume with increasing desorption laser intensity, while its forward velocity was invariant with respect to the desorption laser intensity for both glycine and adenine. The forward kinetic energy was in the range of the surface stress energy, which supports the previously proposed stress-induced desorption model for the laser-induced acoustic desorption process.

5.1 Introduction

Laser-induced acoustic desorption [16, 17] is a promising technique to bring thermally labile, light sensitive and non-volatile molecules into gas phase. It relies on samples being deposited as a thin layer on a metal foil, typical foil thickness of around 10 µm, which are then desorbed by irradiating the backside of the foil, i. e., the side without sample, with a nanosecond laser. As this method avoids direct contact between the desorption laser and sample, it is especially suitable for light-sensitive and labile samples and has been demonstrated for bringing biological systems ranging from amino acids [28–30, 113], through peptides [23–25] and even entire viruses, bacteria and cells [20, 27] into

[1] This chapter is based on the paper *Laser-Induced Acoustic Desorption of Thermally Stable and Unstable Molecules*, Zhipeng Huang, Daniel A Horke, and Jochen Küpper, *Under review*, arXiv: 1811.05925 [physics].
I conducted the experiments. Together with Daniel A. Horke, I conducted the data analysis. Together with all other authors, I discussed the results and wrote the article.

the gas-phase. Such LIAD-based molecule sources have been applied to mass spectrometry studies [19–21,114], gas-phase chemical reactions [115,116], and even attosecond dynamics experiments [28–30]. They are further promising large-molecule sources for use in matter-wave interferometry [117, 118] and single-particle imaging experiments at free-electron lasers [3, 119].

We have previously demonstrated and characterized our newly designed LIAD source, featuring constant sample replenishment using a tape-drive to deliver fresh sample, and prepared a high-density plume of phenylalanine [113]. We observed that increasing the pulse energy of the desorption laser lead to an increase in the observed fragmentation, as studied using strong-field ionization. It furthermore lead to a significant increase in the translational temperature of desorbed molecules. In this contribution we investigated how the LIAD source parameters, such as desorption laser intensity and desorption-ionization timing, affected the produced molecular plume for thermally stable and thermally unstable biological molecules, using adenine and glycine as prototypical examples [120, 121]. Our results confirmed the previous assignment of a desorption model based on surface stress on sample islands deposited on the foil, as evidenced by the combination of an invariance of the molecular plume velocity on the desorption laser intensity, but an increase of the translational temperature [35, 113]. For the thermally labile glycine sample we found that fragmentation can occur during the propagation of the molecular plume in the vacuum chamber following desorption. These molecules were found to possess translational temperatures above the decomposition threshold. If there is a full thermalization of internal and external degrees of freedom, which seems reasonable given the involved microsecond timescale desorption process, this would explain the increased fragmentation during free flight propagation for thermally labile glycine molecules after desorption.

5.2 Experimental Method

Detailed descriptions of our experimental setup and sample preparation method were given in the chapter 3. Briefly, samples were deposited on the front surface of a 10 µm thick, 10 mm wide and 1 m long tantalum foil band. In order to create a stable coverage of sample on the foil, sample was aerosolized using a gas-dynamic virtual nozzle (GDVN) [36, 37] and this aerosol deposited on the foil, where it sticks and rapidly dries out. The surface coverage of adenine and glycine on the foil was around 600 nmol/cm^2 and 400 nmol/cm^2, respectively, as determined by weighing foil bands before and after sample deposition. To desorb molecules, the back surface of the foil was irradiated by a 355 nm laser pulse with 8 ns duration at a repetition rate of 20 Hz, focused to a spot size of around 300 µm

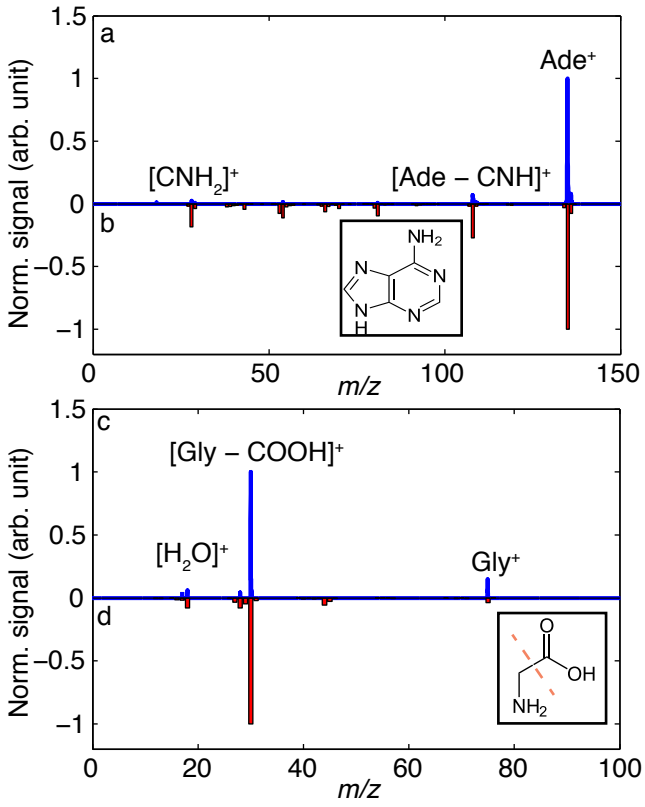

Figure 5.1: Mass spectrum of adenine and glycine recorded using strong-field ionization with a field strengths of 4×10^{13} W/cm^2(blue) and electron impact ionization (red) [105]. Both are normalized to the dominant mass-to-charge ratio peak.

(FWHM) on the foil. Sample was constantly replenished during operation by forwarding the foil band with a velocity of ~ 50 µm/s. Desorbed molecules were ionized using strong-field ionization (SFI) induced by a focused femtosecond (40 fs) Ti:Sapphire laser focused to a spot size of around 100 µm, corresponding to typical field strengths of 4×10^{13} W/cm^2. Produced ions were detected by a linear time-of-flight mass spectrometer (TOF-MS).

5.3 Results and Discussion

Typical time-of-flight mass spectra of adenine and glycine desorbed via LIAD are shown in Figure 5.1 and are compared to literature spectra obtained using electron-impact ionization (EI) of thermally evaporated samples [105]. Both spectra were normalized to their respective dominant ion peak, i. e., the parent ion peak at 135 u for adenine and the dominant fragment peak at 30 u for glycine. The adenine spectra clearly demonstrate the production of intact adenine in the gas-phase using LIAD, with very little fragmentation. For glycine, however, fragmentation was observed for both our and the reference spectrum. We note that this fragmentation is not necessarily inherent to LIAD, since both SFI and EI can induce fragmentation during or after the ionization process [28, 113, 122]. Nonetheless, using LIAD combined with SFI a significant contribution from intact glycine was present. The mass spectra showed no evidence for the formation of molecular clusters or ablation of metal atoms or clusters from the foil band [113].

In order to investigate how the desorption laser intensity affects the fragmentation behavior for thermally stable and labile molecules, respectively, we collected mass spectra for adenine and glycine under different desorption laser intensities. Molecules were ionized using SFI 4.5 mm behind the foil band. Figure 5.2 a,c shows the respective parent and dominant fragment ion yields as a function of desorption laser intensity. These data were fit with a power-law dependence of the form $A \times x^n$, and all ion channels showed a corresponding increase with increasing laser intensity. As the SFI process can induce fragmentation, we use the ion yields of dominant fragments divided by the ion yields of parent molecules (i. e., fragment-to-parent ratios) to illustrate the effect of LIAD parameters on the fragmentation. Figure 5.2 b,d shows the fragment-to-parent ratios for adenine and glycine as a function of desorption laser intensity and we observed only a slight linear increase in fragmentation as the desorption power is increased. Both thermally stable and unstable molecules, therefore, behave similar with increasing desorption laser intensity, confirming the non-thermal nature of the desorption process.

To investigate whether further fragmentation occurred after desorption, i. e., during propagation of the molecular plume through the vacuum chamber, we recorded mass

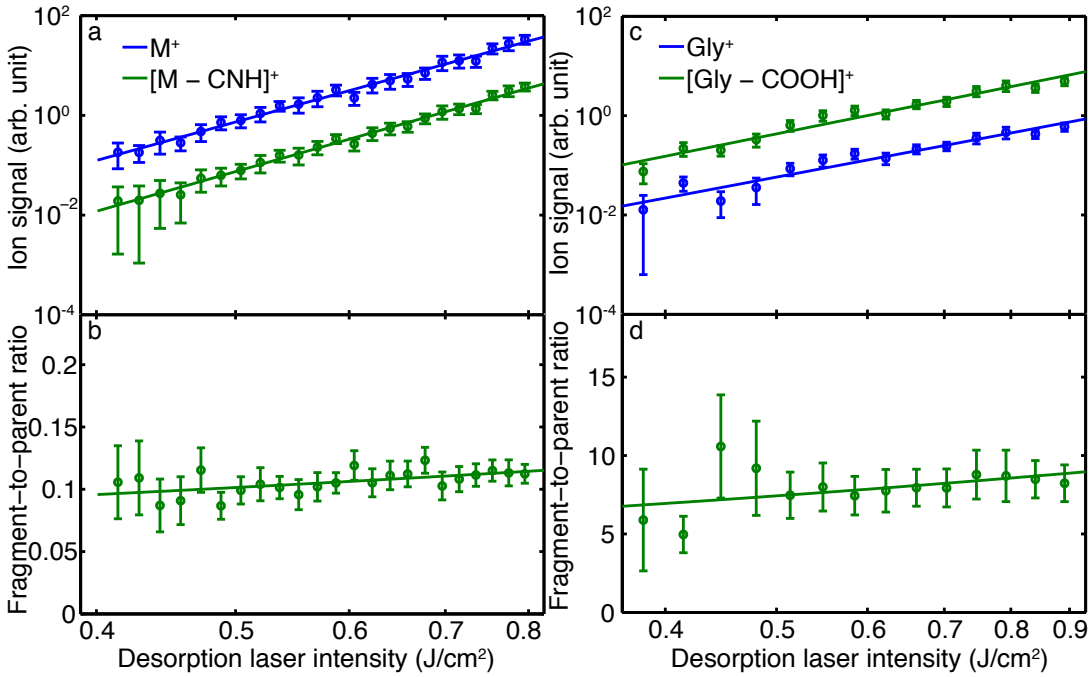

Figure 5.2: Parent and dominant fragment ion yields (a,c) and fragment-to-parent ratios (b,d) as a function of desorption laser intensity for adenine (a,b) and glycine (c,d). Data was recorded using strong-field ionization 4.5 mm behind the foil band.

spectra at different distances behind the foil band. At each distance the delay between ionization laser and desorption laser was changed, such that we always probed the highest density part of the plume, i. e., we followed the peak of the plume as it travels. This data is shown in Figure 5.3 a,b, where we plot the fragment-to-parent ratio for distances of 0.5–12.0 mm between the foil band and the interaction point. Figure 5.3 a shows the behavior for adenine, using the dominant fragment at 108 u, corresponding to the loss of –CNH from intact adenine. We observed a decrease of the fragment-to-parent ratio with distance from foil band, indicating that the peak number density of fragments decreased relatively to the adenine parent. At the same time the absolute densities for parent and fragment should decrease with increasing distance. We attribute the observed behavior to different relative velocity distributions for fragments and intact molecules. Fragments appear to be traveling at higher velocities, likely due to the additional kinetic energy released in the fragmentation process, leading to the observed decrease in the fragment-to-parent ratio of adenine with increasing distance from the foil band. This indicates that there was no further fragmentation of adenine during propagation.

The behavior observed for glycine is markedly different, as shown in Figure 5.3 b. Here, the relative population of the dominant fragment at 30 u increased during propagation, indicating that further fragmentation occurred during free flight of the molecules

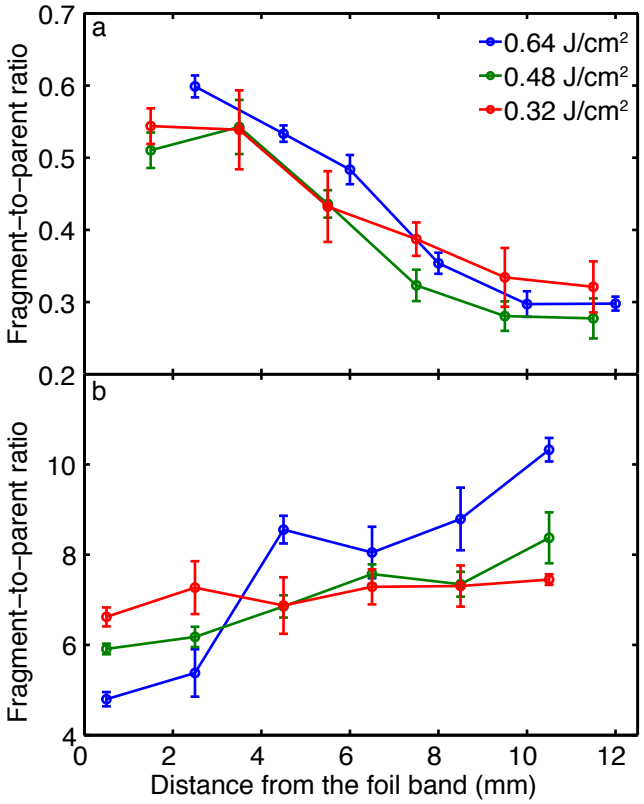

Figure 5.3: Fragment-to-parent ratio of adenine (a) and glycine (b) as a function of distance from the foil band for the highest density part of the plume.

through the chamber. We note that one might expect fragments and intact glycine to propagate at different velocities, as observed for adenine, such that the fragmentation during propagation might be even more significant than the data in Figure 5.3 b suggests. These two competing effects also explain the unclear variation in a corresponding measurement of the fragmentation during propagation of phenylalanine following LIAD [113]. The different behavior for adenine and glycine suggests a thermal decomposition during free flight propagation as the origin of the enhanced fragmentation. This will be investigated further below, where we asses the translational temperature of desorbed molecules.

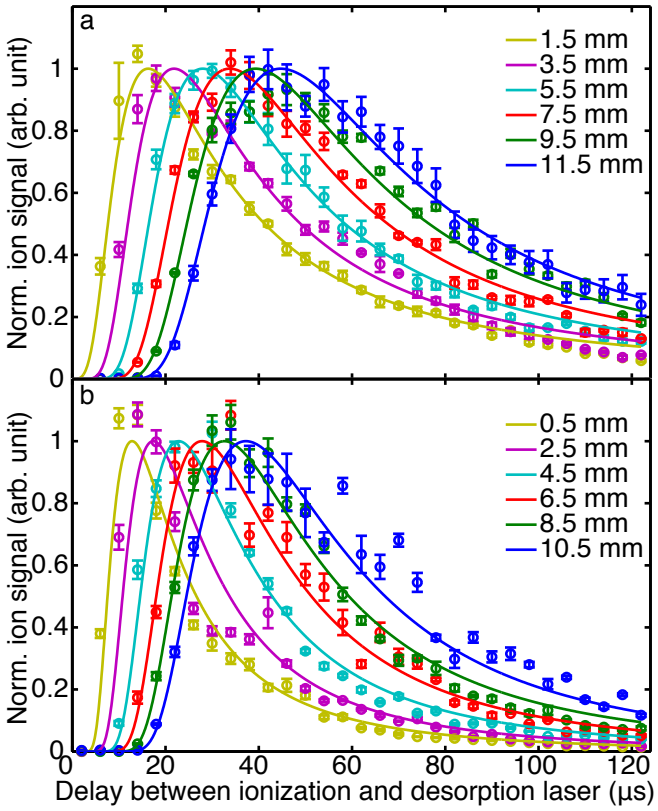

Figure 5.4: Adenine (a) and glycine (b) plume temporal distribution measured at different distances from the foil band for a desorption laser fluence of 0.48 J/cm^2.

In order to evaluate the translational forward velocity and translational temperature of the plume, we recorded mass spectra for different ionization-desorption laser delays and at different distances from the foil. These data, shown in Figure 5.4, were then modeled by a Maxwell-Boltzmann distribution convoluted with the initial temporal distribution from the LIAD process [113]. The shown data was recorded for a desorption laser fluence of 0.48 J/cm^2, profiles for other fluences are shown in the supplementary materials. All experimental data were fitted globally for all propagation distances with a

Table 5.1: Derived translational forward velocities $v_{0,z}$ and translational temperatures T in the moving frame for adenine and glycine at different desorption-laser fluences.

Fluence	Ade		Gly	
(J/cm^2)	T (K)	$v_{0,z}$ (m/s)	T (K)	$v_{0,z}$ (m/s)
0.32	494	365	441	337
0.48	516	369	496	338
0.64	521	384	698	355
0.80	523	380	745	340

common temperature T and forward velocity $v_{0,z}$. The resulting fit is shown as solid lines in Figure 5.4. The extracted forward velocity and translational temperature for different desorption laser intensities are summarized in Table 5.1. We found that the forward velocity of both, adenine and glycine, plumes was invariant with respect to desorption laser intensity, as previously observed for other molecules [35, 113]. Similarly we confirmed the previous finding that the translational temperature increases with desorption laser intensity, for both, adenine and glycine. However, while the former only shows a very modest increase over the laser fluence range investigated, the glycine translational temperature was found to increase significantly. For all but the lowest desorption fluence, the extracted translational temperature for the glycine plume was above its thermal decomposition temperature, which is on the order of $\sim 485 - 513$ K [121]. The translational temperatures for adenine, however, were much below its decomposition temperature of 582 K [120]. While we have no definitive explanation for the differences in observed translational temperature, we think that this is due to different thermal properties, such as heat transport, from the metal foil to the sample during the desorption process. Furthermore, we note that the different thicknesses of the sample layers will influence this. Nonetheless, these results rationalize the observed fragmentation behavior following desorption from the foil band shown in Figure 5.3: the thermally unstable glycine appears to fragment during propagation, while for adenine no additional fragmentation was observed.

The observation of a constant plume velocity, but increasing translational temperature, as well as only a modest increase in fragmentation with increasing desorption laser fluence, is a clear indicator for a desorption process based on surface stress between the substrate and the deposited sample [35, 113, 123]. The forward velocity of the molecular plume, i. e., its kinetic energy, is hence determined by material properties of the substrate and sample. From our measurements we extracted a forward kinetic energy, based on the average velocity, of around 90 meV for adenine and 45 meV for glycine. This is consistent with the previously observed kinetic energy for phenylalanine under identical conditions, around 50 meV [113], and within the range of simple estimates of the stress energy of

25–100 meV [35, 111]. The kinetic energy of desorbed molecules is essentially a measure of the interaction energy between the deposited molecules and the metal foil. In a very qualitative picture it is easy to rationalize how adenine with its highly delocalized π-system has a stronger interaction with a metal surface than glycine, with phenylalanine somewhere between the two.

An important parameter for the desorbed plume is characterized by number density. Our calibrated multi-channel plate (MCP) detector can count the absolute number of molecules. By knowing the interaction volume, we can derive the number density of our plume. Figure 5.5 shows how the desorbed plume number density changes with distance from the foil band at three different desorption laser intensity. It obeys an inverse square function due to the large Rayleigh length of ionization laser ($z_R \approx 38$ mm) compensating one dimension expansion. Ade peak number density is around 2.0×10^9 cm^{-3} and Gly peak number density is around 8.5×10^8 cm^{-3} when desorption laser intensity is around 0.64 J/cm^2 and $z_x = 0.5$ mm.

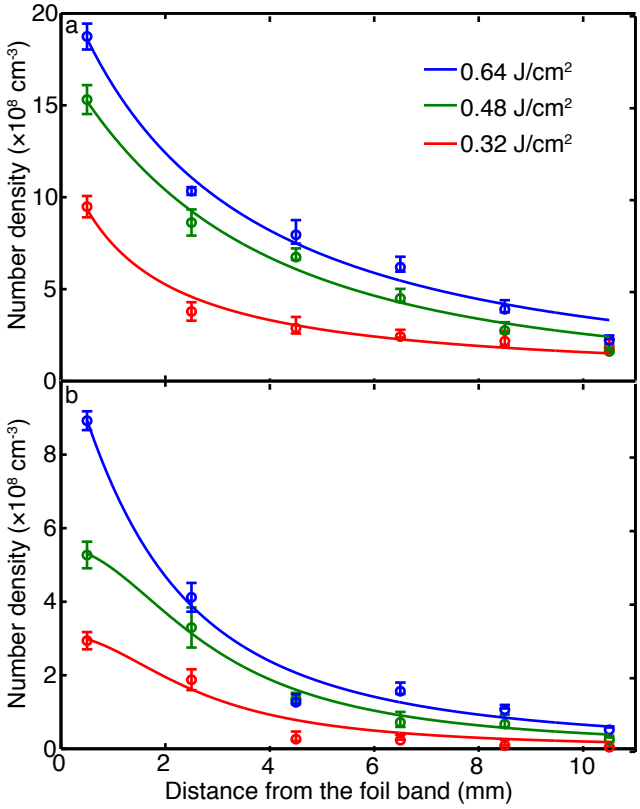

Figure 5.5: Number density of adenine plumes (a) and glycine plume (b) as a function of distance from foil band at different desorption laser intensity.

Lastly we would like to point out the large variation in experimental setups and parameters used for LIAD experiments by different groups. There are furthermore many

different ionization sources coupled to LIAD, some of which, such as resonance-enhanced multiphoton ionization (REMPI), are impervious to any fragmentation and this will not be observed. This variety implies that the discussed observations and trends might not be universally applicable to all LIAD studies. For example, several studies utilized the second harmonic of an Nd:YAG laser (532 nm) for desorption of molecules from a Titanium foil, which has a reflectivity of around 93 % at this wavelength [124]. In contrast to this, utilizing the third harmonic (355 nm) on a Tantalum foil, the reflectivity is only around 65 %. Thus even for seemingly similar incident laser fluxes the energy deposited into the foil and/or sample can vary significantly. Nonetheless, the present study provides further much needed insight into the LIAD process. We corroborate a desorption process based on surface-stress islands and further show that, due to the microsecond timescale of LIAD, there is a strong coupling of translational and internal degrees of freedom that can lead to fragmentation of analytes if the deposited energy, and corresponding translational temperature, is too high.

5.4 Conclusion

We demonstrated the use of LIAD for the production of gas-phase samples of adenine and glycine, prototypical examples of thermally stable and unstable biological molecules, respectively. We showed that the high translational temperatures of molecules following desorption can lead to further fragmentation of thermally unstable systems as they travel through the vacuum chamber, indicating a strong coupling between internal and external degrees of freedom in the desorbed samples. Measurements of the translational temperature and molecular velocity distributions confirmed this, and showed that indeed glycine is produced with a temperature in excess of its decomposition threshold. The invariance of forward velocities on the desorption laser power further confirmed a desorption model based on surface stress between substrate and sample.

The additional fragmentation of molecules could be avoided if they were rapidly cooled down, for example using buffer-gas cells [112] or entrainment in cold molecular beams, as is commonly done in direct laser desorption [67]. Such experiments are underway in our laboratory and such a cold beam of intact large molecules would enable novel experiments, from controlling large molecules with external fields [8,68] to direct diffractive imaging of single molecules in the gas-phase [3,119].

6 Effects of Sample Layer Thickness on Phenylalanine Plume Properties

6.1 Introduction

Effects of sample layer thickness on properties of gas-phase phenylalanine plumes prepared by laser-induced acoustic desorption are evaluated. Two phenylalanine samples with different thickness were prepared on two same tantalum foil bands. We evaluated the forward velocity and translational temperature of phenylalanine plumes prepared from these two different samples. It shows that the plume forward velocity and translational temperature are dependent on the sample thickness. The temporal profile of plumes prepared from thick sample is broader than thin sample, which is confirmed by the higher translational temperature for the plume prepared from the thick sample. Forward velocity of desorbed plume from thick sample layer is also higher than from thin layer sample. Fragment-to-parent ratio derived from mass spectra was utilized to indicate the foil surface temperature. The results show that a quick temperature rises on the foil after laser shining, which induces a stress between foil band and sample layer due to the different thermal mechanic parameters for foil band and sample layer. Desorption happens when the surface stress can overcome the binding energy between foil band and sample. The maximum of desorption ion yields is nearly 20 µs later than the maximum of fragment-to-parent ratio indicates the desorption is not a simple direct couple desorption process.

6.2 Experimental Method

Detailed descriptions of our experimental setup and sample preparation were presented in chapter 3. The setup features prolonged measurement times and a fixed interaction point. A novel sample deposition method utilizing aerosol spraying provides a uniform sample coverage and hence stable signal intensity. The newly developed setup and novel sample

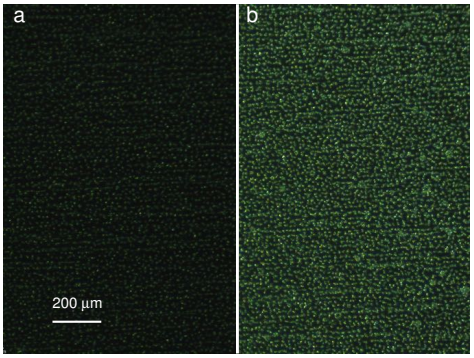

Figure 6.1: Optical microscope images of phenylalanine sample prepared with foil band moving speed at 80 µm/s (a) and 160 µm/s respectively (b).

preparation method enable us characterize the source continuously for a long time with fixed interaction points as well as decent signal to noise ratios. Two phenylalanine aqueous solutions were prepared with same concentration at 0.1 mol/L. They were aerosolized to the foil bands with a ceramic injection-molded GDVN with a liquid inner capillary of 75 µm in diameter. The two foil bands advance with speed at 80 µm/s and 160 µm/s respectively, which leads to two different sample layer thickness. Figure 6.1 shows the optical microscope (Carl Zeiss Stemi 2000) images of prepared phenylalanine samples. The thin and thick phenylalanine layers covered on the foil by aerosol spraying is around 300 nmol/cm^2 and 600 nmol/cm^2 respectively by weighing foil bands before and after depositing sample. The back of the foil is irradiated by a 355 nm laser pulse with 8 ns duration (FWHM) at a repetition rate of 20 Hz. Spot size of the desorption laser on the foil band is around 300 µm (FWHM) focused by a $f = 500$ mm lens with typical laser intensity at 0.48 J/cm^2. The typical replenish speed of the foil band during experiments is around 50 µm/s. The desorbed molecular plumes from the tantalum foil were then characterized with strong-field ionization (SFI) from a focused femtosecond (40 fs) Ti:Sapphire laser [28, 67, 113]. The focused spot size of the ionization laser is around 100 µm with a typical peak intensity of 4×10^{13} W/cm^2. Produced ions were detected by a linear time-of-flight mass spectrometer (TOF-MS).

6.3 Results and Discussion

Figure 6.2 (a) shows normalized temporal profiles of phenylalanine parent molecules desorbed from two sample layers with different thickness. We observed that the plume temporal profile prepared from thick layer is boarder than the plume temporal profile prepared from thin sample layer. The maximum peak of parent molecule ion yields from

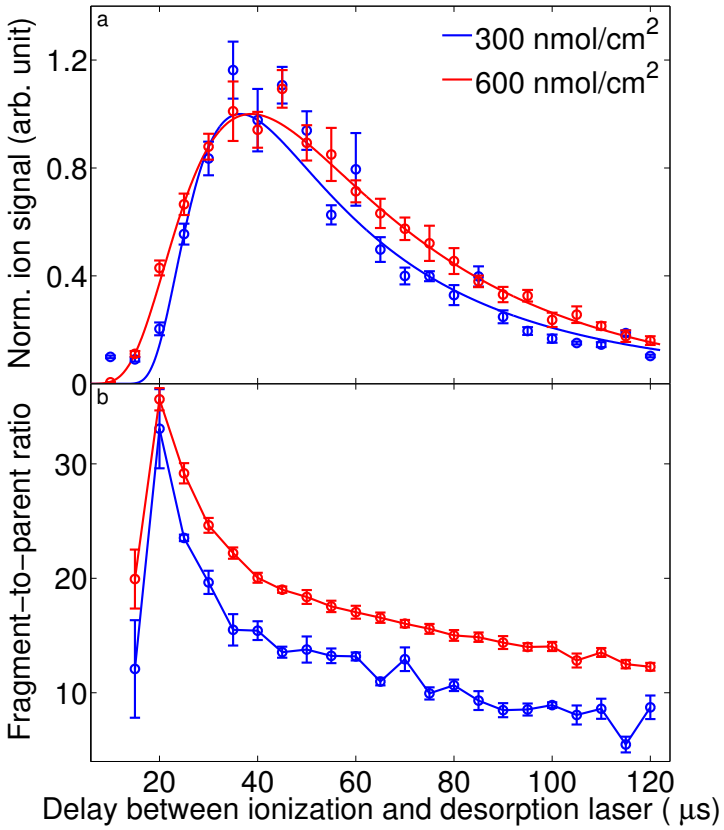

Figure 6.2: Normalized temporal profiles of intact phenylalanine parent ions (a) and temporal profiles of fragment-to-parent ratio (b) prepared from two different thickness layers, following desorption with 0.8 J/cm^2, recorded for distances from the foil band at 4 mm.

thick sample is later than thin sample, which is reasonable due to the longer propagation time for stress wave in thicker sample layer. Figure 6.2 (b) shows the corresponding fragment-to-parent ratio temporal profiles for plumes desorbed from these two different sample layers. Because phenylalanine is thermally labile and sensitive to the temperature, the higher temperature will lead to more fragmentation. As a result, the fragment-to-parent ratio can be used to indicate the foil band thermal temperature. Figure 6.2 (b) clearly shows a fast temperature rising and slow decay after laser shining the back of the foil band. We noticed that the peak time of maximum thermal temperature is around 20 µs earlier than the maximum of parent molecule yields. It indicates that the desorption process is not a direct coupled process. According to the desorption mechanism discussed in chapter 4 and chapter 5, samples were desorbed out of the foil due to the stress between sample layer and foil band. It indicates that the stress intensity reaches maximum later than surface temperature.

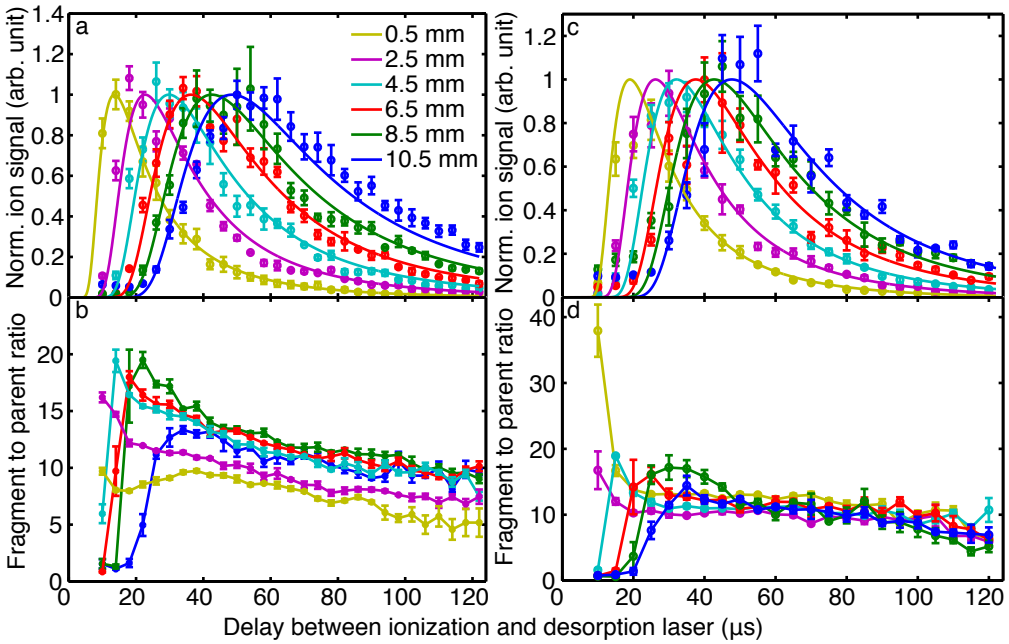

Figure 6.3: Phenylalanine plume temporal distributions and their fragment-to-parent ratio measured at different distances from foil band for a desorption laser intensity of 0.48 J/cm^2. The plumes are prepared from two different samples with surface coverage of 600 nmol/cm^2 (a, b) and 300 nmol/cm^2 (c, d), respectively.

As discussed in chapter 4, we derived the translational forward velocity and translational temperature of desorbed plume by globally fitting the experimental temporal profiles at all propagation distances simultaneously with a common temperature T and forward velocity $V_{0,z}$ by convoluting the Maxwell-Boltzmann model of free-flight propagation to the initial plume temporal distribution. Figure 6.3(a, c) shows normalized

temporal profiles of desorbed plume from two different phenylalanine sample thickness layers measured at six different propagation distances. Solid lines show the fitted data. Table 6.1 shows the derived results of forward velocity and translational temperature of desorbed plumes from two different sample thickness with desorption laser intensity at 0.48 J/cm^2. It clearly shows that the translational temperature of desorbed plumes from thick sample is higher. We also observed that the translational froward velocity of plumes prepared from thick sample is faster than from the thin layer.

Table 6.1: Derived translational forward velocities $v_{0,z}$ and translational temperatures T in the moving frame for phenylalanine plume desorbed from different thickness sample.

Sample coverage (nmol/cm^2)	T (K)	$v_{0,z}$ (m/s)
300	679	234
600	738	311

In order to illustrate the most probable forward velocity from different sample thickness directly, Figure 6.4 (a) shows the time of the maximum parent ion yields probed at different distances from the foil band. Reciprocal of the slope gives the plume most probable forward velocity. It shows that the thick sample has a faster most probable translational velocity, which indicates that the laser-induced stress for thick sample is higher than thin sample. Longer delay between the maximum fragment-to-parent ratio and maximum parent ion yields for thick sample shows that it takes more time to reach maximum desorption yields. As a result, molecules desorbed from the thick sample stay longer on the foil band after laser shining, so they were transferred more thermal energy from the foil, thus they have a higher translational temperature. Figure 6.4 (b) shows the time of maximum parent ion yields and dominant fragment ion yields when probing at different distances from the foil band for the thin sample. It shows that the velocity of fragments is faster than the parent molecules. The most probable forward velocities of parent molecules at 165 u and dominant fragments at 74 u are around 254 m/s and 284 m/s, respectively. The mass of the parent molecule is 165 u, which is more than two times heavier than the dominant fragment at 74 u. If kinetic energies of parent molecules and fragments are the same, the most probable froward velocity of fragments should be $\sqrt{165/74} \approx 1.49$ times faster than the parent molecule. But the experimental result shows the most probable forward velocity of dominant fragment at 74 u is $284/254 \approx 1.12$ times faster than the parent molecule. It means that the fragmentation is mainly caused after the desorption instead of during desorption.

As for our experimental parameters (pulsed 355 nm desorption laser, 300∼600 nm/cm^2 surface coverage by aerosol spraying method, etc.), we assigned the LIAD process with

surface stress induced desorption instead of shock-off mechanism based on our experimental results [113]. When the desorption laser irradiates the back of the 10 µm tantalum foil, a quick thermal temperature rises and propagates to the front side (shown in Figure 6.2 (b)). Due to the temperature gradient and thermal expansion coefficient difference between foil and deposited sample, surface stress will be induced between them. When the thermally induced stress exceeds a critical value, the sample starts to fracture and be desorbed into vacuum. The stored stress energy in samples will be released as kinetic energy and contribute to the overall translational velocity. The translational temperature will be dependent on the thermal transport between foil and sample. Due to the foil temperature increasing with the desorption laser intensity, the plume translational temperature raises as a function of desorption laser intensity. The internal stress energy in sample is not dependent on desorption laser intensity and thus invariable with the desorption laser intensity. But different sample thickness has different internal stress energy, thus the translational forward velocity is different for different sample thickness.

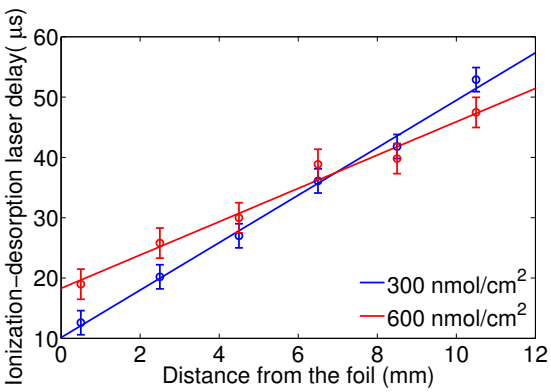

(a) The most probable translational velocity of plumes desorbed from different sample thickness layer.

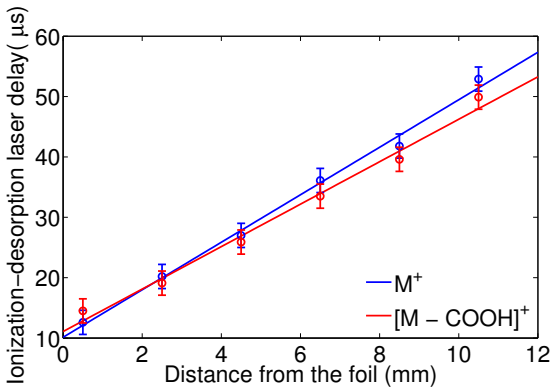

(b) The most probable translational velocity of parent molecules and dominant fragments from plumes desorbed from the thin sample layer.

Figure 6.4: Compare the most probable translational velocity of desorbed plumes from two different thickness layers.

6.4 Conclusion

We evaluated effects of sample layer thickness on laser-induced acoustic desorption process by characterizing phenylalanine plumes desorbed from samples with different thickness for their temporal profile, translational forward velocity, translational temperature and fragmentation. We found that the forward velocity and translational temperature for plumes desorbed from thick sample are higher than the thin sample. These results indicate

that the laser-induced surface stress for thick sample is higher than thin sample, thus the forward velocity of desorbed plume from thick sample is higher than thin sample. As the desorption process for thick sample is slower and lasts longer than thin sample, more thermal energy would be transferred to molecules in the plume, thus the translational temperature for thick sample is higher. The delay (around 20 µs) between maximum thermal temperature and parent molecule yields supports the desorption is caused by surface stress between sample layer and foil band, instead of shock-wave. The different forward velocity between parent molecules and dominant fragments indicates that the desorption will cause fragmentation during desorption for phenylalanine. But the velocity difference is much smaller than expected if they have same kinetic energy, it means that the fragmentation mainly happens after the desorption instead of during desorption.

7 Conclusion and Outlook

7.1 Conclusion

In this thesis, a laser-induced acoustic desorption molecular source for bringing thermally labile or non-volatile biomolecules into gas-phase, was developed and carefully characterized. The apparatus, designed for use at central facilities, such as free-electron lasers, allows for prolonged measurement times through automatic sample replenishment, whilst keeping the interaction point fixed. This is realized through the use of a long metal tape as the LIAD substrate, which is constantly forwarded – akin to an old-fashioned cassette tape – to provide fresh sample. A dedicated sample preparation method was utilized to prepare reproducible uniform sample layers on the 1 m long, 10 mm width and 10 µm thick foil band, and ensured stable reproducible desorption signals. Before applying the molecular source to central facilities, it was characterized with table-top Ti:Sapphire femtosecond laser through strong-field ionization. The ionization signals were then detected by a TOF mass spectrometer.

The experimental results confirm that laser-induced acoustic desorption can be used to transfer large neutral biomolecules into gas phase. Coupled with a post strong-field ionization technique and time-of-flight mass spectrometer, number density, spatial extend, temporal distribution, translational temperature, and forward velocity were studied for phenylalanine, adenine, glycine plumes respectively. Their fragmentation behaviors as a function of desorption laser intensity, ionization-desorption laser delay, free-flying distance were investigated, respectively. Phenylalanine, adenine and glycine plumes with number densities higher than 2×10^8 cm^{-3}, 2×10^9 cm^{-3}, and 8.5×10^8 cm^{-3} were prepared respectively. These numbers were derived from parent molecule ion yields and did not account for the fragmentations, thus they should be considered as the lower limit of the plume number density.

Figure 7.1 shows the plume longitude and transverse profiles at different desorption-ionization laser temporal delays. It illustrates how the plume propagates in the vacuum

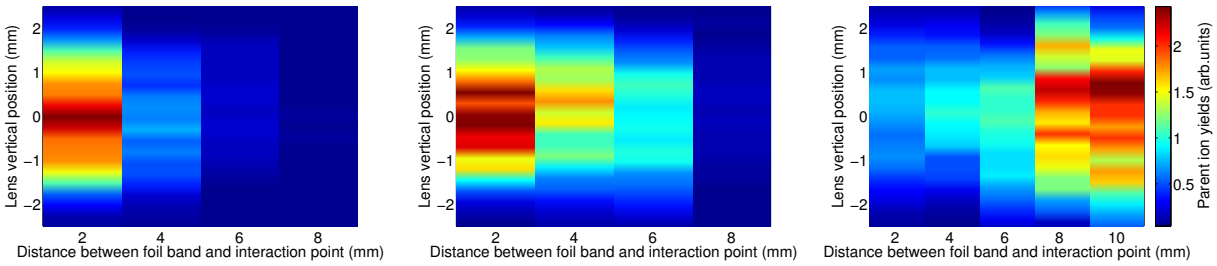

Figure 7.1: Spatial profiles of the desorbed phenylalanine plume at different desorption - ionization laser delay time. The desorption-ionization laser delay time of left image is at 20 µs, middle one is at 40 µs, right one is at 80 µs, respectively.

at different delay time. We can clearly see that the plume propagates forward in longitude z direction and expands in transverse y direction. But we need to notice here that the transverse direction might be modulated by the acceptance of the TOF electrode, which is shown in Figure 4.3. With plume temporal profiles detected at different distance from the foil, the velocity and translational temperature of the plume were derived and discussed in chapter 4.

In order to understand the desorption mechanism, we compared the plume properties of thermally stable adenine molecules and thermally labile glycine molecules. The adenine plume features no further fragmentation caused by desorption but glycine plume does. We derived the plume forward velocity and translational temperature for adenine and glycine. The forward kinetic energy of adenine and glycine is around 90 meV and 45 meV respectively, which is in the range of the surface stress energy between tantalum foil substrate and sample layer [35, 111]. The forward kinetic energy also corresponds to the physical adsorption energy of samples on the tantalum foil. In a very qualitative picture it is easy to rationalize how adenine with its highly delocalized π-system has a stronger interaction with a metal surface than glycine, with phenylalanine somewhere between the two. While translational velocity of both adenine and glycine is invariant for different desorption laser intensities, the translational temperature of glycine plume increases significantly but adenine plume does not. It indicates that the desorption process has an influence on thermally labile molecules and would induce some fragments.

In order to understand the influence of deposited sample thickness on desorption process, We evaluated phenylalanine plumes desorbed from samples with different layer thickness regarding their temporal profile, translational forward velocity, translational temperature and fragmentation. We found that the forward velocity and translational temperature for the plume desorbed from thick sample are higher than the thin sample. The fragment-to-parent ratio peak was around 20 µs earlier than the parent molecule

ion peak. These results demonstrate that the induced surface stress for thick sample is higher thus higher kinetic energy for the desorbed plume than the thin sample. As the maximum desorption for thick sample happens later than the thin sample, consequently it would undergo a longer time for thermal transport and thus a higher translational temperature than the thin sample. The long delay (20 µs) between maximum thermal temperature and parent molecule yields also supports that the desorption is caused by surface stress between substrate and sample, as it rules out the shock wave model, which will result instant desorption instead of a long delay after the desorption laser pulse. The different forward velocity between parent molecules and dominant fragments indicates that the desorption causes fragmentation during desorption for phenylalanine. But the velocity difference is much smaller than expected if they have same kinetic energy, which shows that the fragmentation is mostly coming from the post ionization laser instead of desorption laser.

The physical adsorbed molecule binding energy is around 50 $\sim$ 500 meV [125]. The kinetic energy for phenylalanine at 237 m/s is 48 meV. The phenylalanine crystal binding energy is around 500 meV $\sim$ 1 eV. Surface stress energy is around 100 meV when the temperature difference is 400 K. These observations are consistent with a desorption model based on surface stress between the foil band and islands of deposited molecules [35]. As kinetic energy of the desorbed plume ranges around 45 $\sim$ 100 meV, which is in the range of surface stress energy. We also found that the stress energy is dependent on the sample layer thickness due to their different thermal mechanic properties.

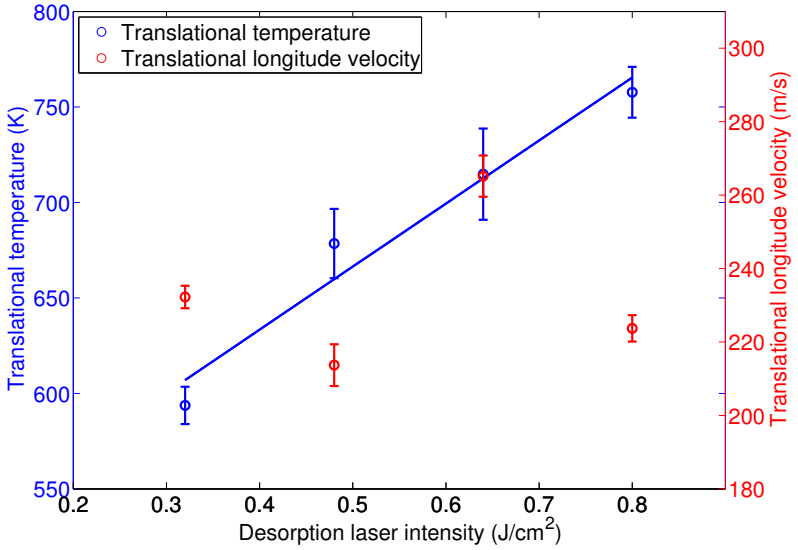

Figure 7.2: Phenylalanine plume translational forward velocity and translational temperature as a function of desorption laser intensity derived from the temporal profile measurements at different longitude distance. See subsection 4.3.2 for details.

Figure 7.2 shows that the derived translational temperature for phenylalanine plume at different desorption laser intensities. It shows a nearly linear increase with desorption laser intensity, which is confirmed by the thermal transient simulation results in subsection A.1.6. The simulation results demonstrate that surface temperature of the foil band increases linearly with the desorption laser intensity. Due to the lock of thermal equilibrium and deformation of sample rystals by the thermal and mechanical stress, the plume translational temperature was the confluence of crystal binding energy and foil surface temperature. However the translational longitude velocity is invariant with the desorption laser intensity, which shows that the desorption happens when the thermal and acoustic induced surface stress is high enough to overcome the physical adsorbed molecule binding energy.

7.2 Outlook

We have demonstrated to bring phenylalanine, adenine and glycine into gas-phase with LIAD as the volatilization method. The developed setup can be extended to bring large biomolecules, i.e. peptides, DNA strands, etc. into gas-phase. Coupled with a cryogenic buffer-gas cell, these large molecules can be cooled down to cryogenic temperature [112]. These cold large molecules allow for subsequent experiments, which are already in use for small molecules. This includes, for instance, state selection experiments [8], laser alignment and orientation experiments [13–15, 54], diffraction based analysis of structures and dynamics [4, 119, 126]. This will pave the way for the observation of ultrafast dynamics in large molecules [127] and ultimately chemical reactions. Further developments of the current setup and potential applications of the developed LIAD source will be briefly discussed in this section.

7.2.1 Couple with Cooling Techniques

As discussed in chapter 4 and chapter 5, translational temperature of prepared gas-phase molecules is higher than room temperature and increases with the desorption laser intensity. It means doses of vibrational and rotational states are populated, so these prepared molecules need to be cooled down to conduct certain experiments i.e. species separation or laser alignment experiments. The LIAD desorbed molecules can be cooled down by cryogenic buffer gas cooling [112, 128–130] or supersonic jet expansion [67, 131, 132]. Cryogenic buffer gas cooling is an efficient method to cool molecules down to cryogenic temperature due to the collisions between cold buffer-gas (i.e. helium) atoms

and sample molecules. Figure 7.3 shows the schematic of cryogenic buffer gas cooling cell, which is under development in our lab [130]. We can couple the LIAD sample source with buffer-gas cell by replacing one wall of the cell with the foil plate. The side with sample deposited on faces inside the cell. Once the sample gets desorbed, molecules will fly into the cell and collide with cold helium atoms. Translational and internal temperatures of sample molecules would be cooled down. As is known from Figure 4.3, the desorbed plume expands during free-flying. With proper design, the buffer-gas flow can be used to compress the transverse expansion of prepared plume to increase the molecule number density.

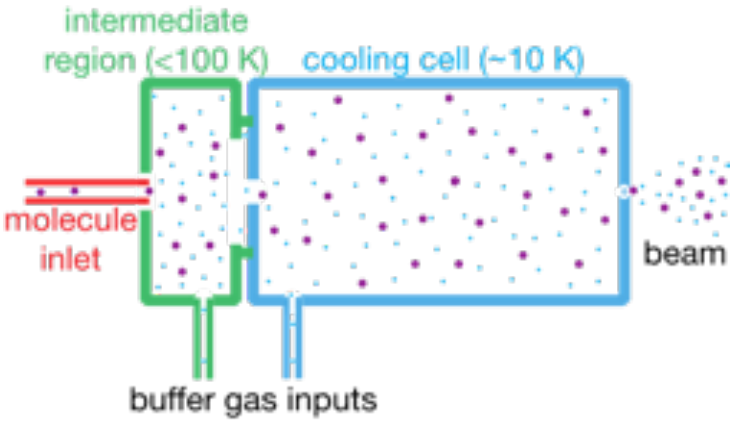

Figure 7.3: Schematic of cryogenic buffer gas cooling cell [130].

We can also couple the molecular source with supersonic expansion cooling as has been done for laser desorption source [67, 68]. The molecular beam from buffer-gas cooling is much slower than the supersonic expansion beam [112,130,133], which might be beneficial for matter-wave experiments [117, 118] and state selection experiments.

7.2.2 Structure Selection

Biomolecules usually have different conformers, whose dipole moments are different. When they fly through the inhomogeneous electric fields, the different conformers would be separated due to the stark effect. The electric force $\boldsymbol{F}$, molecule experienced is described as below,

$$\boldsymbol{F} = \mu_{\text{eff}}(\epsilon) \cdot \nabla\epsilon \tag{7.1}$$

where $\nabla\epsilon$ is the gradient of the electric field, $\mu_{\text{eff}}(\epsilon)$ is the effective dipole moment of certain molecular state at certain electric field. It is derived as below,

$$\mu_{\text{eff}}(\epsilon) = -\partial W(\epsilon)/\partial\epsilon \tag{7.2}$$

where $W(\epsilon)$ is the energy of certain molecular state at certain electric field. The energy $W(\epsilon)$ can be derived from the Schördinger equation

$$W(\epsilon)\Psi = H(\epsilon)\Psi \tag{7.3}$$

where Ψ is the molecular wavefunction, $H(\epsilon)$ is the molecular hamiltonian under electric field. It is described as below,

$$H_{\mathrm{rot},\epsilon} = H_{\mathrm{rot}} + H_{\mathrm{Stark}} \tag{7.4}$$

where H_{rot} is a simplified molecular hamiltonian without external electric fields, H_{Stark} is hamiltonian describing the stark effect [134]. It is given by

$$H_{\mathrm{Stark}} = -\boldsymbol{\mu} \cdot \boldsymbol{\epsilon} \tag{7.5}$$

where $\boldsymbol{\mu}$ is the permanent dipole moment and $\boldsymbol{\epsilon}$ is the electric field vector in the laboratory frame.

Figure 7.4 shows the separation of different conformers when flying through the deflector. The inhomogeneous electric fields between the deflector electrodes is showing in Figure 1.1.

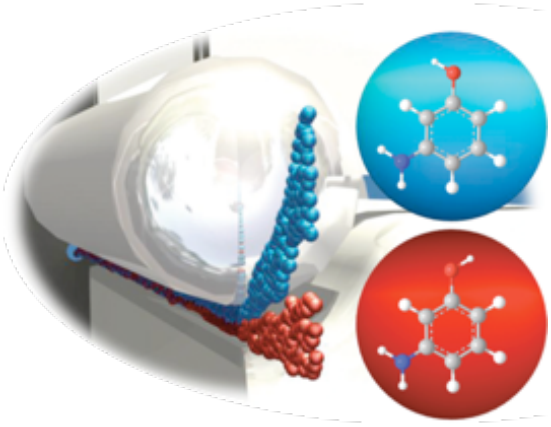

Figure 7.4: Schematic drawing of separation of 3-Aminophenol conformers [8–10]

Not only for conformers, different cluster stoichiometries or even different quantum (i.e. rotational) states can be separated due to their different effective dipole moments [8, 9, 11, 95–98]. As a result, a pure molecular beam with the same conformer, cluster size, or quantum state can be prepared.

7.2.3 Alignment and Orientation

Align and orient gas-phase molecules in the molecular frame is helpful to improve the signal-to-noise ratio on the detector when imaging them with X-ray or electron pulses [2–4, 135]. Figure 7.5 shows a schematic diagram of isotropically oriented (left), aligned (middle), and oriented iodobenzene molecules (right). For isolated molecules in laser field, the hamiltonian H_{align}, which describes alignment, can be written as below:

$$H_{align} = H_{\mathrm{rot}} + V_{\alpha} \tag{7.6}$$

where V_{α} is the induced potential by the laser field. For an asymmetric top molecule the induced potential by a linear polarized laser can be described by

$$V_{\alpha} = -\frac{(E_0\epsilon(t))^2}{4}(\sin^2\theta(\alpha_{xx}\cos^2\chi + \alpha_{yy}\sin^2\chi) + \alpha_{zz}\cos^2\theta) \tag{7.7}$$

where E_0 is the electric field strength and $\epsilon(t)$ is the laser pulse envelope. α_{xx}, α_{yy}, and α_{zz} are the polarizability tensor components with respect to the molecular frame, θ is polar Euler angle between the laser field polarization and the molecular axis, and χ is the azimuthal Euler angle about the molecules z-axis. Depending on the rotation period τ_{Rot} of molecules and the rising and falling time τ_{Laser} of the laser pulse intensity, the laser alignment regime can be divided into three regimes [9, 11, 95], i.e, adiabatic regime for $\tau_{\mathrm{Laser}} \gg \tau_{\mathrm{Rot}}$, intermediate regime for $\tau_{\mathrm{Laser}} \approx \tau_{\mathrm{Rot}}$ and non-adiabatic regime for $\tau_{\mathrm{Laser}} \ll \tau_{\mathrm{Rot}}$. After the alignment, molecules can point up or down. By adding a strong

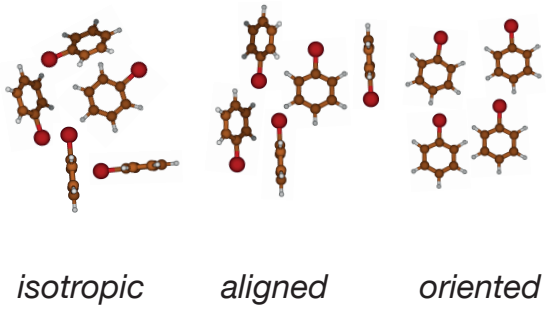

Figure 7.5: Schematic illustration of alignment and orientation of iodobenzene molecules [15]

external electric DC field, it will break down the up-down symmetry of the dipole moment vector of molecules and lead to orientation in one direction [136–138]. The hamiltonian is described as below,

$$H = H_{\mathrm{rot}} + V_{\alpha} + V_{\mu} \tag{7.8}$$

where V_μ is the interaction potential between electric field ϵ and dipole moment of the molecule.

$$V_\mu = -\mu \cdot \epsilon \cdot \cos\theta \tag{7.9}$$

where θ is the angle between the electric field and the molecular axis. As a result the selected pure molecule sample can be fixed in one direction due to the presence of laser field and electric DC field. The alignment and orientation degree θ can be evaluated by the ion velocity map imaging spectrometer [139–142].

7.2.4 X-ray and Electron Imaging

The LIAD setup developed in the dissertation can prepare gas-phase biomolecules with a number density higher than 10^9 cm^{-3} without seeding gas in the interaction region. It has been demonstrated that the LIAD source can be coupled with attosecond laser pulses to study ultrafast electron dynamics of amino acids [143]. We can utilize the molecular source to do ultrafast spectroscopy experiments, diffractive imaging or coulomb explosion imaging experiments. Or we couple it with cryogenic buffer-gas cell firstly to cool the molecules down and then implement our conventional gas-phase molecule control experiments (i.e. structure selection, laser alignment and mixed field orientation). Then the controlled state-selected pure samples are delivered to the interaction points for X-ray or electron imaging experiments. For the former case we have high number density of samples without carrier gas but isotropic oriented in the interaction region. For the later case we have controlled, identical and oriented molecules but less number density mixed with carrier gas in the interaction region. For both cases, LIAD provides a promising gas-phase biomolecule sample source for imaging and spectroscopy experiments.

Bibliography

[1] K. Yamanouchi, W. T. Hill III, and G. G. Paulus, Progress in Ultrafast Intense Laser Science XIII. Springer, Dec. 2017.

[2] S. Stern, Controlled Molecules for X-ray Diffraction Experiments at Free-Electron Lasers. Dissertation, Universität Hamburg, Hamburg, Germany, 2013.

[3] J. Küpper, S. Stern, L. Holmegaard, F. Filsinger, A. Rouzée, A. Rudenko, P. Johnsson, A. V. Martin, M. Adolph, A. Aquila, S. Bajt, A. Barty, C. Bostedt, J. Bozek, C. Caleman, R. Coffee, N. Coppola, T. Delmas, S. Epp, B. Erk, L. Foucar, T. Gorkhover, L. Gumprecht, A. Hartmann, R. Hartmann, G. Hauser, P. Holl, A. Hömke, N. Kimmel, F. Krasniqi, K.-U. Kühnel, J. Maurer, M. Messerschmidt, R. Moshammer, C. Reich, B. Rudek, R. Santra, I. Schlichting, C. Schmidt, S. Schorb, J. Schulz, H. Soltau, J. C. H. Spence, D. Starodub, L. Strüder, J. Thøgersen, M. J. J. Vrakking, G. Weidenspointner, T. A. White, C. Wunderer, G. Meijer, J. Ullrich, H. Stapelfeldt, D. Rolles, and H. N. Chapman, "X-ray diffraction from isolated and strongly aligned gas-phase molecules with a free-electron laser," Phys. Rev. Lett., vol. 112, p. 083002, 2014.

[4] S. Stern, L. Holmegaard, F. Filsinger, A. Rouzée, A. Rudenko, P. Johnsson, A. V. Martin, A. Barty, C. Bostedt, J. D. Bozek, R. N. Coffee, S. Epp, B. Erk, L. Foucar, R. Hartmann, N. Kimmel, K.-U. Kühnel, J. Maurer, M. Messerschmidt, B. Rudek, D. G. Starodub, J. Thøgersen, G. Weidenspointner, T. A. White, H. Stapelfeldt, D. Rolles, H. N. Chapman, and J. Küpper, "Toward atomic resolution diffractive imaging of isolated molecules with x-ray free-electron lasers," Faraday Disc., vol. 171, p. 393, 2014.

[5] M. M. Seibert, T. Ekeberg, F. R. N. C. Maia, M. Svenda, J. Andreasson, O. Jönsson, D. Odić, B. Iwan, A. Rocker, D. Westphal, M. Hantke, D. P. Deponte, A. Barty, J. Schulz, L. Gumprecht, N. Coppola, A. Aquila, M. Liang, T. A. White, A. Martin, C. Caleman, S. Stern, C. Abergel, V. Seltzer, J.-M. Claverie, C. Bostedt, J. D.

Bozek, S. Boutet, A. A. Miahnahri, M. Messerschmidt, J. Krzywinski, G. Williams, K. O. Hodgson, M. J. Bogan, C. Y. Hampton, R. G. Sierra, D. Starodub, I. Andersson, S. Bajt, M. Barthelmess, J. C. H. Spence, P. Fromme, U. Weierstall, R. Kirian, M. Hunter, R. B. Doak, S. Marchesini, S. P. Hau-Riege, M. Frank, R. L. Shoeman, L. Lomb, S. W. Epp, R. Hartmann, D. Rolles, A. Rudenko, C. Schmidt, L. Foucar, N. Kimmel, P. Holl, B. Rudek, B. Erk, A. Hömke, C. Reich, D. Pietschner, G. Weidenspointner, L. Strüder, G. Hauser, H. Gorke, J. Ullrich, I. Schlichting, S. Herrmann, G. Schaller, F. Schopper, H. Soltau, K.-U. Kühnel, R. Andritschke, C.-D. Schröter, F. Krasniqi, M. Bott, S. Schorb, D. Rupp, M. Adolph, T. Gorkhover, H. Hirsemann, G. Potdevin, H. Graafsma, B. Nilsson, H. N. Chapman, and J. Hajdu, "Single mimivirus particles intercepted and imaged with an X-ray laser," Nature, vol. 470, no. 7332, p. 78, 2011.

[6] S. Boutet and G. Williams, "The coherent x-ray imaging (cxi) instrument at the linac coherent light source (lcls)," New J. Phys., vol. 12, p. 035024, 2010.

[7] R. Neutze, R. Wouts, D. van der Spoel, E. Weckert, and J. Hajdu, "Potential for biomolecular imaging with femtosecond x-ray pulses," Nature, vol. 406, pp. 752–757, Aug. 2000.

[8] Y.-P. Chang, D. A. Horke, S. Trippel, and J. KÃ¼pper, "Spatially-controlled complex molecules and their applications," Int. Rev. Phys. Chem., vol. 34, pp. 557–590, 2015.

[9] F. Filsinger, J. Küpper, G. Meijer, J. L. Hansen, J. Maurer, J. H. Nielsen, L. Holmegaard, and H. Stapelfeldt, "Pure samples of individual conformers: the separation of stereo-isomers of complex molecules using electric fields," Angew. Chem. Int. Ed., vol. 48, pp. 6900–6902, 2009.

[10] T. Kierspel, D. A. Horke, Y.-P. Chang, and J. Küpper, "Spatially separated polar samples of the cis and trans conformers of 3-fluorophenol," Chem. Phys. Lett., vol. 591, pp. 130–132, 2014.

[11] S. Trippel, Y.-P. Chang, S. Stern, T. Mullins, L. Holmegaard, and J. Küpper, "Spatial separation of state- and size-selected neutral clusters," Phys. Rev. A, vol. 86, p. 033202, Sept. 2012.

[12] D. A. Horke, S. Trippel, Y.-P. Chang, S. Stern, T. Mullins, T. Kierspel, and J. Küpper, "Spatial separation of molecular conformers and clusters," J. Vis. Exp., vol. (83), p. e51137, 2014.

[13] L. Holmegaard, J. H. Nielsen, I. Nevo, H. Stapelfeldt, F. Filsinger, J. Küpper, and G. Meijer, "Laser-induced alignment and orientation of quantum-state-selected large molecules," Phys. Rev. Lett., vol. 102, p. 023001, 2009.

[14] F. Filsinger, J. Küpper, G. Meijer, L. Holmegaard, J. H. Nielsen, I. Nevo, J. L. Hansen, and H. Stapelfeldt, "Quantum-state selection, alignment, and orientation of large molecules using static electric and laser fields," J. Chem. Phys., vol. 131, p. 064309, 2009.

[15] S. Trippel, T. Mullins, N. L. M. Müller, J. S. Kienitz, K. Długołęcki, and J. Küpper, "Strongly aligned and oriented molecular samples at a kHz repetition rate," Mol. Phys., vol. 111, p. 1738, 2013.

[16] B. Lindner and U. Seydel, "Laser desorption mass spectrometry of nonvolatiles under shock wave conditions," Anal. Chem., vol. 57, pp. 895–899, 1985.

[17] B. Lindner, "On the desorption of electrosprayed organic compounds from supporting metal foils by laser induced pressure waves," Int. J. Mass Spectrom. Ion Processes, vol. 103, no. 2-3, pp. 203–218, 1991.

[18] V. V. Golovlev, S. L. Allman, W. R. Garrett, and C. H. Chen, "Laser-induced acoustic desorption of electrons and ions," Appl. Phys. Lett., vol. 71, pp. 852–854, Aug. 1997.

[19] V. V. Golovlev, S. L. Allman, W. R. Garrett, N. I. Taranenko, and C. H. Chen, "Laser-induced acoustic desorption," Int. J. Mass Spectrom. Ion Processes, vol. 169–170, pp. 69–78, Dec. 1997.

[20] W.-P. Peng, Y.-C. Yang, M.-W. Kang, Y.-K. Tzeng, Z. Nie, H.-C. Chang, W. Chang, and C.-H. Chen, "Laser-induced acoustic desorption mass spectrometry of single bioparticles," Angew. Chem. Int. Ed., vol. 45, pp. 1423–1426, 2006.

[21] L. Nyadong, J. P. Quinn, C. S. Hsu, C. L. Hendrickson, R. P. Rodgers, and A. G. Marshall, "Atmospheric pressure laser-induced acoustic desorption chemical ionization mass spectrometry for analysis of saturated hydrocarbons," Anal. Chem., vol. 84, pp. 7131–7137, Aug. 2012.

[22] J. Pérez, L. E. Ramírez-Arizmendi, C. J. Petzold, L. P. Guler, E. D. Nelson, and H. I. Kenttämaa, "Laser-induced acoustic desorption/chemical ionization in fourier-transform ion cyclotron resonance mass spectrometry," Int. J. Mass Spectrom., vol. 198, pp. 173–188, May 2000.

[23] R. C. Shea, C. J. Petzold, J. L. Campbell, S. Li, D. J. Aaserud, and H. I. Kenttämaa, "Characterization of laser-induced acoustic desorption coupled with a fourier transform ion cyclotron resonance mass spectrometer," Anal. Chem., vol. 78, no. 17, pp. 6133–6139, 2006.

[24] R. C. Shea, S. C. Habicht, W. E. Vaughn, and H. I. Kenttämaa, "Design and characterization of a high-power laser-induced acoustic desorption probe coupled with a fourier transform ion cyclotron resonance mass spectrometer," Anal. Chem., vol. 79, pp. 2688–2694, Feb. 2007.

[25] S. C. Habicht, L. M. Amundson, P. Duan, N. R. Vinueza, and H. I. Kenttämaa, "Laser-induced acoustic desorption coupled with a linear quadrupole ion trap mass spectrometer," Anal. Chem., vol. 82, pp. 608–614, Jan. 2010.

[26] J. Gao, D. J. Borton, B. C. Owen, Z. Jin, M. Hurt, L. M. Amundson, J. T. Madden, K. Qian, and H. I. Kenttämaa, "Laser-Induced Acoustic Desorption/Atmospheric Pressure Chemical Ionization Mass Spectrometry," J. Am. Soc. Mass. Spectrom., vol. 22, pp. 531–538, Jan. 2011.

[27] N. Zhang, K. Zhu, C. Xiong, Y. Jiang, H.-C. Chang, and Z. Nie, "Mass measurement of single intact nanoparticles in a cylindrical ion trap," Anal. Chem., vol. 88, no. 11, pp. 5958–5962, 2016.

[28] C. R. Calvert, L. Belshaw, M. J. Duffy, O. Kelly, R. B. King, A. G. Smyth, T. J. Kelly, J. T. Costello, D. J. Timson, W. A. Bryan, T. Kierspel, P. Rice, I. C. E. Turcu, C. M. Cacho, E. Springate, I. D. Williams, and J. B. Greenwood, "LIAD-fs scheme for studies of ultrafast laser interactions with gas phase biomolecules," Phys. Chem. Chem. Phys., vol. 14, no. 18, pp. 6289–6297, 2012.

[29] L. Belshaw, F. Calegari, M. J. Duffy, A. Trabattoni, L. Poletto, M. Nisoli, and J. B. Greenwood, "Observation of ultrafast charge migration in an amino acid," J. Phys. Chem. Lett., vol. 3, pp. 3751–3754, Dec. 2012.

[30] F. Calegari, D. Ayuso, A. Trabattoni, L. Belshaw, S. De Camillis, S. Anumula, F. Frassetto, L. Poletto, A. Palacios, P. Decleva, J. B. Greenwood, F. Martín, and M. Nisoli, "Ultrafast electron dynamics in phenylalanine initiated by attosecond pulses," Science, vol. 346, pp. 336–339, Oct. 2014.

[31] M. G. H. Boogaarts and G. Meijer, "Measurement of the beam intensity in a laser-desorption jet-cooling mass-spectrometer," J. Chem. Phys., vol. 103, pp. 5269–5274, 1995.

[32] I. Compagnon, R. Antoine, D. Rayane, M. Broyer, and P. Dugourd, "Permanent electric dipole of gas-phase p-amino benzoic acid," J. Phys. Chem. A, vol. 107, pp. 3036–3039, 2003.

[33] J. W. Elam and D. H. Levy, "Ultraviolet laser desorption of indole," J. Chem. Phys., vol. 106, pp. 10368–10378, 1997.

[34] K. Rogers, J. Milnes, and J. Gormally, "The laser desorption laser ionization mass-spectra of some indole-derivatives and alkaloids," Int. J. Mass Spectrom. Ion Processes, vol. 115, pp. 219–233, 1992.

[35] A. V. Zinovev, I. V. Veryovkin, J. F. Moore, and M. J. Pellin, "Laser-driven acoustic desorption of organic molecules from back-irradiated solid foils," Anal. Chem., vol. 79, pp. 8232–8241, Oct. 2007.

[36] D. P. DePonte, U. Weierstall, K. Schmidt, J. Warner, D. Starodub, J. C. H. Spence, and R. B. Doak, "Gas dynamic virtual nozzle for generation of microscopic droplet streams," J. Phys. D, vol. 41, no. 19, p. 195505, 2008.

[37] K. R. Beyerlein, L. Adriano, M. Heymann, R. Kirian, J. Knoska, F. Wilde, H. N. Chapman, and S. Bajt, "Ceramic micro-injection molded nozzles for serial femtosecond crystallography sample delivery," Rev. Sci. Instrum., vol. 86, p. 125104, Dec. 2015.

[38] W. Wiley and I. Mclaren, "Time-of-flight mass spectrometer with improved resolution," Rev. Sci. Instrum., vol. 26, no. 12, pp. 1150–1157, 1955.

[39] P. Emma, R. Akre, J. Arthur, R. Bionta, C. Bostedt, J. Bozek, A. Brachmann, P. Bucksbaum, R. Coffee, F. J. Decker, Y. Ding, D. Dowell, S. Edstrom, A. Fisher, J. Frisch, S. Gilevich, J. Hastings, G. Hays, P. Hering, Z. Huang, R. Iverson, H. Loos, M. Messerschmidt, A. Miahnahri, S. Moeller, H. D. Nuhn, G. Pile, D. Ratner, J. Rzepiela, D. Schultz, T. Smith, P. Stefan, H. Tompkins, J. Turner, J. Welch, W. White, J. Wu, G. Yocky, and J. Galayda, "First lasing and operation of an angstrom-wavelength free-electron laser," Nat. Photon., vol. 4, pp. 641–647, Jul 2010.

[40] K. Ayyer, G. Geloni, V. Kocharyan, E. Saldin, S. Serkez, O. Yefanov, and I. Zagorodnov, "Perspectives for imaging single protein molecules with the present design of the european xfel," Struct. Dyn., vol. 2, p. 041702, jul 2015.

[41] A. Barty, "Time-resolved imaging using x-ray free electron lasers," J. Phys. B, vol. 43, p. 194014, Oct. 2010.

[42] M. Bargheer, N. Zhavoronkov, Y. Gritsai, J. C. Woo, D. S. Kim, M. Woerner, and T. Elsaesser, "Coherent atomic motions in a nanostructure studied by femtosecond x-ray diffraction," Science, vol. 306, no. 5702, pp. 1771–1773, 2004.

[43] R. G. J. Fraser, Molecular Beams. Methuen's Monographs on Physical Subjects, London, GB: Methuen & Co., 1937.

[44] M. Staniforth and V. G. Stavros, "Recent advances in experimental techniques to probe fast excited-state dynamics in biological molecules in the gas phase: dynamics in nucleotides, amino acids and beyond.," Proc. Royal Soc. London A, vol. 469, pp. 20130458–20130458, Nov. 2013.

[45] J. W. Elam and D. H. Levy, "Laser ablation of trp-gly," Journal Of Physical Chemistry B, vol. 102, pp. 8113–8120, 1998.

[46] A. Kantrowitz and J. Grey, "A high intensity source for the molecular beam. part i. theoretical," Rev. Sci. Instrum., vol. 22, no. 5, pp. 328–332, 1951.

[47] G. B. Kistiakowsky and W. P. Slichter, "A high intensity source for the molecular beam. part ii. experimental," Rev. Sci. Instrum., vol. 22, no. 5, pp. 333–337, 1951.

[48] D. Touboul, F. Gaie-Levrel, G. A. Garcia, L. Nahon, L. Poisson, M. Schwell, and M. Hochlaf, "Vuv photoionization of gas phase adenine and cytosine: A comparison between oven and aerosol vaporization," J. Chem. Phys., vol. 138, pp. 094203–094203, Mar. 2013.

[49] K. R. Wilson, M. Jimenez-Cruz, C. Nicolas, L. Belau, S. R. Leone, and M. Ahmed, "Thermal vaporization of biological nanoparticles: fragment-free vacuum ultraviolet photoionization mass spectra of tryptophan, phenylalanine−glycine−glycine, and β-carotene," J. Phys. Chem. A, vol. 110, pp. 2106–2113, Feb. 2006.

[50] U. Even, "Pulsed supersonic beams from high pressure source: Simulation results and experimental measurements," Adv. Chem., vol. 2014, p. 636042, 2014.

[51] U. Even, J. Jortner, D. Noy, N. Lavie, and N. Cossart-Magos, "Cooling of large molecules below 1 K and He clusters formation," J. Chem. Phys., vol. 112, pp. 8068–8071, 2000.

[52] G. Scoles, ed., Atomic and molecular beam methods, vol. 2. New York, NY, USA: Oxford University Press, 1992.

[53] J. B. Fenn, "Research in retrospect: Some biograffiti of a journeyman chemist," Annu. Rev. Phys. Chem., vol. 47, pp. 1–41, 1996.

[54] H. Stapelfeldt and T. Seideman, "Colloquium: Aligning molecules with strong laser pulses," Rev. Mod. Phys., vol. 75, no. 2, pp. 543–557, 2003.

[55] B. Friedrich and D. Herschbach, "Alignment and trapping of molecules in intense laser fields," Phys. Rev. Lett., vol. 74, pp. 4623–4626, June 1995.

[56] B. Friedrich and D. Herschbach, "Polarization of molecules induced by intense nonresonant laser fields," J. Phys. Chem., vol. 99, p. 15686, 1995.

[57] A. Vertes, "Laser desorption of large molecules: Mechanisms and models," in Methods and Mechanisms for Producing Ions from Large Molecules, pp. 275–286, Boston, MA: Springer, Boston, MA, 1991.

[58] A. Vertes and R. D. LEVINE, "Sublimation versus fragmentation in matrix-assisted laser desorption," Chem. Phys. Lett., vol. 171, no. 4, pp. 284–290, 1990.

[59] L. G. Wright, R. G. Cooks, and K. V. Wood, "Matrix enhanced laser desorption in mass spectrometry and tandem mass spectrometry," Biomedical Mass Spectrometry, vol. 12, p. 159, 1985.

[60] K. Dreisewerd, "The desorption process in maldi," Chem. Rev., vol. 103, p. 395, 2003.

[61] M. Karas and F. Hillenkamp, "Laser desorption ionization of proteins with molecular masses exceeding 10000 daltons," Anal. Chem., vol. 60, pp. 2299–2301, 1988.

[62] L. Li and D. M. Lubman, "Pulsed laser desorption method for volatilizing thermally labile molecules for supersonic jet spectroscopy," Rev. Sci. Instrum., vol. 59, pp. 557–561, 1988.

[63] G. Meijer, M. S. de Vries, H. E. Hunziker, and H. R. Wendt, "Laser desorption jet-cooling of organic molecules – cooling characteristics and detection sensitivity," Appl. Phys. B, vol. 51, pp. 395–403, 1990.

[64] G. Meijer, M. S. de Vries, H. E. Hunziker, and H. R. Wendt, "Laser desorption jet-cooling spectroscopy of para-amino benzoic-acid monomer, dimer, and clusters," J. Chem. Phys., vol. 92, pp. 7625–7635, 1990.

[65] G. Meijer, M. S. de Vries, H. E. Hunziker, and H. R. Wendt, "Laser desorption jet-cooling spectroscopy of the benzoic-acid monomer," J. Phys. Chem., vol. 94, pp. 4394–4396, 1990.

[66] S.-i. Ishiuchi, K. Yamada, H. Oba, H. Wako, and M. Fujii, "Gas phase ultraviolet and infrared spectroscopy on a partial peptide of β_2-adrenoceptor SIVSF-NH_2 by a laser desorption supersonic jet technique," Phys. Chem. Chem. Phys., vol. 18, pp. 23277–23284, 2016.

[67] N. Teschmit, K. Długołęcki, D. Gusa, I. Rubinsky, D. A. Horke, and J. Küpper, "Characterizing and optimizing a laser-desorption molecular beam source," J. Chem. Phys., vol. 147, p. 144204, 2017.

[68] N. Teschmit, D. A. Horke, and J. Küpper, "Spatially separating the conformers of a dipeptide," Angew. Chem. Int. Ed., vol. 57, pp. 13775–13779, Oct. 2018.

[69] I. Bald, Low Energy Electron Induced Reactions in Gas Phase Biomolecules. Dissertation, Freien Universität Berlin, Berlin,Germany, 2007.

[70] K. C. Kulander, K. J. Schafer, and J. L. Krause, "Dynamics of short-pulse excitation, ionization and harmonic conversion," in Super-Intense Laser-Atom Physics (A. L'Huillier, B. Piraux, and K. Rzazewski, eds.), vol. 316 of Nato Science Series B: Physics, pp. 95–110, Plenum Press, New York, 1993.

[71] M. Protopapas, C. H. Keitel, and P. L. Knight, "Atomic physics with super-high intensity lasers," Rep. Prog. Phys., vol. 60, pp. 389–486, Apr. 1997.

[72] G. Mainfray and G. Manus, "Multiphoton ionization of atoms," Rep. Prog. Phys., vol. 54, pp. 1333–1372, Dec. 1991.

[73] S. Campbell, J. L. Beauchamp, M. Rempe, and D. L. Lichtenberger, "Correlations of lone pair ionization energies with proton affinities of amino-acids and related-compounds - site specificity of protonation," Int. J. Mass Spectrom. Ion Processes, vol. 117, no. 1-3, pp. 83–99, 1992.

[74] F. Gaie-Levrel, G. A. Garcia, M. Schwell, and L. Nahon, "Vuv state-selected photoionization of thermally-desorbed biomolecules by coupling an aerosol source to an imaging photoelectron/photoion coincidence spectrometer: case of the amino acids tryptophan and phenylalanine," Phys. Chem. Chem. Phys., vol. 13, no. 15, pp. 7024–7036, 2011.

[75] W. Demtröder, Laser Spectroscopy: Basic Concepts and Instrumentation. Berlin: Springer Verlag, 3 ed., 2003.

[76] S. Augst, D. D. Meyerhofer, D. Strickland, and S. L. Chin, "Laser ionization of noble gases by coulomb-barrier suppression," J. Opt. Soc. Am. B, vol. 8, pp. 858–867, Apr 1991.

[77] L. Keldysh, "Ionization in the field of a strong electromagnetic wave," J. Exp. Theor. Phys., vol. 20, no. 5, pp. 1307–1314, 1965.

[78] H. N. Chapman, A. Barty, S. Marchesini, A. Noy, S. P. Hau-Riege, C. Cui, M. R. Howells, R. Rosen, H. He, J. C. H. Spence, U. Weierstall, T. Beetz, C. Jacobsen, and D. Shapiro, "High-resolution ab initio three-dimensional x-ray diffraction microscopy," J. Opt. Soc. Am. A, vol. 23, no. 5, pp. 1179–1200, 2006.

[79] J. C. Williamson, J. M. Cao, H. Ihee, H. Frey, and A. H. Zewail, "Clocking transient chemical changes by ultrafast electron diffraction," Nature, vol. 386, no. 6621, pp. 159–162, 1997.

[80] T. Kierspel, Imaging structure and dynamics using controlled molecules. Dissertation, Universität Hamburg, Hamburg, Germany, 2016.

[81] R. Srinivasan, V. A. Lobastov, C.-Y. Ruan, and A. H. Zewail, "Ultrafast electron diffraction (ued). a new development for the 4d determination of transient molecular structures," Helv. Chim. Acta., vol. 86, no. 40, p. 1763, 2003.

[82] A. H. Zewail, "4D ultrafast electron diffraction, crystallography, and microscopy," Annu. Rev. Phys. Chem., vol. 57, pp. 65–103, 2006.

[83] B. Wolter, M. G. Pullen, A. T. Le, M. Baudisch, K. Doblhoff-Dier, A. Senftleben, M. Hemmer, C. D. Schroter, J. Ullrich, T. Pfeifer, R. Moshammer, S. Gräfe, O. Vendrell, C. D. Lin, and J. Biegert, "Ultrafast electron diffraction imaging of bond breaking in di-ionized acetylene," Science, vol. 354, pp. 308–312, oct 2016.

[84] C. J. Hensley, J. Yang, and M. Centurion, "Imaging of isolated molecules with ultrafast electron pulses," Phys. Rev. Lett., vol. 109, p. 133202, 2012.

[85] J. Yang, M. Guehr, T. Vecchione, M. S. Robinson, R. Li, N. Hartmann, X. Shen, R. Coffee, J. Corbett, A. Fry, K. Gaffney, T. Gorkhover, C. Hast, K. Jobe, I. Makasyuk, A. Reid, J. Robinson, S. Vetter, F. Wang, S. Weathersby, C. Yoneda, M. Centurion, and X. Wang, "Diffractive imaging of a rotational wavepacket in nitrogen molecules with femtosecond megaelectronvolt electron pulses," Nat. Commun., vol. 7, p. 11232, Apr. 2016.

[86] J. Yang, J. Beck, C. J. Uiterwaal, and M. Centurion, "Imaging of alignment and structural changes of carbon disulfide molecules using ultrafast electron diffraction," Nat. Commun., vol. 6, p. 8172, 2015.

[87] J. Yang, X. Zhu, T. J. A. Wolf, Z. Li, J. P. F. Nunes, R. Coffee, J. P. Cryan, M. Gühr, K. Hegazy, T. F. Heinz, K. Jobe, R. Li, X. Shen, T. Veccione, S. Weathersby, K. J. Wilkin, C. Yoneda, Q. Zheng, T. J. Martínez, M. Centurion, and X. Wang, "Imaging CF_3I conical intersection and photodissociation dynamics with ultrafast electron diffraction," Science, vol. 361, pp. 64–67, July 2018.

[88] J. Als-Nielsen and D. McMorrow, Elements of Modern X-ray Physics. Chichester, West Sussex, United Kingdom: John Wiley & Sons, 2001.

[89] R. Glauber and V. Schomaker, "The theory of electron diffraction," Phys. Rev., vol. 89, pp. 667–671, Feb 1953.

[90] I. Hargittai and M. Hargittai, Stereochemical Applications of Gas-Phase Electron Diffraction. Weinheim, Germany: VCH Verlagsgesellschaft, 1988.

[91] A. A. Ischenko and S. A. Aseyev, Time-Resolved Electron Diffraction: For Chemistry, Biology and Materials Science, vol. 184 of Advances in Imaging and Electron Physics. Amsterdam: Elsevier, 2014.

[92] A. M. Michalik, E. Y. Sherman, and J. E. Sipe, "Theory of ultrafast electron diffraction: The role of the electron bunch properties," J. Appl. Phys., vol. 104, p. 054905, 2008.

[93] J. C. H. Spence, "Electron diffraction from laser-aligned beams of large hydrated molecules," Journal of Electron Microscopy, vol. 54, no. 3, pp. 163–168, 2005.

[94] J. Yang and M. Centurion, "Gas-phase electron diffraction from laser-aligned molecules",," Struct. Chem., vol. 26, no. 5, pp. 1513–1520, 2015.

[95] F. Filsinger, U. Erlekam, G. von Helden, J. Küpper, and G. Meijer, "Selector for structural isomers of neutral molecules," Phys. Rev. Lett., vol. 100, p. 133003, 2008.

[96] J. H. Nielsen, P. Simesen, C. Z. Bisgaard, H. Stapelfeldt, F. Filsinger, B. Friedrich, G. Meijer, and J. Küpper, "Stark-selected beam of ground-state OCS molecules characterized by revivals of impulsive alignment," Phys. Chem. Chem. Phys., vol. 13, pp. 18971–18975, 2011.

[97] D. A. Horke, Y.-P. Chang, K. Długołęcki, and J. Küpper, "Separating para and ortho water," Angew. Chem. Int. Ed., vol. 53, pp. 11965–11968, 2014.

[98] S. Y. T. van de Meerakker, H. L. Bethlem, N. Vanhaecke, and G. Meijer, "Manipulation and control of molecular beams," Chem. Rev., vol. 112, pp. 4828–4878, Mar. 2012.

[99] C. Z. Bisgaard, O. J. Clarkin, G. Wu, A. M. D. Lee, O. Geßner, C. C. Hayden, and A. Stolow, "Time-resolved molecular frame dynamics of fixed-in-space CS_2 molecules," Science, vol. 323, no. 5920, pp. 1464–1468, 2009.

[100] L. Holmegaard, J. L. Hansen, L. Kalhøj, S. L. Kragh, H. Stapelfeldt, F. Filsinger, J. Küpper, G. Meijer, D. Dimitrovski, M. Abu-samha, C. P. J. Martiny, and L. B. Madsen, "Photoelectron angular distributions from strong-field ionization of oriented molecules," Nat. Phys., vol. 6, p. 428, 2010.

[101] R. Boll, D. Anielski, C. Bostedt, J. D. Bozek, L. Christensen, R. Coffee, S. De, P. Decleva, S. W. Epp, B. Erk, L. Foucar, F. Krasniqi, J. Küpper, A. Rouzée, B. Rudek, A. Rudenko, S. Schorb, H. Stapelfeldt, M. Stener, S. Stern, S. Techert, S. Trippel, M. J. J. Vrakking, J. Ullrich, and D. Rolles, "Femtosecond photoelectron diffraction on laser-aligned molecules: Towards time-resolved imaging of molecular structure," Phys. Rev. A, vol. 88, p. 061402(R), 2013.

[102] M. S. de Vries and P. Hobza, "Gas-phase spectroscopy of biomolecular building blocks," Annu. Rev. Phys. Chem., vol. 58, no. 1, pp. 585–612, 2007.

[103] A. V. Bulgakov, N. Goodfriend, O. Nerushev, N. M. Bulgakova, S. V. Starinskiy, Y. G. Shukhov, and E. E. B. Campbell, "Laser-induced transfer of nanoparticles for gas-phase analysis," J. Opt. Soc. Am. B, vol. 31, no. 11, pp. C15–C21, 2014.

[104] N. T. Goodfriend, S. V. Starinskiy, O. A. Nerushev, N. M. Bulgakova, A. V. Bulgakov, and E. E. B. Campbell, "Laser pulse duration dependence of blister formation on back-radiated Ti thin films for BB-LIFT," Appl. Phys. A, vol. 122, no. 3, p. 154, 2016.

[105] P. J. Linstrom and W. G. Mallard, eds., NIST Chemistry WebBook, NIST Standard Reference Database Number 69. Gaithersburg MD, 20899: National Institute of Standards and Technology, May 2017.

[106] L. V. Zhigilei and B. J. Garrison, "Velocity distributions of molecules ejected in laser ablation," Appl. Phys. Lett., vol. 71, no. 4, pp. 551–553, 1997.

[107] N. G. Utterback, S. P. Tang, and J. F. Friichtenicht, "Atomic and ionic beam source utilizing pulsed laser blow off," Phys. Fluids, vol. 19, no. 6, pp. 900–905, 1976.

[108] F. Calegari, D. Ayuso, A. Trabattoni, L. Belshaw, S. De Camillis, F. Frassetto, L. Poletto, A. Palacios, P. Decleva, J. B. Greenwood, F. Martín, and M. Nisoli, "Ultrafast charge dynamics in an amino acid induced by attosecond pulses," IEEE J. Sel. Top. Quantum. Electron., vol. 21, no. 5, pp. 1–12, 2015.

[109] D. J. Borton, L. M. Amundson, M. R. Hurt, A. Dow, J. T. Madden, G. J. Simpson, and H. I. Kenttämaa, "Development of a high-throughput laser-induced acoustic desorption probe and raster sampling for laser-induced acoustic desorption/atmospheric pressure chemical ionization," Anal. Chem., vol. 85, pp. 5720–5726, June 2013.

[110] P. A. Rigg, R. J. Scharff, and R. S. Hixson, "Sound speed measurements in tantalum using the front surface impact technique," J. Phys.: Conf. Ser., vol. 500, no. 3, p. 032018, 2014.

[111] A. Bondi, "Thermal properties of molecular crystals. I. Heat capacity and thermal expansion," J. Appl. Phys., vol. 37, pp. 4643–4647, Dec. 1966.

[112] N. R. Hutzler, H.-I. Lu, and J. M. Doyle, "The buffer gas beam: An intense, cold, and slow source for atoms and molecules," Chem. Rev., vol. 112, pp. 4803–4827, May 2012.

[113] Z. Huang, T. Ossenbrüggen, I. Rubinsky, M. Schust, D. A. Horke, and J. Küpper, "Development and characterization of a laser-induced acoustic desorption source," Anal. Chem., vol. 90, pp. 3920–3927, Feb. 2018.

[114] A. Dow, A. Wittrig, and H. Kenttämaa, "Laser-induced acoustic desorption (liad) mass spectrometry," Eur. J. Mass Spectrom., vol. 18, no. 2, pp. 77–92, 2012.

[115] R. C. Shea, C. J. Petzold, J.-a. Liu, and H. I. Kenttämaa, "Experimental investigations of the internal energy of molecules evaporated via laser-induced acoustic desorption into a fourier transform ion cyclotron resonance mass spectrometer," Anal. Chem., vol. 79, pp. 1825–1832, Mar. 2007.

[116] N. J. Demarais, Z. Yang, T. P. Snow, and V. M. Bierbaum, "Gas-phase reactions of polycyclic aromatic hydrocarbon cations and their nitrogen-containing analogs with h atoms," Astrophys. J., vol. 784, pp. 25–7, Feb. 2014.

[117] U. Sezer, L. Wörner, J. Horak, L. Felix, J. Tüxen, C. Götz, A. Vaziri, M. Mayor, and M. Arndt, "Laser-induced acoustic desorption of natural and functionalized biochromophores," Anal. Chem., vol. 87, pp. 5614–5619, June 2015.

[118] U. Sezer, P. Schmid, L. Felix, M. Mayor, and M. Arndt, "Stability of high-mass molecular libraries: the role of the oligoporphyrin core," J. Mass. Spectrom., vol. 50, pp. 235–239, Jan. 2015.

[119] A. Barty, J. Küpper, and H. N. Chapman, "Molecular imaging using x-ray free-electron lasers," Annu. Rev. Phys. Chem., vol. 64, pp. 415–435, Apr. 2013.

[120] X.-J. Wang and J.-Z. You, "Study on the molecular structure and thermal stability of purine nucleoside analogs," J. Anal. Appl. Pyrolysis, vol. 111, pp. 1–14, Jan. 2015.

[121] V. Y. Yablokov, I. L. Smel'tsova, I. A. Zelyaev, and S. V. Mitrofanova, "Studies of the rates of thermal decomposition of glycine, alanine, and serine," Russ. J. Gen. Chem., vol. 79, pp. 1704–1706, Sept. 2009.

[122] T. M. Jarrell, B. C. Owen, J. S. Riedeman, B. M. Prentice, C. J. Pulliam, J. Max, and H. I. Kenttämaa, "Laser-induced acoustic desorption/electron ionization of amino acids and small peptides," J. Am. Soc. Mass. Spectrom., vol. 28, no. 6, pp. 1091–1098, 2017.

[123] X. Ma, Y. Zhang, H.-R. Lei, and H. I. Kenttämaa, "Laser-induced acoustic desorption," MRS Bull, vol. 44, no. 5, pp. 372–381, 2019.

[124] W. S. M. Werner, K. Glantschnig, and C. Ambrosch-Draxl, "Optical constants and inelastic electron-scattering data for 17 elemental metals," J. Phys. Chem. Ref. Data, vol. 38, no. 4, pp. 1013–1092, 2009.

[125] A. W. Adamson, Physical chemistry of surfaces. John Wiley & Sons, 6 ed., 1997.

[126] M. Centurion, "Ultrafast imaging of isolated molecules with electron diffraction," J. Phys. B, vol. 49, no. 6, p. 062002, 2016.

[127] D. Ayuso, A. Palacios, P. Decleva, and F. Martin, "Ultrafast charge dynamics in glycine induced by attosecond pulses," Phys. Chem. Chem. Phys., vol. 19, p. 19767, 2017.

[128] D. Egorov, T. Lahaye, W. Schöllkopf, B. Friedrich, and J. Doyle, "Buffer-gas cooling of atomic and molecular beams," Phys. Rev. A, vol. 66, p. 043401, 2002.

[129] D. Egorov, T. Lahaye, W. Schollkopf, B. Friedrich, and J. M. Doyle, "Buffer-gas cooling of atomic and molecular beams," Phys. Rev. A, vol. 66, p. 043401, 2002.

[130] V. Singh, A. K. Samanta, N. Roth, D. Gusa, T. Ossenbrüggen, I. Rubinsky, D. A. Horke, and J. Küpper, "Optimized cell geometry for buffer-gas-cooled molecular-beam sources," Phys. Rev. A, vol. 97, p. 032704, Mar. 2018.

[131] J. Alfano, S. Martinez, and D. Levy, "Time-resolved spectroscopy of 3-amino-s-tetrazine and 3-amino-6-methyl-s-tetrazine in a supersonic jet," J. Chem. Phys., vol. 94, pp. 2475–2481, FEB 15 1991.

[132] M. R. Cameron and S. H. Kable, "A new design for a simple and effective pyrolysis nozzle in a supersonic free jet," Rev. Sci. Instrum., vol. 67, pp. 283–287, 1996.

[133] S. Deachapunya, P. J. Fagan, A. G. Major, E. Reiger, H. Ritsch, A. Stefanov, H. Ulbricht, and M. Arndt, "Slow beams of massive molecules," Eur. Phys. J. D, vol. 46, pp. 307–313, Feb. 2008.

[134] J. Stark and G. Wendt, "Beobachtungen über den effekt des elektrischen feldes auf spektrallinien. ii. längseffekt," Ann. Phys., vol. 348, no. 7, pp. 983–990, 1914.

[135] N. L. M. Müller, Electron diffraction and controlled molecules. Dissertation, Universität Hamburg, Hamburg, Germany, 2016.

[136] H. J. Loesch and A. Remscheid, "Brute force in molecular reaction dynamics: A novel technique for measuring steric effects," J. Chem. Phys., vol. 93, p. 4779, 1990.

[137] J. Bulthuis, J. Möller, and H. J. Loesch, "Brute force orientation of asymmetric top molecules," J. Phys. Chem. A, vol. 101, pp. 7684–7690, 1997.

[138] B. Friedrich and D. Herschbach, "Enhanced orientation of polar molecules by combined electrostatic and nonresonant induced dipole forces," J. Chem. Phys., vol. 111, p. 6157, Jan 1999.

[139] A. T. J. B. Eppink and D. H. Parker, "Velocity map imaging of ions and electrons using electrostatic lenses: Application in photoelectron and photofragment ion imaging of molecular oxygen," Rev. Sci. Instrum., vol. 68, no. 9, pp. 3477–3484, 1997.

[140] M. N. R. Ashfold, N. H. Nahler, A. J. Orr-Ewing, O. P. J. Vieuxmaire, R. L. Toomes, T. N. Kitsopoulos, I. A. Garcia, D. A. Chestakov, S.-M. Wu, and D. H. Parker, "Imaging the dynamics of gas phase reactions," Phys. Chem. Chem. Phys., vol. 8, no. 1, pp. 26–53, 2006.

[141] A. I. Chichinin, K. H. Gericke, S. Kauczok, and C. Maul, "Imaging chemical reactions — 3d velocity mapping," Int. Rev. Phys. Chem., vol. 28, no. 4, pp. 607–680, 2009.

[142] M. Stei, J. von Vangerow, R. Otto, A. H. Kelkar, E. Carrascosa, T. Best, and R. Wester, "High resolution spatial map imaging of a gaseous target," J. Chem. Phys., vol. 138, p. 214201, 2013.

[143] F. Calegari, A. Trabattoni, A. Palacios, D. Ayuso, M. C. Castrovilli, J. B. Greenwood, P. Decleva, F. Martín, and M. Nisoli, "Charge migration induced by attosecond pulses in bio-relevant molecules," Journal of Physics B: Atomic, Molecular and Optical Physics, vol. 49, no. 14, p. 142001, 2016.

[144] A. Zinovev, I. Veryovkin, and M. Pelli, "Molecular desorption by laser–driven acoustic waves: Analytical applications and physical mechanisms," in Acoustic Waves - From Microdevices to Helioseismology, InTech, Nov. 2011.

[145] T. Stolarski, Y. Nakasone, and S. Yoshimoto, Engineering Analysis with ANSYS Software. Elsevier, Jan. 2006.

[146] W. Frisch, "Characterizing laser induced desorption of large molecules," bachelor's thesis, Universität Hamburg, Hamburg, Germany, 2014.

[147] J. Lu, Z. Li, X. Jiang, and S. Rohani, "Solubility of l-phenylalanine in aqueous solutions," J. Chem. Eng. Jpn., vol. 43, no. 9, pp. 810–813, 2010.

A Appendix

A.1 Supplementary information chapter 2

Understanding the LIAD mechanism is crucial to make use of this vaporization method for preparing large thermally labile or non-volatile biomolecules into gas-phase. But the desorption mechanism remains unclear, because many different physical processes are involved. For example, how the laser interacts with metal foil and induces thermal and acoustic waves, how the thermal and acoustic waves propagate through the foil, and how the samples are desorbed. Lindner et al. [16] proposed that the desorption is caused by laser-induced acoustic wave. They observed that the delay between molecular ion desorption signals and desorption laser pulses is almost the same as the acoustic wave prorogation time. Zinovev et al. [35] proposed that the laser-induced thermal and acoustic stress causing the crack of crystals and then desorption. Campbell et al. proposed a blister model to explain their results [103, 104]. Different desorption mechanisms proposed by different groups are discussed below briefly.

A.1.1 Shake-off Model

Lindner et al. [16] and Golovlev et al. [18] proposed the acoustic shake off model to explain the desorption of molecules out of the substrate when laser shines the other side of the substrate. The evidence is that the delay between desorption laser pulse and molecules getting desorbed corresponds to the time for sound wave propagation through the substrate. If the acoustic shake-off dominants the desorption mechanism, velocity of desorbed molecules v should meet following equation:

$$v \geq \sqrt{2E_{ads}/m}, \tag{A.1}$$

where E_{ads} is the adsorption energy of molecules adsorbed on the substrate surface and m is its mass. The typical adsorption energies of the physically adsorbed molecules are

on the order of $\sim$ 0.5 eV [125], then we can calculate from Equation A.1 that minimal foil surface velocities needed are in the range of 700 m/s for the molecules with mass of 200 Da to be desorbed. These values are close to the speed of sound, for the solid, which was used as a proof of the validity of the LIAD model mentioned above. In fact, the velocities of acoustic waves propagating in solids are always much higher than the corresponding velocities of the mass motion [110].

In the shake-off mechanism, the desorption can only occur when the velocity of the moving foil surface is close to its maximum. This corresponds to the very first foil vibration, which lasts a fraction of a microsecond.

A.1.2 Thermal Model

Another desorption mechanism is thermal induced desorption. As in Calegari's experiments [30, 108], continuous wave (CW) laser with an unfocused spot size was utilized to shine the back of a 10 µm tantalum metal foil. The desorption can be caused by the thermal wave, which propagates through the foil and heats up the sample for their desorption. Compare to Zinovev's experiments [35], where pulsed focused UV laser beam was utilized, translational velocities of the desorbed molecules are independent of the laser intensities (thus, of the surface temperature). As a result, pure thermal model can not explain the experimental results acquired for short pulsed lasers.

A.1.3 Stress Model

Zinovev et al. proposed for their experiments with the following qualitative model [35,144]. The acoustic vibrations of the metal foil surface in combination with some rise in its temperature are the triggers for starting the desorption process. They proposed that isolated islands of analyte, formed on the metal surface after solution drying, are not in minimal energy states. It is usually the case that film growth on surfaces is accompanied with stress in the growing film. For LIAD phenomena, the important point is that each island can have some effective energy excess because of the stress. The acoustic and thermal waves can cause surface stress and, consequently, surface elastic deformation, which can initiate an island decomposition process. As a result of this effect, molecules can be desorbed from islands. The amount of energy stored in the residual stress depends on many unknown factors. But we need to note that the amount of energy transferred to the desorbed molecules during this process depends only on the specific characteristics of a given island, but does not depend on the total energy of the acoustic or thermal wave.

The mechanism is similar to the one proposed by Vertes for MALDI [57, 58], which is

based on a thermal stress generation in the layer of organic film deposited on solid substrate. Thermal stress energy due to foil heating by laser irradiation G may be expressed in the following equation:

$$G = \frac{E(1+v)^2}{2(1-v^2)} \times (\alpha_s - \alpha_f)^2 \Delta T^2 2\pi r_0 h_f \tag{A.2}$$

where E is the elasticity modulus, v is the Poisson ratio, α_s and α_f are the thermal expansion coefficients of the substrate and film correspondingly, $\triangle T$ is the temperature rise, and h_f and r_0 are the island thickness and radius. The average energy per analyte molecule g_a can be calculated using Equation A.2

$$g_a = \frac{E(1+v)^2}{2(1-v^2)\rho} \times \frac{(\alpha_s - \alpha_f)^2 \Delta T^2 M}{N_A} \tag{A.3}$$

Here M is the molar mass, ρ is the specific gravity, and N_A is the Avogadro number. It is interesting to note that g_a does not depend on the analyte island size but strongly depends on the thermal and mechanical parameters. The increasing of the desorption laser intensity causes a rise in $\triangle T$ and an increase in energy G, results in the formation of analyte cracks. This will increase the number of desorption sites and finally the total number of desorbed molecules. But because the formation of any individual cracks is defined only by the intermolecular bonding forces in the vicinity of the crack, the translational kinetic energy of desorbed molecules should remain independent of driving laser intensity.

A.1.4 Blister Model

Campbell et al. proposed a blister model to explain the desorption process [103, 104]. A very thin titanium film was deposited on a glass. And then a layer of nanoparticles was prepared on the titanium film. Then they shined a pulsed nanosecond laser through the glass on the titanium film to desorb nanoparticles into vacuum.

From the atomic force microscopy (AFM) images of titanium film after desorption of sample, they proposed that the titanium film created blister and desorbed nanoparticles into the vacuum. They named this technique as blister-based-laser-induced forward transfer [103, 104].

A.1.5 Repulsive Model

When the desorption laser intensity is high (>10^{10} W/cm^2), the emissions of charged particles (both positive and negative) have been observed due to the surface deformation [19]. Another possible mechanism for sample desorption for this case might be related to formation of nonequilibrium surface electron states due to migration and annihilation of solid dislocations. These electron states vary with the material, and range from formation of localized holes to generation of strong electric fields within the surface cracks for dielectrics. In any case, such states have an energy excess and could serve as an energy source for desorbing molecules [35]. This mechanism might play a major role at higher desorption laser intensities (>10^{10} W/cm^2), which may result from confinement conditions of laser plasma ignition.

A.1.6 Thermal Transient Simulation

Thermal transient simulation with Ansys [145] of the heat distribution in the tantalum foil after shining by laser pulses was presented in below. It helps us to understand the role of thermal process on the desorption mechanism as the thermal process can not be avoided no matter pulsed or continuous wave lasers are used. Table A.1 shows the simulation input parameters.

Table A.1: Input parameters for simulation.

Desorption laser and substrate parameter	**Value**
Wavelength	355 nm
Pulse duration (FWHM)	8 ns
Pulse energy	0.4 / 0.7 / 1 mJ
Spot size ($1/e^2$)	300 µm
Repetion rate	20 Hz
Tantalum reflectance	88%

The transient temperature distributions inside the foil with shining different laser pulse energy were obtained from the simulation. The results suggest that the surface temperature of the foil band increases nearly linearly with the intensity of desorption laser pulse. With a 0.4 mJ laser pulse no melting can be seen under the microscope, as well as a T_{max} of less than 1800 °C in the simulation indicates no melting ($T_{Ta,melting}$ = 3017 °C). For 0.7 mJ laser pulse the microscope image show no or only little melting of surface, whereas the simulation shows maximum temperatures of 3200 °C. The discrepancy can be explained by the fact that not all the power is absorbed only at the surface, but will

also penetrate into the material (volume effect). For the 1 mJ pulse melting was observed in the microscope images as well as in the simulation (up to 5400 °C).

A.2 Supplementary information chapter 3

A.2.1 Mass-to-charge ratio calibration

For our experiments, molecules are ionized between the TOF electrodes (repeller plate and extractor plate) with the presence of an electric field. The potential energy E_p of a particle of charge q in an electric field with the electric potential difference U is given by

$$E_p = qU \tag{A.4}$$

After the acceleration in the electric field, this potential energy is transferred to kinetic energy E_k of the particle of mass m in the flight tube.

$$E_p = E_k \tag{A.5}$$

$$qU = \frac{1}{2}mv^2 \tag{A.6}$$

With the known length d of the TOF one can express the mass to charge ratio by the flight time t of the ions:

$$\frac{m}{q} = 2U\left(\frac{t}{d}\right)^2 \tag{A.7}$$

When the mass to charge ratio $\frac{m_1}{q_1}$ of one peak in the TOF spectrum is known, we can convert the time-of-flight to mass to charge ratio. Since all ions were created in the same electric field, they all got the same potential U and traveled the same distance d:

$$\frac{m_1}{q_1} = 2U\left(\frac{t_1}{d}\right)^2 \tag{A.8}$$

Substitute Equation A.8 to Equation A.7:

$$\frac{m}{q} = \frac{m_1}{q_1}\left(\frac{t}{t_1}\right)^2 \tag{A.9}$$

As we can see from Equation A.9, the mass to charge ratio is proportional to the square of the time-of-flight. In the mass spectra measured in these experiments, the known peaks were either water ion at 18 u or the dominant ion mass, i.e. 74 u fragment

ion of phenylalanine, 135 u molecule ion of adenine and 30 u fragment ion of glycine. These peaks were primarily used for the mass calibration.

Usually there is a offset t_0 for the experimentally recored time-of-flight due to the delay between electronic trigger and photons arriving to the interaction point. Then Equation A.9 needs to consider the offset and will change to:

$$\frac{m}{q} = \frac{m_1}{q_1}\left(\frac{t - t_0}{t_1 - t_0}\right)^2 \tag{A.10}$$

For the offset t_0, either it can be experimentally determined with a photo diode for recording the delay between electronic trigger and photon arriving time to the interaction point or it can be derived if two peaks in the TOF spectrum are know. For the latter case, if the second peak at t_2 with $\frac{m_2}{q_2}$ is known, substitute $\frac{m_1}{q_1}$ at t_2 to Equation A.10:

$$\frac{m_2}{q_2} = \frac{m_1}{q_1}\left(\frac{t_2 - t_0}{t_1 - t_0}\right)^2 \tag{A.11}$$

As a result, t_0 can be derived from Equation A.11,

$$t_0 = \frac{t_1 - t_2\sqrt{\frac{\left(\frac{m_1}{q_1}\right)}{\left(\frac{m_2}{q_2}\right)}}}{1 - \sqrt{\frac{\left(\frac{m_1}{q_1}\right)}{\left(\frac{m_2}{q_2}\right)}}} \tag{A.12}$$

With the known t_0, experimentally measured time-of-flight can be converted to mass-to-charge ratio using Equation A.10 accurately.

A.2.2 Drop and Dry

For drop and dry method, Sample was first dissolved in a typical solvent, i.e. deionized water, methanol or ethanol for our case. Then the prepared solution was dropped onto the foil with a syringe. And then they were dried in atmosphere. The advantage of drop and dry method is easy to prepare a thin sample film, but the prepared film is not uniform due to the solution surface tension, which forms isolated spots on the foil. For the first version LIAD in our lab [146], the resulting solutions was dripped on the foil and evaporated, leaving behind sample on the foil. A foil holder was used as a barrier to confine the area on the foil, where solution gets deposited.

Figure A.1 shows optical microscope images of sample prepared by drop and dry

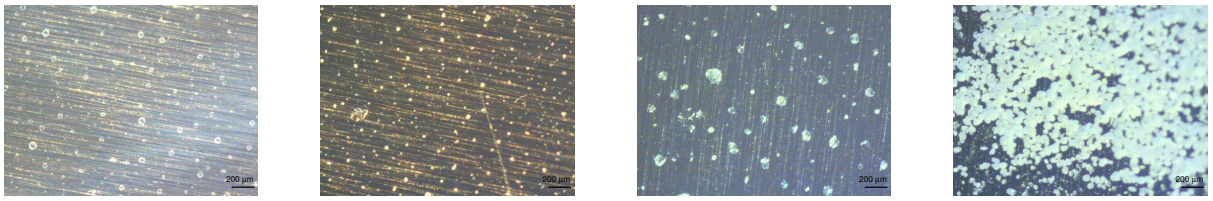

(a) 0.1 mmol/L (b) 1 mmol/L (c) 10 mmol/L (d) 100 mmol/L

Figure A.1: Microscope images of sample prepared by drop and dry method with different phenylalanine water solution concentration.

with different phenylalanine water solution concentration. The deposited phenylalanine solution formed small crystals on the foil after drying [28]. The quantity and size of these crystals are strongly defined by the molarity and amount of the solution deposited on the foil. It is clearly visible that the number of crystals on the foils rises with the molarity of the solution deposited on them.

A.2.3 Sample Drying with N_2

An advanced way of sample drying is with the help of a drying chamber. It was used by Borton et al. [109] and adapted in this work. The drying chamber improves the drying time by replacing the air atmosphere with a constant stream of nitrogen. The drying time can be reduced from over 20 min without, to approximately 6 min with drying chamber for 200 µL of solution.

A comparison of the results was shown in Figure A.2. It clearly demonstrates that the sample film is more uniform with N_2 drying. For the first version LIAD in our lab [146], we adapted this method for sample preparation. The reason why the sample dried with N_2 is thicker and more uniform than drying in air atmosphere is that the fast drying avoids the isolated spots due to the surface tension of solution. For drying in air atmosphere it takes more time and causes the solution flowing around and attaching on the barrier plate.

A.2.4 Brush Method

Similar as subsection A.2.2 sample was dissolved in solvent (i.e. deionized water, methanol, ethanol). Then the prepared solution was brushed and spread on the foil. The solvent was vaporized in the atmosphere and sample was deposited on the foil. It is very fast to prepare sample layers on a long foil band, i.e. our second LIAD version(see Figure 3.2 and Figure 3.3), but the layer is non-uniform after the solvent is vaporized due to the

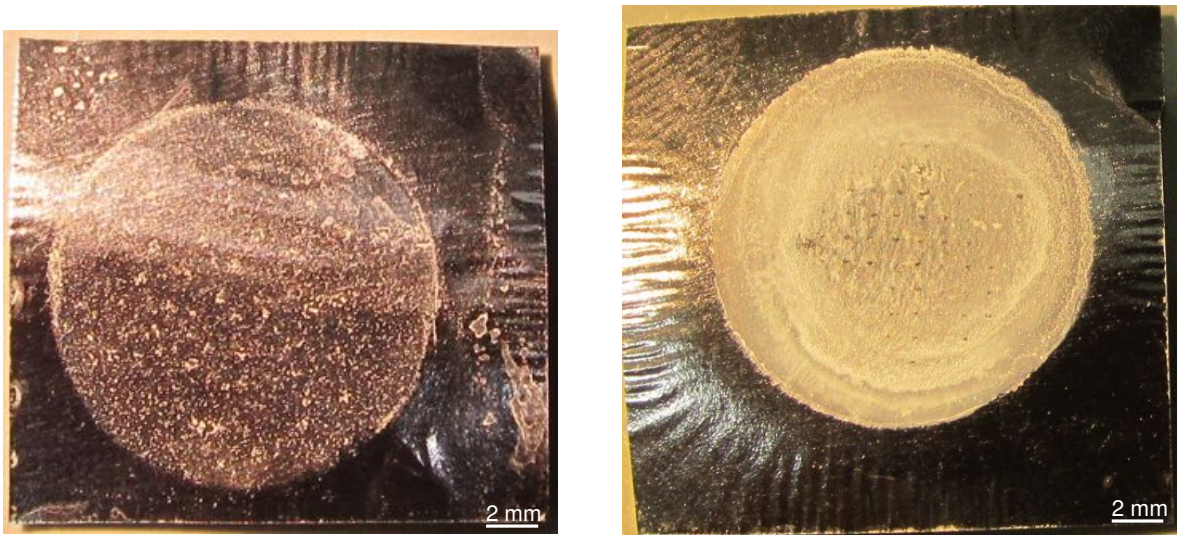

(a) Dried at air (b) Dried with N_2 stream

Figure A.2: Ta foils with 25 mM solution deposited on them. (a) dried at air (b) dried under a N_2 stream.

surface tension of the solution. As a result, isolated non-uniform sample spots are formed.

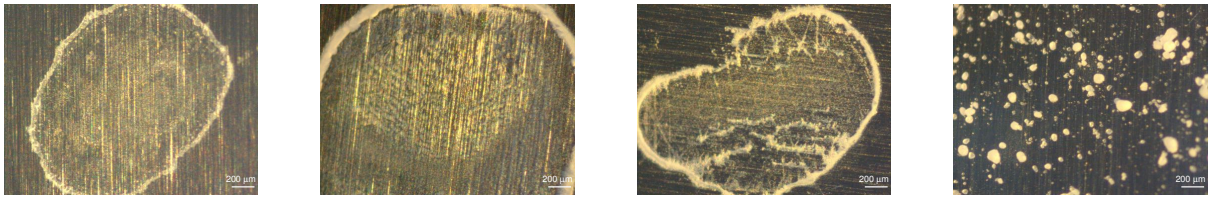

(a) 0.1 mmol/L (b) 1 mmol/L (c) 10 mmol/L (d) 100 mmol/L

Figure A.3: Microscope images of sample prepared by brush method with different phenylalanine water solution concentration.

Figure A.3 shows microscope images of sample prepared by brush method with different phenylalanine water solution concentration. Large isolated sample spots are spread on the foil. When the sample concentration goes higher, it tends to form small spots, which spread more uniformly. Even though the brush method can prepare a sample layer on the long foil band fast, the uniformity is not good.

A.2.5 Precipitation Method

Phenylalanine solubility in water solution decreases with temperature from 273.15 K to 343.15 K [147]. For precipitation method, the foil was immersed into the surface of

phenylalanine saturated aqueous solution, which was warmed up to increase the solubility and then cooled down to leave sample precipitate on the foil surface.

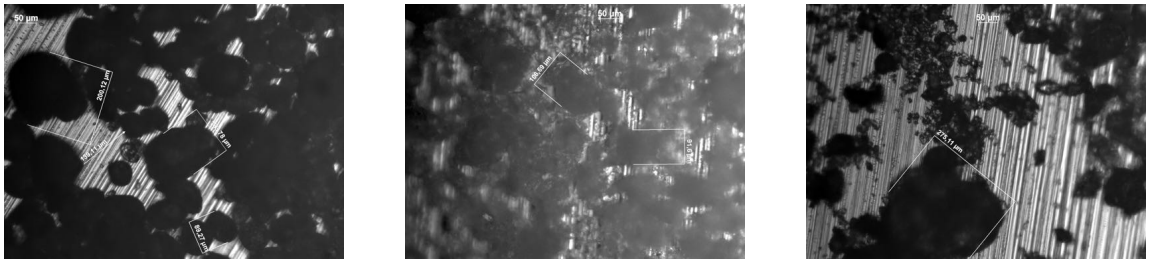

(a) 20 °C (b) 30 °C (c) 40 °C

Figure A.4: Microscope images of sample prepared by precipitation method with heating phenylalanine water solution concentration at different temperature.

Three pieces of foils with size around 2.5× 2.5 cm^2 were immersed into three 50 mL 0.1 mol/L phenylalanine water solution, which were heated to 20 °C, 30 °C and 40 °C respectively and cooled down quickly to 5 °C to let the phenylalanine precipitate on the foil. Figure A.4 shows microscope images of sample prepared by precipitation method for different phenylalanine aqueous solution temperature. It does not make much difference to heat the solution to different temperature. Crystals deposited on the foil are large comparing with other methods. As a result the spacing between these crystals are large and not uniform.

A.2.6 Slow-dragging Method

Similar as precipitation method, slow dragging method is that foil is immersed into the sample solution and then dragged out very slowly by a motor. The sample precipitates onto the surface of the foil due to vaporize of the solution.

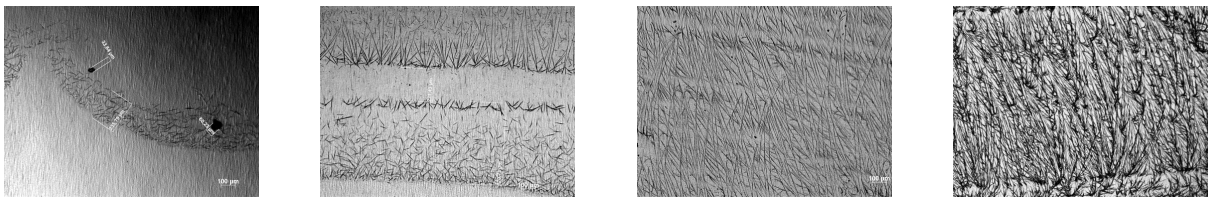

(a) 12.5 µm/s (b) 6.25 µm/s (c) 1.25 µm/s (d) 4.88 nm/s

Figure A.5: Microscope images of sample prepared by slow dragging method with different motor dragging speed.

Figure A.5 shows microscope images of sample prepared by slow dragging method with different moving speed. It clearly shows that the sample density on the foil band

increasing as slower the motor moving. This method is applicable to long foil bands and can prepare a very thin layer, but the layer is discontinuous and takes long time (4 h) to prepare a 1 m long foil band.

A.2.7 Rubbing Powder Method

For rubbing powder method, the sample powders were rubbed on the foil band directly using brush, glove, or ceramic stick. It has been adapted by Calegari et al. [30, 108]. It is a fast and easy method to prepare sample layer on a long foil band, but the prepared layer is not very uniform for our case and it is hard to control the sample layer thickness systematically.

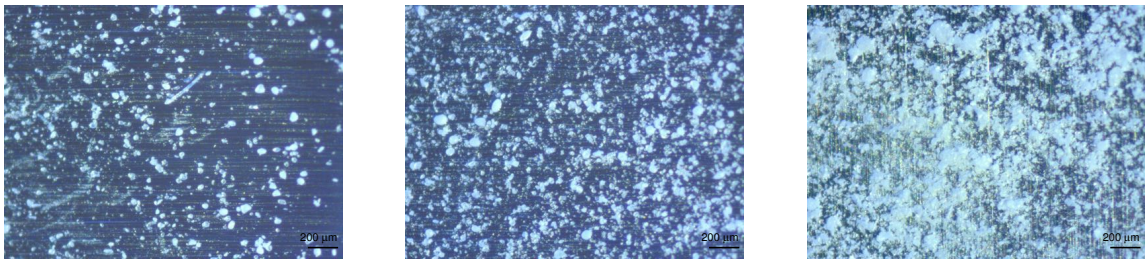

(a) Rubbing with brush (b) Rubbing with glove (c) Rubbing with stick

Figure A.6: Microscope images of sample prepared by rubbing raw sample powders with different tools on foil bands.

Figure A.6 shows microscope images of sample prepared by rubbing original raw sample powders bought directly from Sigma-Aldrich with different tools (i.e. brush, glove, stick) on foils. We can clearly see that sample crystals/powders spreads on the foil non-uniformly. There is no significant difference using different tools.

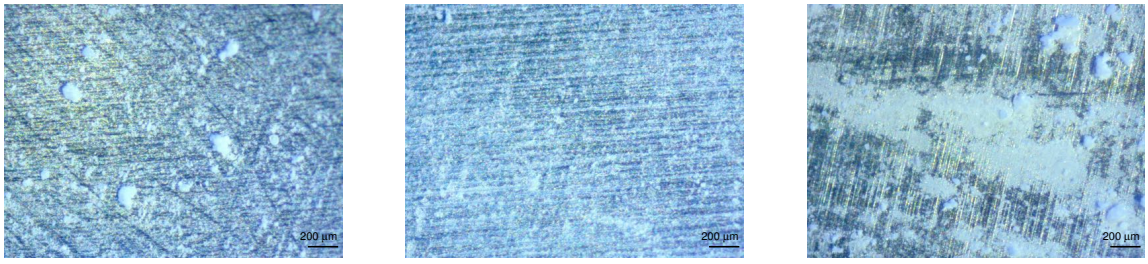

(a) Rubbing with brush (b) Rubbing with glove (c) Rubbing with stick

Figure A.7: Microscope images of sample prepared by rubbing grinded fine sample powders with different tools on foil bands.

Figure A.7 shows microscope images of sample prepared by rubbing fine powders

on foils with different tools. The fine powders are prepared by grinding the original raw powders using mortar and pestle. It clearly shows that the sample layers are more uniform comparing to rub the original powders. The sample layer prepared using gloves distributes more uniform than other tools. But it is difficult to control the sample layer thickness systematically.

A.3 Supplementary information chapter 4

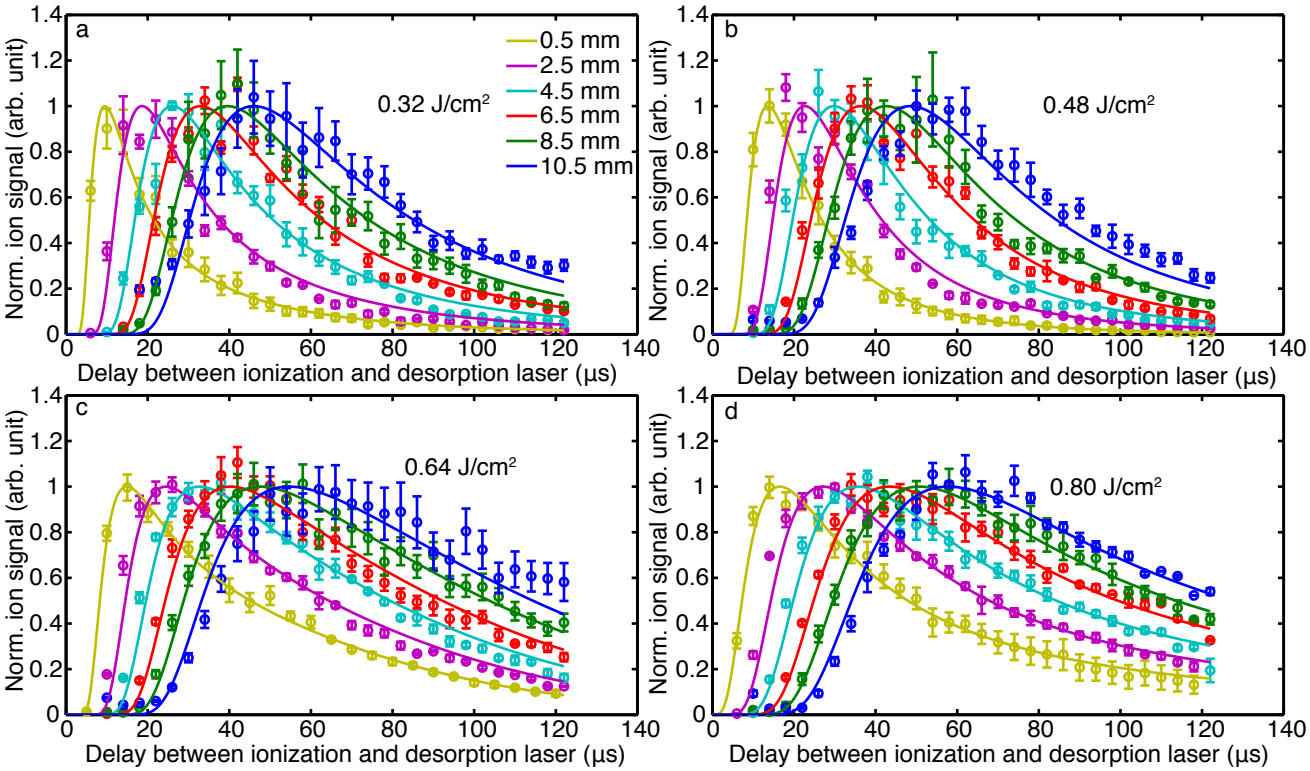

Figure A.8: Normalized temporal profiles of intact phenylalanine parent-ion signals following desorption with a) 0.32 J/cm^2, b) 0.48 J/cm^2, c) 0.64 J/cm^2, and d) 0.80 J/cm^2, recorded for different distances from the foil band. Solid lines correspond to a fit with a Maxwell-Boltzmann distribution convoluted with the desorption time distribution; see main text for details.

A.4 Supplementary information chapter 5

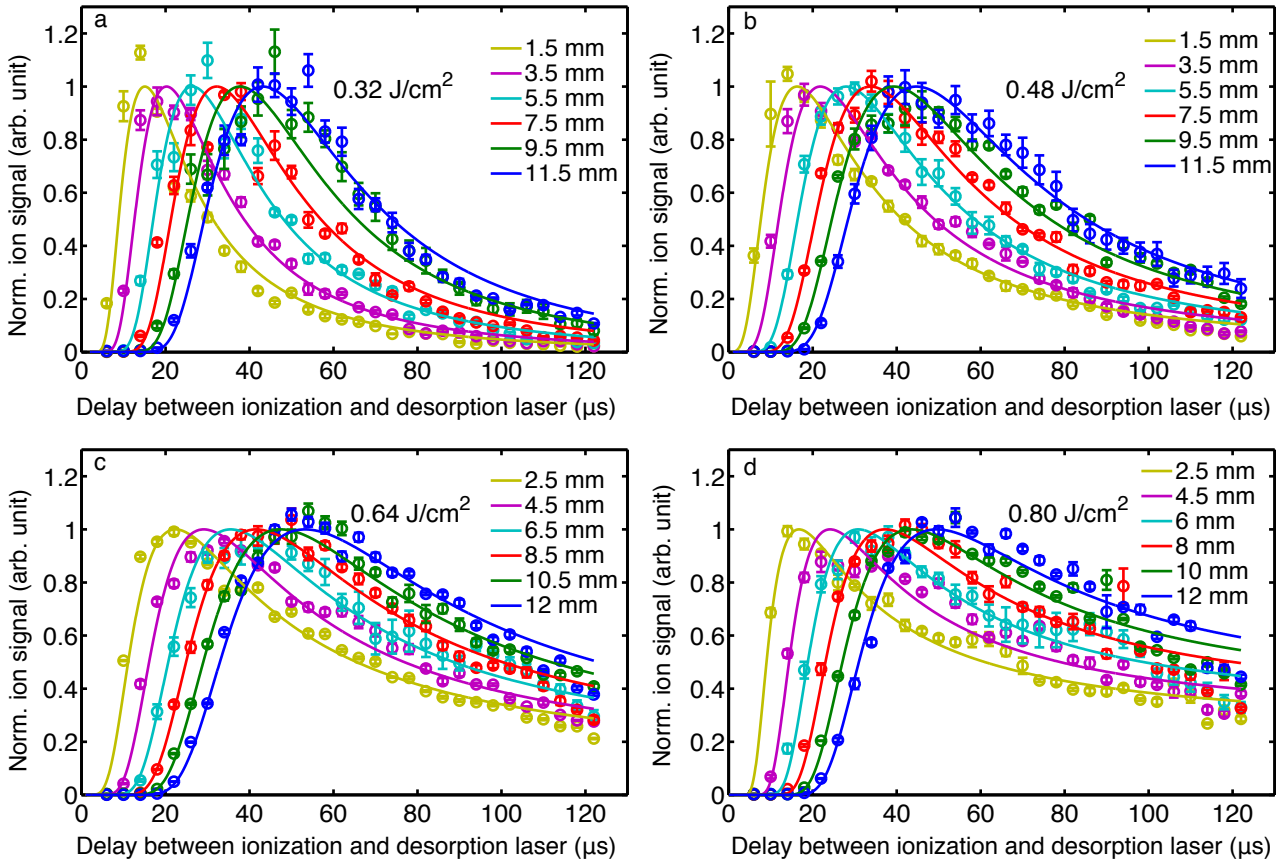

Figure A.9: Normalized temporal profiles of adenine intact parent-ion signals following desorption with a) 0.32 J/cm^2, b) 0.48 J/cm^2, c) 0.64 J/cm^2, and d) 0.80 J/cm^2, recorded for different distances from the foil band. Solid lines correspond to a fit with a Maxwell-Boltzmann distribution convoluted with the desorption time distribution; see main text for details.

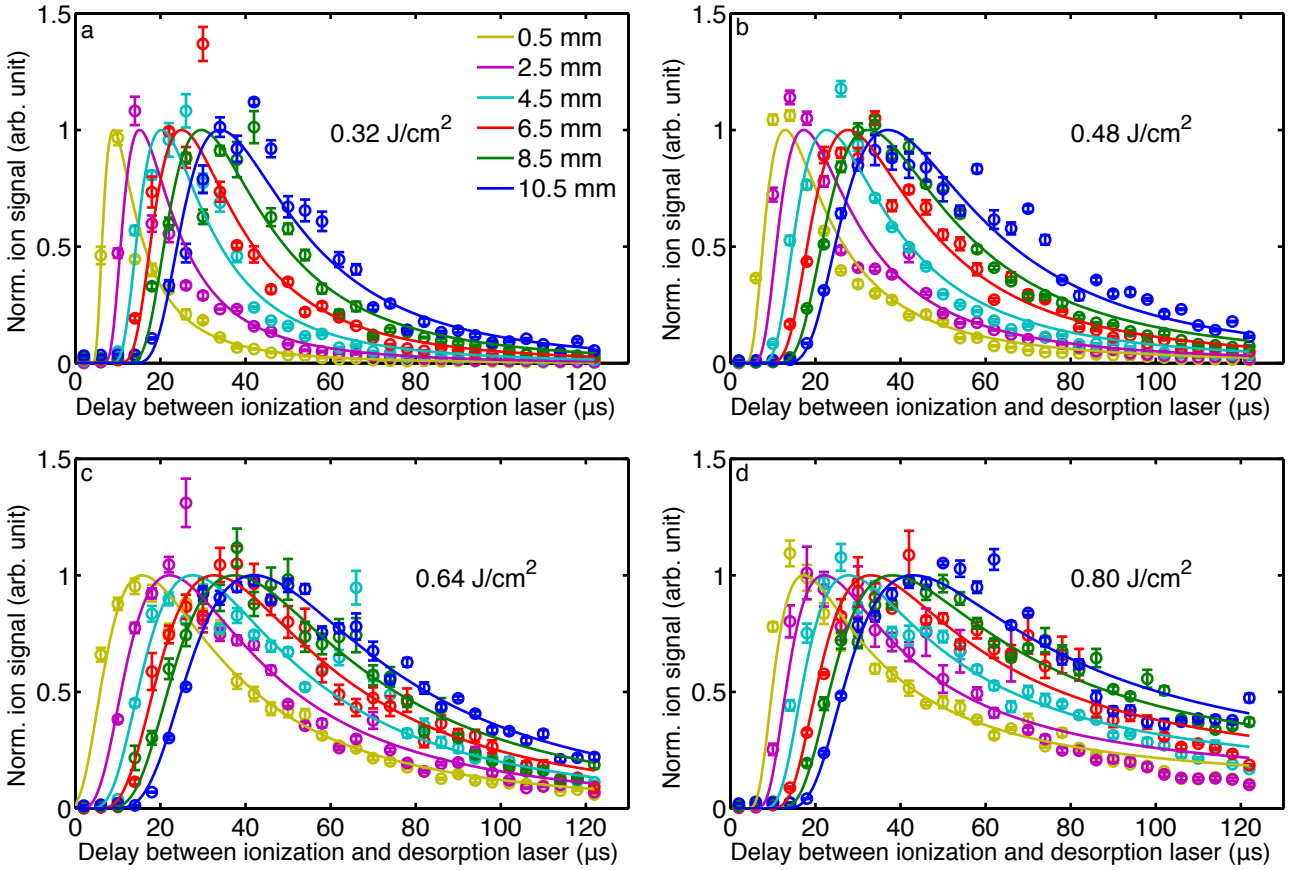

Figure A.10: Normalized temporal profiles of glycine intact parent-ion signals following desorption with a) 0.32 J/cm^2, b) 0.48 J/cm^2, c) 0.64 J/cm^2, and d) 0.80 J/cm^2, recorded for different distances from the foil band. Solid lines correspond to a fit with a Maxwell-Boltzmann distribution convoluted with the desorption time distribution; see main text for details.

Acknowledgements

I would like to take this opportunity to thank all of the people who helped me finish this thesis.

First of all I would like to thank my supervisors Prof. Dr. Jochen Küpper, Prof. Dr. Henry Chapman and Dr. Daniel A. Horke for giving me this great subject for my PhD thesis and supervise me. Thank you for the opportunity to be a part of your group.

Secondly I would like to acknowledge the financial support from the Joachim Herz Foundation and PIER Helmholtz Graduate School. I would especially thank Dr. Eva Ackermann from JHZ for organizing nice get-together events yearly and Mirko and Stefanie from PIER for organizing the soft skill courses and workshops.

Thirdly I would thank all of the CMI members for the nice discussions and beer time. Especially I would like to thank Dr. Daniel A. Horke for the patient supervising and COMOTION members for working together. And I would like to point out that this thesis has been supported by the European Research Council under the European Union's Seventh Framework Programme (FP7/2007-2013) through the Consolidator Grant COMOTION (ERC-614507-Küpper).

Finally and most importantly I want to thank my wife Mrs. Mingmei Sun for her support and meticulous care during my PhD. And the birth of our lovely daughter Jenny encouraged me a lot. Thanks for the happiness she brings to me and our family.

List of Publications

1. *Laser-induced acoustic desorption of thermally stable and unstable biomolecules*
   Z. Huang, D. Horke, and J. Küpper
   under review, 2019, arXiv:1811.05925 [physics].

2. *Development and characterization of a laser-induced acoustic desorption source*
   Z. Huang, T. Ossenbrüggen, I. Rubinsky, M. Schust, D. Horke, and J. Küpper
   Analytical Chemistry **90(6)**, 3920-3927(2018).

3. *Voltage dependent quantum efficiency measurement in property study of thin film solar cells*
   Z. Huang, S. Zhao, L. Sun, P. Sun, C. Zhang, Y. Wu, H. Cao, Z. Hu, S. Wang, P. Yang, and J. Chu
   Journal of Infrared and Millimeter Waves **33(4)**, 395-399 (2014).

4. *A 5.5% efficient co-electrodeposited ZnO/CdS/Cu_2ZnSnS_4/Mo thin film solar cell*
   J. Ge, J. Jiang, P. Yang, C. Peng, **Z. Huang**, S. Zuo, L. Yang, and J. Chu
   Solar Energy Materials and Solar Cells **125**, 20-26 (2014).

5. *Influence of Co doping on structural, optical and magnetic properties of $BiFeO_3$ films deposited on quartz substrates*
   L. Peng, H. Deng, J. Tian, Q. Ren, C. Peng, **Z. Huang**, P. Yang, and J. Chu
   Applied Surface Science **268**, 146-150 (2013).

6. *Numerical analysis of the non-ideal current-voltage characteristics of solar cells*
   S. Zhao, **Z. Huang**, L. Sun, P. Sun, C. Zhang, Y. Wu, H. Cao, Z. Huang, S. Wang, and J. Chu
   Journal of Infrared and Millimeter Waves **32(5)**, 389-393 (2013).

7. *A detailed study of the effect of Schottky barrier on the dark current density-voltage characteristics of CdS/CdTe solar cells*
   S. Zhao, **Z. Huang**, L. Sun, P. Sun, C. Zhang, Y. Wu, H. Cao, G. Hu, S. Wang,

and J. Chu
Acta Physica Sinica **62(16)**, 168801 (2013).

8. *Analysis of electrical property parameters of CdS/CdTe solar cells fabricated by close space-sublimation*
S. Zhao, **Z. Huang**, L. Sun, P. Sun, C. Zhang, Y. Wu, H. Cao, G. Hu, S. Wang, and J. Chu
Acta Physica Sinica **62(18)**, 188801 (2013).